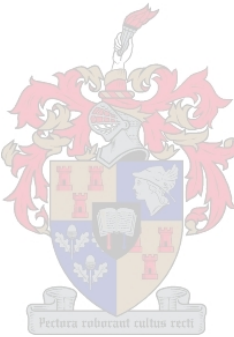


# Heavy-quark production via leptonic decays at forward rapidity in pp collisions with ALICE at the LHC

by

Christine Marie Monteverdi



*Thesis presented in partial fulfilment of the requirements for  
the degree of Master of Science (Physics) in the Faculty of  
Science at Stellenbosch University*

Supervisor: Prof Z. Buthelezi & Dr. S. V. Förtzsch  
Co-supervisor: Prof P. Papka

March 2020

The financial assistance of the National Research Foundation (NRF) towards this research is hereby acknowledged. Opinions expressed and conclusions arrived at, are those of the author and are not necessarily to be attributed to the NRF.

# Declaration

By submitting this thesis electronically, I declare that the entirety of the work contained therein is my own, original work, that I am the sole author thereof (save to the extent explicitly otherwise stated), that reproduction and publication thereof by Stellenbosch University will not infringe any third party rights and that I have not previously in its entirety or in part submitted it for obtaining any qualification.

Date: ..... 2020/03/03

Copyright © 2020 Stellenbosch University  
All rights reserved.

# Abstract

## Heavy-quark production via leptonic decays at forward rapidity in pp collisions with ALICE at the LHC

C. Monteverdi

*Department of Physics,  
University of Stellenbosch,  
Private Bag X1, Matieland 7602, South Africa.*

Thesis: MSc (Physics)

March 2020

The measurements for the study of heavy-quark production in proton-proton (pp) collisions with ALICE at Large Hadron Collider (LHC) energies are described. Heavy-quarks (charm and beauty) are produced at an early stage of the collision via hard parton scatterings. In ALICE, heavy-quarks are measured in the central barrel ( $|\eta| < 0.9$ ) via the hadronic and electronic decay channels and at forward rapidity ( $-4 < \eta < -2.5$ ) via the single muon decay channel. These measurements provide a testing ground for quantum chromodynamics (QCD) theoretical models and also serve as a baseline for heavy-ion collisions. This study focuses on the measurement of heavy-quark production via the inclusive single muon decay channel at forward rapidity in the ALICE Muon Spectrometer. In this region, one is able to exploit the single high and low transverse momentum ( $p_T$ ) triggers to measure the inclusive single muon  $p_T$  and pseudorapidity ( $\eta$ ) differential cross sections. These single muon differential cross sections are presented and compared to model calculations, by means of the Fixed Order plus Next-to-Leading Logarithms (FONLL).

# Uittreksel

## Heavy-quark production via leptonic decays at forward rapidity in pp collisions with ALICE at the LHC

(“Heavy-quark production via leptonic decays at forward rapidity in pp collisions with ALICE at the LHC”)

C. Monteverdi

*Departement Fisika,  
Universiteit van Stellenbosch,  
Privaatsak X1, Matieland 7602, Suid Afrika.*

Tesis: MS (Fisika)

Maart 2020

The measurements for the study of heavy-quark production in proton-proton (pp) collisions with ALICE at Large Hadron Collider (LHC) energies are described. Heavy-quarks (charm and beauty) are produced at an early stage of the collision via hard parton scatterings. In ALICE, heavy-quarks are measured in the central barrel ( $|\eta| < 0.9$ ) via the hadronic and electronic decay channels and at forward rapidity ( $-4 < \eta < -2.5$ ) via the single muon decay channel. These measurements provide a testing ground for quantum chromodynamics (QCD) theoretical models and also serve as a baseline for heavy-ion collisions. This study focuses on the measurement of heavy-quark production via the inclusive single muon decay channel at forward rapidity in the ALICE Muon Spectrometer. In this region, one is able to exploit the single high and low transverse momentum ( $p_T$ ) triggers to measure the inclusive single muon  $p_T$  and pseudorapidity ( $\eta$ ) differential cross sections. These single muon differential cross sections are presented and compared to model calculations, by means of the Fixed Order plus Next-to-Leading Logarithms (FONLL).

# Acknowledgements

- Prof Zinhle Buthelezi for supporting me, encouraging me and most of all motivating me throughout my masters, both academically and personally. I am eternally grateful for all the wisdom she bestowed on me. I am thankful for all the opportunities to visit CERN to collaborate, as well as Hamburg to attend the physics summer school. I appreciate the pushes to present posters and give presentations, all in preparation for the final presentation of this thesis.
- Sibaliso Mhlanga for helping me understand concepts and taking me through the example codes provided by the ALICE environment. Sibaliso's help was critical in the completion of this thesis.
- Amal Sarkar for providing me with additional macros to compare to when I encountered errors at the beginning of the analysis.
- Dr. Siegfried Förtsch for asking the less obvious questions and making me aware of the gaps in my understanding.
- Prof Paul Papka for supervising me and encouraging me to get to where I am. I am thankful for the support and understanding he provided.
- Dr. Claire Leatham for the weekly check-ins and confidence boost. Her faith in me and prayers kept my head up when things got tough.
- Madison Tonkin, Adrienne Marais and Keziah Mayer for their friendship and positive influence on my day to day life.
- Courtney Morris for being the voice of reason, for justifying my frustrations and for believing in me.

# Dedications

*This thesis is dedicated to my parents, Bernard and Gillian, and my brothers René and Simon.*

# Contents

<b>Declaration</b>	i
<b>Abstract</b>	ii
<b>Uittreksel</b>	iii
<b>Acknowledgements</b>	iv
<b>Dedications</b>	v
<b>Contents</b>	vi
<b>List of Figures</b>	viii
<b>List of Tables</b>	xi
<b>Nomenclature</b>	xii
<b>1 Introduction and Theoretical Background</b>	1
1.1 Introduction . . . . .	1
1.2 Theoretical basis . . . . .	4
1.3 Literature Review . . . . .	10
1.4 Motivation and Aims of the Study . . . . .	13
1.5 Layout . . . . .	13
<b>2 The ALICE experiment</b>	15
2.1 ALICE at the LHC . . . . .	15
2.2 The ALICE Muon Spectrometer . . . . .	18
2.3 Alignment of the tracking chambers . . . . .	21
2.4 Trigger detectors . . . . .	22
2.5 LHC Beam Conditions . . . . .	23
2.6 Data Taking Conditions . . . . .	26
<b>3 Data Analysis</b>	29
3.1 Data sample . . . . .	29
3.2 The Analysis Strategy . . . . .	30

3.3 ALICE offline framework . . . . .	38
3.4 FONLL model calculations . . . . .	38
3.5 Acceptance and efficiency correction . . . . .	47
<b>4 Results and Discussion</b>	<b>52</b>
4.1 Differential production cross section measurements . . . . .	52
4.2 Discussion of results . . . . .	56
<b>5 Summary and Conclusion</b>	<b>64</b>
5.1 Summary . . . . .	64
5.2 Conclusion . . . . .	65
5.3 Outlook . . . . .	65
<b>List of References</b>	<b>67</b>
<b>Appendices</b>	<b>73</b>
<b>Run list</b>	<b>74</b>
<b>runGrid.C</b>	<b>75</b>
<b>AliAnalysisExamplePt.cxx</b>	<b>77</b>
<b>sim.C</b>	<b>82</b>
<b>rec.C</b>	<b>84</b>
<b>trigger.C</b>	<b>85</b>
<b>ReadPurity.C</b>	<b>88</b>
<b>muCalc.C</b>	<b>89</b>
<b>NormFinal.C</b>	<b>91</b>

# List of Figures

1.1	The range of Bjorken- $x$ values accessible in heavy-ion collisions at the top energies reached by the SPS, RHIC and the LHC [Col04]. . . . .	2
1.2	"The Standard Model of Elementary Particles"[fPPPI] . . . . .	5
1.3	The QCD coupling constant $\alpha_{QCD}$ as a function of $Q$ , the scale of the interaction [Bet07]. . . . .	8
1.4	Feynman diagrams depicting the LO processes, from left to right, quark-antiquark annihilation, gluon-gluon fusion, flavour excitation and gluon splitting. . . . .	9
1.5	QCD meson and Feynman diagram of heavy flavour decay via a semi-leptonic decay channel [Shi08]. . . . .	9
1.6	Energy dependence of the total nucleon-nucleon charm ( $c\bar{c}$ ) and beauty ( $b\bar{b}$ ) production cross sections [Col14a] [Col12a]. . . . .	11
1.7	Ratio of the $p_T$ -differential production cross sections of muons from heavy-flavour hadron decays at forward rapidity in pp collisions at $\sqrt{s} = 7$ TeV to those at $\sqrt{s} = 5.02$ TeV [Col17b]. . . . .	12
2.1	CERN accelerator complex [BW17], showing a schematic view of the LHC and its injection scheme as well as other ongoing CERN experiments. . . . .	16
2.2	The ALICE Detector [Pal17]. . . . .	16
2.3	Pseudorapidity and $\theta$ angle relation in the yz-plane. . . . .	17
2.4	The Front Absorber [Col00], where the units used are in cm. . . . .	18
2.5	Schematic representation of the ALICE Muon Spectrometer, with a single muon traversing the Muon Spectrometer, illustrated by the red line. . . . .	19
2.6	General view of the GMS setup used to measure relative displacements between the chambers [KT05]. . . . .	22
2.7	A typical sequence of LHC Beam Modes within a fill. . . . .	25
2.8	Integrated luminosity delivered to ALICE in 2017 for pp collisions at 13 TeV [Colb]. . . . .	28
3.1	Analysis strategy followed. . . . .	31
3.2	runGrid.C, showing the implementation of event selection cuts. . .	31

3.3	Schematic representation of V0 detectors' position and timing [Kry14] for the event selection . . . . .	32
3.4	Vertex distributions depicting the distribution of events as a function of the vertex position for trigger CMSH and data taking period LHC17k after applying the various event cuts. . . . .	33
3.5	$p_{\text{DCA}}$ as a function of $p_T$ , illustrating the effect of the $p_{\text{DCA}}$ track cut on LHC17k data with the CMSH trigger. See text for details. . . . .	34
3.6	Extracted $p_T$ - and $\eta$ - distributions obtained from merged data samples collected during periods LHC17h and k using the CMSH trigger class. These distributions are extracted after implementing event and track cuts. . . . .	36
3.7	Extracted $p_T$ - and $\eta$ - distributions obtained from merged data samples collected during periods LHC17h and k using the CMSL trigger class. These distributions are extracted after implementing event and track cuts. . . . .	37
3.8	The ALICE Offline Framework for Raw Data [Col19a]. . . . .	39
3.9	Differential production cross sections of heavy-flavour decay muons as a function of $p_T$ for pp collisions at 13 TeV obtained from calculations by means of FONLL event generator [Nas98]. . . . .	41
3.10	(Top) Differential production cross section of heavy-flavour decay muons as a function of $p_T$ in pp collisions at 13 TeV obtained from calculations using the FONLL event generator [Nas98] compared to the fit function given in Equation 3.7, including statistical errors as horizontal bars. (Bottom) The ratio of the FONLL results to the fit function. . . . .	42
3.11	Differential production cross sections from heavy-flavour production as a function of $\eta$ for pp collisions at 13 TeV obtained from FONLL event generator calculations [Nas98]. . . . .	43
3.12	(Top) Differential production cross section of heavy-flavour muons as a function of $\eta$ for pp collisions at 13 TeV obtained from calculations using the FONLL event generator [Nas98] and fitted with the function described in Equation 3.8. (Bottom) The ratio of the FONLL results to the fit function. . . . .	44
3.13	Reconstructed and generated $\eta$ - and $p_T$ -distributions for the geometrical acceptance of the Muon Spectrometer, $-4 < \eta < -2.5$ , with the high- $p_T$ muon trigger, CMSH. . . . .	45
3.14	Reconstructed and generated $\eta$ - and $p_T$ -distributions for the geometrical acceptance of the Muon Spectrometer, $-4 < \eta < -2.5$ , with the low- $p_T$ muon trigger, CMSL. . . . .	46
3.15	$A \times \epsilon$ as a function of $p_T$ for the high- and low- $p_T$ muon triggers, CMSH(L), in the range $2 < p_T < 20 \text{ GeV}/c$ . . . . .	48
3.16	$A \times \epsilon$ as a function of $\eta$ for the high- and low- $p_T$ muon triggers, CMSH(L)7-B-NOPF-MUFAST, in the range $-4 < \eta < -2.5$ . . . . .	49

3.17	Total extracted yield of all single muons (blue) and corrected bin by bin for $A \times \epsilon$ (red) as a function of $p_T$ and $\eta$ in the range $2 < p_T < 20$ GeV/ $c$ and $-4 < \eta < -2.5$ , respectively, for the muon trigger CMSH.	50
3.18	Total extracted yield of all single muons (blue) and corrected bin by bin for $A \times \epsilon$ (red) as a function of $p_T$ and $\eta$ in the ranges $2 < p_T < 20$ GeV/ $c$ and $-4 < \eta < -2.5$ for the low muon trigger CMSL. . . . .	51
4.1	Typical single muon background contribution in the $p_T$ distributions in the Muon Spectrometer studied in [Col14b]. . . . .	55
4.2	(Top) Inclusive differential production cross sections of single muons from heavy-flavour decays as a function of $p_T$ comparing the low- and high- $p_T$ triggers, CMSL and CMSH, with statical errors in the horizontal direction. (Bottom) The ratio of CMSH to CMSL. . . . .	57
4.3	(Top) Inclusive differential production cross sections of single muons from heavy-flavour decays as a function of $\eta$ comparing the low- and high- $p_T$ triggers, CMSL and CMSH, with statical errors as horizontal bars. (Bottom) The ratio of CMSH to CMSL. . . . .	58
4.4	Inclusive differential production cross sections of single muons from heavy-flavour decays as a function of $p_T$ for the high- $p_T$ trigger, compared with FONLL results, all with statistical uncertainties in the horizontal direction. . . . .	59
4.5	(Top) Inclusive differential production cross sections of single muons from heavy-flavour decays as a function of $p_T$ for the high- $p_T$ trigger, compared with the sum of the FONLL decay channels, all with statistical uncertainties as horizontal bars. (Bottom) The ratio of results obtained to the sum of the FONLL decay channels. . . . .	60
4.6	Inclusive differential production cross sections of single muons from heavy-flavour decays as a function of $\eta$ for the high- $p_T$ trigger, compared with FONLL results, all shown with statistical uncertainties as horizontal bars. . . . .	62
4.7	(Top) Inclusive differential production cross sections of single muons from heavy-flavour decays as a function of $\eta$ for the high- $p_T$ trigger, compared with the sum of the FONLL decay channels, all with statistical uncertainties as horizontal bars. (Bottom) The ratio of results obtained to the sum of the FONLL decay channels. . . . .	63

# List of Tables

1.1	The heavy-flavour production processes considered in this study. . . . .	13
2.1	LHC Beam Modes and corresponding ALICE operations [Cola] . . . . .	27
2.2	Data taking conditions . . . . .	28
3.1	The Quality Assurance (QA) criteria used to define the quality of the data in this analysis [Col17a]. . . . .	29
3.2	Total number of analysed runs that passed the QA per data taking period. . . . .	30
3.3	Summary of the trigger-selected statistics after applying various event cuts: physics selection and good vertex. . . . .	32
3.4	The number of events recorded per track cut according to the triggers selected for each data taking period used in this analysis. . . . .	35
4.1	Normalisation factors obtained for each data taking period, per muon trigger in this study. . . . .	54

# Nomenclature

## Variables

$x = \frac{Me^{\pm y}}{\sqrt{s}}$	Bjorken-x	[ ]
$p_T = \sqrt{p_x^2 + p_y^2}$	Transverse momentum	[GeV/c]
$y = \frac{1}{2} \ln \frac{E+p_z c}{E-p_z c}$	Rapidity	[ ]
$\eta = -\ln(\tan \frac{\theta}{2})$	Pseudorapidity	[ ]
$L = \frac{1}{\sigma} \frac{dN}{dt}$	Luminosity	[s <sup>-1</sup> b <sup>-1</sup> ]
$L_{int} = \int L dt$	Integrated luminosity	[b <sup>-1</sup> ]
$\sqrt{s}$	Centre-of-mass energy	[TeV]
$\theta$	Rotation angle	[deg]
$p$	Momentum	[GeV/c]
$dN/dp_T$	$p_T$ -yield	[counts/GeV/c]
$dN/d\eta$	$\eta$ -yield	[counts]
$\gamma$	Lorentz factor	[ ]
( [ ] indicates a dimensionless quantity.)		

# Chapter 1

## Introduction and Theoretical Background

### 1.1 Introduction

At the Large Hadron Collider (LHC) 600 million collisions occur between protons every second [CERa]. On average, the LHC collides protons with protons for 7 months of the year and heavy ions for 1 month. At the LHC an unprecedented energy regime is reached enabling scientists to discover new physics. These proton-proton (pp) collisions are used as a baseline for corresponding heavy-ion collisions, such as lead-lead (Pb-Pb) and proton-lead (p-Pb). They are also used to test Quantum Chromodynamic (QCD) calculations. The maximum centre-of-mass energy ( $\sqrt{s}$ ) achieved in pp, p-Pb and Pb-Pb collisions at the LHC are 13 TeV, 8.16 TeV and 5.02 TeV, respectively. Compared to lower energy facilities, e.g. CERN Super Proton Synchrotron (SPS) [DF08] and the Relativistic Heavy Ion Collider (RHIC) [Kea17], the LHC is able to probe the small Bjorken- $x$  regime, as illustrated in Figure 1.1, where the Bjorken- $x$  is defined as the momentum fraction of the proton carried by its parton that participate in the parton-parton scatterings. A parton (a quark or gluon) is a constituent of a nucleon (e.g. a proton). Bjorken- $x$  can be calculated according to Equation 1.1,

$$x = \frac{Me^{\pm y}}{\sqrt{s}}, \quad (1.1)$$

where  $M$  denotes the mass of the particle,  $s$  the centre-of-mass energy and  $y$  the rapidity, defined as

$$y = \frac{1}{2} \ln \frac{E + p_z c}{E - p_z c}, \quad (1.2)$$

where  $E$  is the energy of a particle at rest,  $p_z$  is the z component of the momentum of a particle, where the z-axis is the beam axis, and  $c$  is the speed of light.

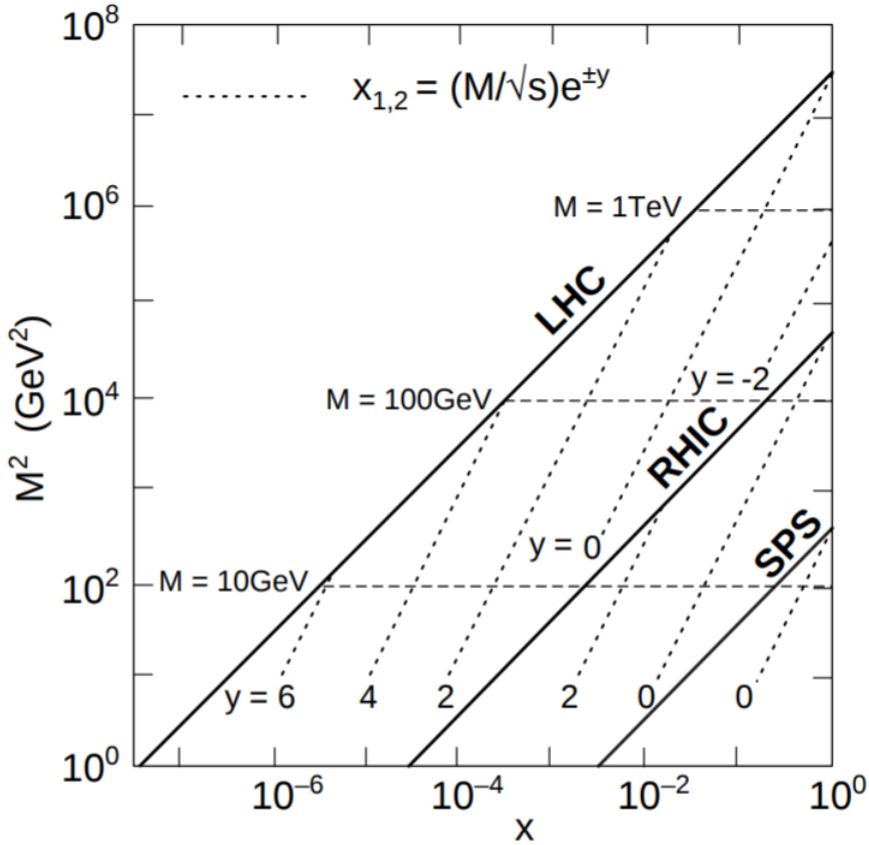


**Figure 1.1:** The range of Bjorken- $x$  values accessible in heavy-ion collisions at the top energies reached by the SPS, RHIC and the LHC [Col04].

In terms of heavy-ion collisions (HIC), theoretical calculations predict that a deconfined state of matter, referred to as the Quark-Gluon Plasma (QGP), can be formed with an increase in energy, large baryon densities ( $\simeq 0.5 - 2$  baryons/fm $^3$ ) and extreme temperatures ( $\simeq 2 \times 10^{12}$  K) [Mhl15]. This phase of deconfined quarks and gluons exists for a short time, 5-10 fm/c before hadronisation occurs, a phase in which quarks and gluons form hadrons such as mesons and baryons, consisting of two and three quarks, respectively.

At the LHC, ALICE (A Large Ion Collider Experiment) [Col08] is one of the 4 major experiments. It is optimized to study the physics of strongly interacting matter by examining nucleus-nucleus (Pb-Pb) collisions [Sch12]. The primary focus is track reconstruction of short-lived particles such as heavy-flavours and particle identification over a wide momentum range (0.1 - 100 GeV/itc). These heavy-ion collisions (HIC) provide the highest energy densities reached thus far in the laboratory. As a result one can reach the strongly interacting primordial phase of matter (QGP). For this reason, ALICE carries out a comprehensive study of the final state particles, namely hadrons, elec-

trons, muons and photons, produced in Pb-Pb collisions. Furthermore, ALICE studies pp and p-Pb collisions both as a comparison with nucleus-nucleus collisions and in their own right.

One of the sensitive probes of the QGP is the modification of heavy-quark transverse momentum ( $p_T = \sqrt{p_x^2 + p_y^2}$ ) distributions measured in Pb-Pb collisions with respect to those measured in pp collisions. Heavy quarks experience the whole evolution of the QGP and as such are ideal probes for all the stages of the collision [Col14b].

At the LHC one observes abundant amounts of heavy-quark decay products [Col14a] [Col12a]. Heavy-quarks, charm ( $m_c = 1.27 \pm 0.02 \text{ GeV}/c^2$ ) and bottom ( $m_b = 4.18^{+0.03}_{-0.02} \text{ GeV}/c^2$ ) [ea12] production can be predicted with good precision using the QCD based models. Heavy-quarks include two historical pillars, namely open heavy-flavour hadrons (D and B mesons) and bound states/quarkonia (charm-anticharm, e.g.  $J/\psi$ , and beauty-antibeaity, e.g.  $\Upsilon$ ). This thesis will focus on open heavy-flavour hadrons or "heavy-flavour", which are hadrons containing a charm (anticharm) or beauty (antibeaity) quark and a light antiquark (quark).

Lower mass heavy-flavour hadrons decay weakly and have a lifetime of  $\sim 0.5 - 2 \text{ ps}$  with a decay length,  $c_\tau$ , of  $\sim 100 - 500 \text{ mm}$  due to relativistic effects (the Lorentz factor defined as  $\gamma = 1/\sqrt{1 - v^2/c^2}$ ). Their decay vertices are displaced by hundreds of mm from the primary vertex. Two of the possible decay modes are the hadronic decay channel with branching ratios (B.R.) of  $\sim 55\%$ , and the leptonic decay channel with branching ratios (B.R.) of just above 10%.

Heavy-flavour production in high energy pp collisions is important for providing information about the mechanisms involved in parton interactions, in particular in the small Bjorken- $x$  regime [Zha12]. The partonic hard-scattering process can be calculated with pQCD down to low  $p_T$ .

In ALICE, muons are measured at forward pseudorapidity ( $-4 < \eta < -2.5$ ), using the Muon Spectrometer. The pseudorapidity,  $\eta$  is expressed as,

$$\eta = -\ln \left( \tan \frac{\theta}{2} \right), \quad (1.3)$$

where  $\theta$  is the polar angle of the track with respect to the beam axis (z-axis). Pseudorapidity is the spatial coordinate which describes the trajectory of the particle. Various track cuts are used to reduce background in the measurement of muons. Heavy-flavour measurements at forward rapidity with the ALICE Muon Spectrometer allow access to small Bjorken- $x$ , probing a range of  $x$  below  $10^{-4}$  which provides parton distribution function (PDF) information. A PDF is defined as the probability density for a parton to carry the momentum fraction  $x$  of a proton at a resolution scale  $Q^2$ , where  $Q$  is the energy scale of the hard interaction. At large  $Q^2$ , heavy-flavour hadrons are produced in initial hard parton scatterings. The dynamics of the interacting system within such a proton can be expressed in terms of PDFs [Tho18].

ALICE measurements of heavy-quarks are complementary to other LHC measurements as the pseudorapidity range of the ALICE Muon Spectrometer complements the region reached at LHCb while the ALICE Central Barrel complements the region reached at both CMS and ATLAS.

This Chapter consists of the theoretical background, a literature review of studies conducted at the LHC in the heavy-flavour sector, the motivation and aims as well as the outline of this study.

## 1.2 Theoretical basis

This section discusses the theoretical background relevant to this study. A brief overview of the Standard Model of particles will be given, with emphasis on Quantum Chromodynamics (QCD), the theory that governs the strong interaction. The Standard Model of particles is an important introduction before discussing the physics conducted at the Large Hadron Collider (LHC), especially for heavy-flavour production in high energy pp collisions.

### 1.2.1 The Standard Model of particles

The Standard Model of particles describes the fundamental constituents of matter, namely quarks, leptons and gauge bosons, where quarks and leptons are matter constituents, gauge bosons are force carriers, and the Higgs boson accounts for the mass of elementary particles. In Figure 1.2 one can see all known elementary particles and their corresponding mass, charge and spin. The Standard Model of elementary particles consists of 3 generations of fermions with half-integer spin, namely quarks and leptons, with each group composed of pairs of particles exhibiting similar physical behaviour. The six quarks are also referred to as flavour. The first generation of quarks consists of the up (u) and down (d) quarks, the second generation of quarks consists of the charm (c) and strange (s) quarks, and the third generation consists of the bottom (b) and top (t) quarks.

Charm, bottom and top quarks are named "heavy-quarks" or "heavy-flavour" as they have the largest masses, in the order of  $\text{GeV}/c^2$ , compared to the lighter quarks which are of the order of  $\text{MeV}/c^2$ . All quarks have fractional charges (-1/3 or +2/3) and have an additional intrinsic property called colour charge and interact by the exchange of force carrying particles called gluons. The six leptons consist of the similar three generations, where each lepton has a corresponding neutrino. Leptons interact via three fundamental interactions, namely gravitation by the gravitational force, the weak interaction by the weak force and electromagnetism by the electromagnetic force. The first generation of leptons consists of the electron (e) and electron neutrino ( $\nu_e$ ), the second generation consists of the muon ( $\mu$ ) and the muon neutrino ( $\nu_\mu$ ), and the third generation consists of the tau ( $\tau$ ) and the tau neutrino ( $\nu_\tau$ ).

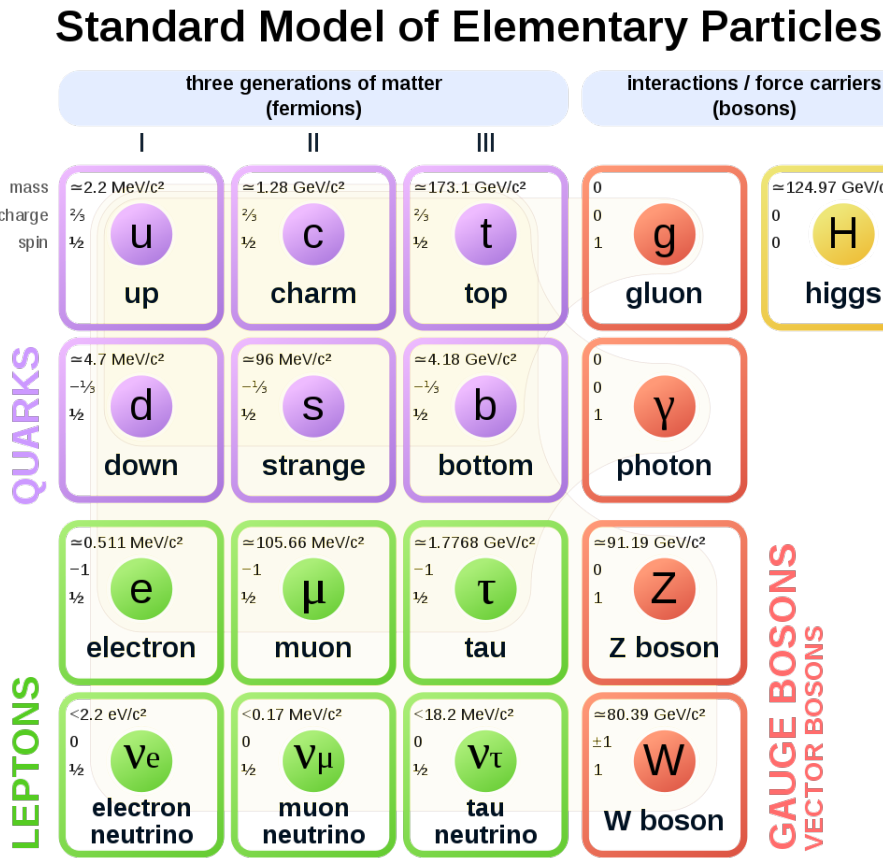


**Figure 1.2:** "The Standard Model of Elementary Particles" [fPPPI]

For each quark and lepton there is an antiparticle, namely the antiquark and antilepton. These antiparticles have equal mass yet opposite physical sign, namely the electric charge and magnetic moment [oEB].

All known fundamental forces are transmitted via force carriers, called gauge bosons, as seen in the fourth column of Figure 1.2. An example of a gauge bosons is the gluon which confines quarks as hadrons. There are four gauge bosons, namely the gluon ( $g$ ), the photon ( $\gamma$ ), the  $Z$  boson ( $Z$ ) and the  $W^\pm$  bosons ( $W$ ). Bosons have integer spin, as opposed to fermions with half-integer spin. The first three gauge bosons, namely the gluon, photon and  $Z$  boson, have no electric charge, however the gluon carries a color charge. The  $W$  boson is the only gauge boson to carry electric charge, of either  $+/- 1$ . The Higgs boson, in the fifth column, has spin 0 and no charge. It is the Higgs boson that is responsible for giving mass to elementary particles. The Higgs boson, or Brout-Englert-Higgs particle, was discovered and confirmed to have a mass of  $125.09 \text{ GeV}/c^2$  by the ATLAS and CMS experiments at the LHC [Col12e] [Col12d]. The  $W$  and  $Z$  bosons are known as the intermediate vector bosons and are responsible for the mediation of the weak interaction. The photon

has zero mass and exists only as moving particles. It has no electric charge, carries energy and momentum and is able to interact with other particles such as electrons. It interacts via the electromagnetic interaction. The photon interacts via the Compton effect, photoelectric effect and electron-positron pair production ( $e^-/e^+$ ).

The gluon is the carrier of the strong force which is responsible for confining quarks ( $q$ ) and anti-quarks ( $\bar{q}$ ) into hadrons. Hadrons are separated into two groups called mesons and baryons where mesons consist of a quark and an anti-quark held together by gluons, and baryons consist of three quarks held together by gluons.

### 1.2.2 Quantum Chromodynamics (QCD)

Quantum Chromodynamics is the theory that describes the action of the strong nuclear force or strong interaction. QCD postulates the existence of the strong colour charge, a quantum property introduced in order to account for known hadrons, associated with quarks and gluons [Kha06]. As we know, each quark (anti-quark) has a 'colour' of either red, green or blue (anti-red, anti-green or anti-blue). The total colour charge of hadrons is required to be zero, that is it requires the conservation of colour charge. Thus requiring mesons to consist of two quarks, a quark and anti-quark pair ( $q\bar{q}$ ) as mentioned earlier, and baryons to consist of three quarks, either all three quarks ( $qqq$ ) or all three anti-quarks ( $\bar{q}\bar{q}\bar{q}$ ). Gluons carry one colour charge and one anti-colour charge. This means that gluons are able to couple to quarks as well as themselves. In terms of perturbative QCD theory, gluons are exchanged within hadrons through a virtual emission and absorption process. Gluon transfer between quarks exchange a colour charge, for example, if a blue quark emits a blue anti-red gluon, it becomes red and if a blue quark absorbs a red anti-blue gluon it becomes red.

QCD is an aspect of quantum field theory called the non-abelian gauge theory, with symmetry  $SU(3)$ , also called flavour symmetry theory. There are two different types of  $SU(3)$  symmetries, namely  $SU(3)$  flavour symmetry of light quarks and  $SU(3)$  colour symmetry of the quark and gluon dynamics. The  $SU(3)$  flavour symmetry group results from the universality of quark-gluon couplings. In QCD colour charge is conserved in the interactions of quarks, antiquarks, and gluons. The  $SU(3)$  colour symmetry group results from the colour charge which accounts for the strong interactions of quarks and gluons [Tho18]. QCD theory indicates that the potential between two heavy-quarks, such as bottom or charm, is of the form,

$$V(r) = \frac{-\alpha(r)}{r} + \sigma r \quad (1.4)$$

where  $r$  is the distance between the quarks,  $\alpha$  is the coupling constant of coloumb-like terms and  $\sigma$  is the string constant which gives the strength of the

quark confinement [Bet07]. The first term dominates for small  $r$  and the second term dominates for large  $r$ , thus the potential energy of two quarks increases as the distance between them increases until such state in which there is enough energy present to form a new quark-anti-quark pair. The binding force of the quarks increases as the distance between them increases. As a result of the potential energy increase, pairs of quarks and anti-quarks are formed, that is hadrons are formed. As a result, quarks are always observed as part of a two- or three- quark state and never seen individually. This state of hadronisation, where hadrons are formed, is known as confinement.

As a result of colour confinement, quarks cannot be observed directly but only at the hadron level once hadronisation has occurred. This confinement is due to the force-carrying gluons having colour charge. However, the colour force experienced by quarks in the direction that holds them together remains constant regardless of the distance between them. This is described using the QCD coupling constant mentioned earlier,  $\alpha$ . The strong coupling constant,  $\alpha_s$  is defined as,

$$\alpha_{QCD}(Q^2) = \alpha_s = \frac{4\pi}{(11 - 23n_f) \log \frac{Q^2}{\Lambda_{QCD}^2}} \quad (1.5)$$

where  $Q^2$  gives the scale of the interaction,  $\alpha_{QCD}$  and  $\alpha_s$  are the QCD coupling constants,  $n_f$  is the number of flavours and  $\Lambda_{QCD}^2$  is the QCD scale parameter determined by the experiments. This QCD coupling constant's relation to the scale of the interaction is illustrated in Figure 1.3 [Bet07] where it is shown that the intensity of the strong interaction diminishes at short distances (high energies). For low energies, or small  $Q^2$  in the context of Figure 1.3, the strong coupling constant has large values  $\gg 1$ . For high energies, such as that of the LHC, the momentum transfer is large and thus  $\alpha_s$  becomes small, indicating that the quarks and gluons interact weakly. In such conditions perturbation theory techniques are applicable for studying perturbative QCD (pQCD). The pQCD calculations cannot compute cross sections directly as the cross section is a combination of short and long distance behaviour and thus a theorem for QCD factorisation was developed which is able to calculate high energy cross sections, where the cross section is given in Equation 1.4 [SS89].

$$\sigma_{AB} = \sum_{a,b} \int dx_a dx_b f_A^a(x_a, \mu_F^2) f_B^b(x_b, \mu_F^2) \hat{\sigma}(x_a, x_b, \alpha_s(\mu_R^2)). \quad (1.6)$$

This method of QCD factorisation separates long distance behaviours from that of short distance behaviours in a systematic manner. Furthermore, pQCD calculations use certain factorisation properties to separate the cross section into two parts. The first being the short-distance parton cross section and the second being the universal long-distance functions which predict particle

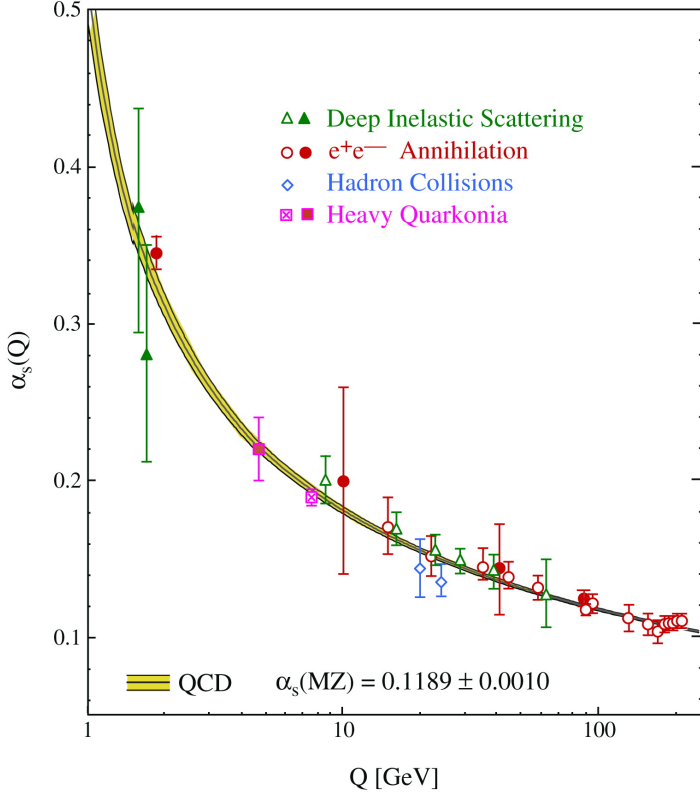


**Figure 1.3:** The QCD coupling constant  $\alpha_{QCD}$  as a function of  $Q$ , the scale of the interaction [Bet07].

reaction processes such as PDFs. PDFs express the distribution of quark momenta within a nucleon whereby the quarks within the parton interact with each other through the exchange of gluons. There are numerous good quantitative tests of pQCD at collider facilities. Heavy-quark production serves as a test of pQCD at ultra-relativistic energies[Mhl15].

### 1.2.3 Heavy-flavour production

The available models used for corrections of heavy-flavour cross section calculations results are leading order (LO) processes, namely fixed-order-next-to-leading-logarithm (FONLL), which matches the resummation of logarithms of the transverse momentum ( $p_T$ ) over the mass of the quark, next-to-leading-logarithm (NLO) and next-to-next-to-leading-logarithm (NNLO) [ea18]. The LO processes in hadronic collisions are heavy-flavour creation via quark-anti-quark annihilation ( $q\bar{q} \rightarrow Q\bar{Q}$ ), gluon-gluon fusion ( $gg \rightarrow Q\bar{Q}$ ), flavour excitation ( $qQ \rightarrow qQ$ ,  $gQ \rightarrow gQ$ ) and final-state gluon splitting ( $g \rightarrow Q\bar{Q}$ ). Gluon fusion ( $gg$ ) has a much higher cross section than quark-anti-quark annihilation for high energy partonic systems such as at the LHC and is therefore the dominant heavy-flavour creation process. The Feynman diagrams for the given

processes are shown in Figure 1.4.

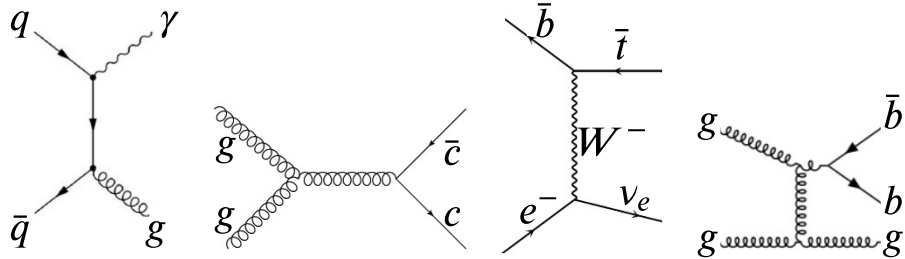


**Figure 1.4:** Feynman diagrams depicting the LO processes, from left to right, quark-antiquark annihilation, gluon-gluon fusion, flavour excitation and gluon splitting.

Heavy-quarks decay via the weak interaction, for example the bottom-quark may decay into a lighter quark such as the charm- or a down-quark, similarly the charm-quark may decay into a lighter quark such as the strange- or up-quark.

$$\begin{aligned} b &\rightarrow c \text{ or } d, \\ c &\rightarrow s \text{ or } u. \end{aligned}$$

They can also decay into lighter hadrons, such as pions or kaons, or to leptons, such as muons, which is the decay process relevant to this study. In particular, this study measures the production of heavy-flavours via the single muon decay channel. An example of heavy-flavour decay via the single muon decay channel is  $B^-$  ( $b\bar{u}$ ) decaying into a single muon and anti-neutrino. The Feynman diagram for such a process is shown in Figure 1.5 where the QCD model of the  $B^-$  meson is illustrated on the left and the decay to a muon and anti-neutrino via the exchange of a  $W^-$  boson is shown on the right [Shi08].

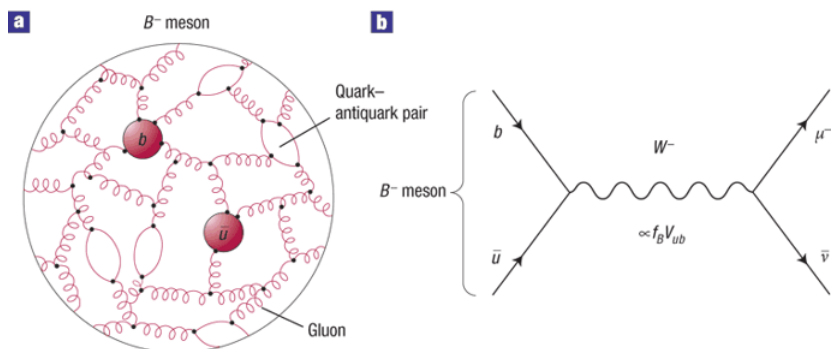


**Figure 1.5:** QCD meson and Feynman diagram of heavy flavour decay via a semi-leptonic decay channel [Shi08].

### 1.3 Literature Review

Heavy-flavour production in pp collisions at the LHC represent an important test of pQCD. Heavy-flavour are produced almost exclusively in initial hard partonic scatterings and therefore the framework of pQCD can be used to estimate their production cross sections. Theoretical developments have indicated that the ratio of heavy-flavour production cross sections between different beam energies and different rapidity intervals are key observables that are expected to be sensitive to the gluon PDFs [MN15].

The ALICE Collaboration has studied heavy-flavour production at mid-rapidity ( $|\eta| < 0.9$ ) via the hadronic decay channel [Kra12] [NO07] and semi-electronic decay channel [Col12b] [Col16b], and at forward rapidity ( $-4 < \eta < -2.5$ ) via the single muon decay channel [Col14b] in pp collisions at  $\sqrt{s} = 7$  TeV. In these studies, results were compared to FONLL [Nas98] and GM-VFNS (general-mass variable-flavour-number-scheme) [Kra12] theoretical predictions. These models are based on pQCD theory. The measurements of D-mesons (e.g.  $D^+(c\bar{d})$ ) at mid-rapidity fall on the higher side of FONLL predictions and the lower side of GM-VFNS predictions, but within uncertainties [Kra12]. However, measurements of prompt  $\Lambda_c^+$  (udc) are underestimated by GM-VFNS predictions [NO07]. Measurements of heavy-flavour decay electrons at midrapidity are in agreement with FONLL calculations [Col16b], as are heavy-flavour decay muons at forward rapidity [Col14b] in pp collisions at  $\sqrt{s} = 7$  TeV.

Published results ([Col14a][Col12a]) of the energy dependency of the total cross section at the LHC are shown in Figure 1.6 where the measurements for bottomonium [Col14a] and charmonium [Col12a] are presented in the top and bottom figures, respectively. These measurements are compared with results from other LHC experiments, results from low energy experiments and theoretical calculations by means of FONLL [Nas98] and MNR [NR92]. From the figure it is clear that the cross section increases with increasing energy. Furthermore, LHC results, including those from ALICE, are higher by a factor 10 for bottomonium and 100 for charmonium. This indicates that the LHC produces an abundance of charm and bottom, thus it is an ideal environment to study heavy-flavour production.

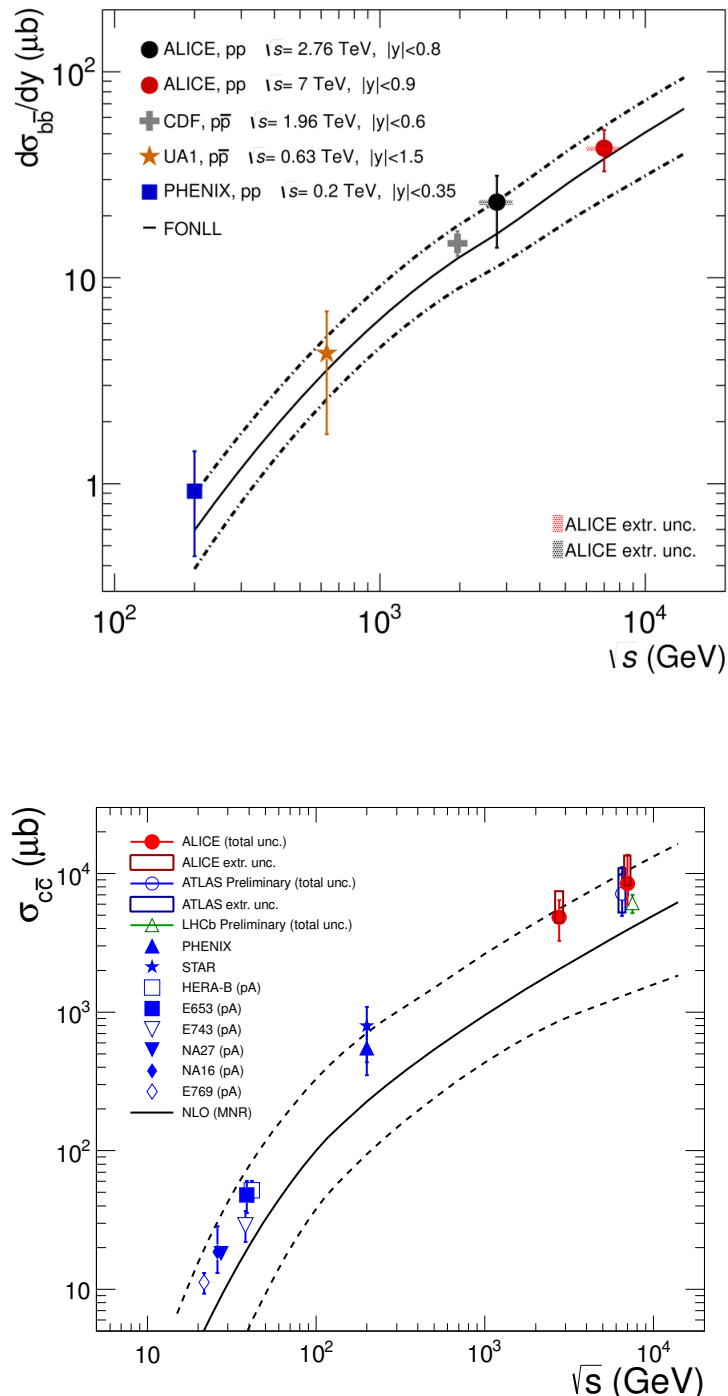


**Figure 1.6:** Energy dependence of the total nucleon-nucleon charm ( $c\bar{c}$ ) and beauty ( $b\bar{b}$ ) production cross sections [Col14a] [Col12a].

These results provide an indication of how the ratio of open heavy-flavour production cross sections between different centre-of-mass energies can serve as a sensitive test of pQCD-based calculations and to constrain the gluon PDF at forward rapidity.

Results from heavy-flavour measurements at forward rapidity in pp collisions at  $\sqrt{s} = 2.76$  [Col12c] and 7 TeV [Col14b] and most recently at  $\sqrt{s} = 5.02$  TeV [Col17b] have been published. At  $\sqrt{s} = 5.02$  TeV [Col17b], a wider transverse momentum interval,  $2 < p_T < 20$  GeV/c, was reached. Evidently, the results were more precise compared to those performed in the same rapidity at  $\sqrt{s} = 2.76$  TeV [Col12c] and 7 TeV [Col14b]. Figure 1.7, taken from [Col17b], shows a ratio of data to FONLL calculations at  $\sqrt{s} = 7$  TeV. This ratio shows a smooth increasing trend from  $p_T = 2$  GeV/c to  $p_T = 12$  GeV/c, this is the region of interest for heavy-flavour studies. A comparison with FONLL predictions [Nas98] shows a good agreement between data and FONLL.

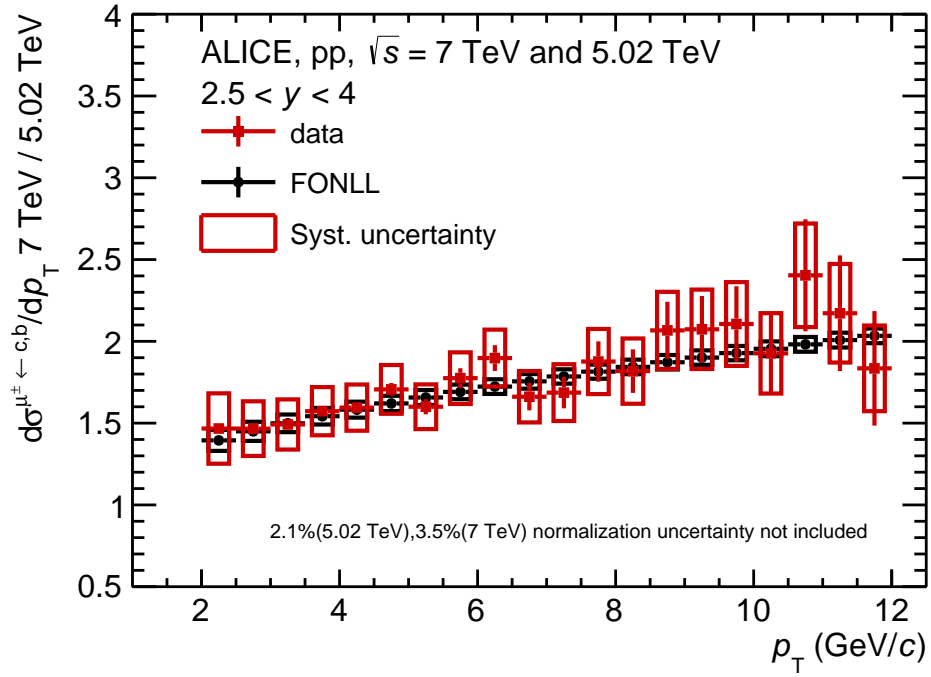


**Figure 1.7:** Ratio of the  $p_T$ -differential production cross sections of muons from heavy-flavour hadron decays at forward rapidity in pp collisions at  $\sqrt{s} = 7$  TeV to those at  $\sqrt{s} = 5.02$  TeV [Col17b].

## 1.4 Motivation and Aims of the Study

The study is motivated by recent ALICE measurements of heavy-flavour production via the leptonic decay channels, shown in Table 1.1, at lower LHC energies which were well reproduced by FONLL calculations [Col17b] [Col12c] [Col14b] [Col16b]. The aim is to study heavy-flavour hadrons produced in

Decay process
$70\% D^0 + 30\% D^+ \rightarrow \mu + X$
$B \rightarrow \mu + X$
$B \rightarrow D \rightarrow \mu + X$

**Table 1.1:** The heavy-flavour production processes considered in this study.

pp collisions at  $\sqrt{s} = 13$  TeV with ALICE, focussing on the decay channel into muons. The heavy-flavour decay muon channel contributes to the total inclusive  $p_T$ -differential muon yield reconstructed with the ALICE Muon Spectrometer. This measurement will be carried out at forward rapidity ( $-4 < \eta < -2.5$ ) where the Muon Spectrometer is situated in ALICE. The Muon Spectrometer provides a clean detection of muons, in particular single muons [Mhl15]. Observables like the minimum momentum ( $p$ ) of 4 GeV/c and the minimum  $p_T$  for trigger of 0.5 GeV/c are achieved with the Muon Spectrometer.

The forward rapidity region probes the small Bjorken- $x$  region ( $x < 10^{-4}$ ). The results presented in this thesis will also explore a wider  $p_T$  range, as was the case in [Col17b] and [Mar17]. The results can be used to compare heavy-flavour production cross sections at an additional centre-of-mass energy of  $\sqrt{s} = 13$  TeV, the highest energy currently reached by the LHC, to previous results at lower centre-of-mass energies. The results obtained could provide PDF information at a pseudorapidity complementary to other LHC experiments. These results will serve as a test for pQCD model calculations.

## 1.5 Layout

The thesis is organised as follows:

- Chapter 2 provides an outline of the ALICE Experiment, focusing on the detector most relevant to the study, that being the Muon Spectrometer. The general LHC beam conditions and how the ALICE Experiment makes use of the beams provided by the LHC is explained. The necessary

data taking conditions are described before introducing the data analysis.

- Chapter 3 is dedicated to the analysis of the data sample used and analysis strategy followed. This includes a brief explanation of the ALICE offline framework. The FONLL model calculations relevant for the study are discussed and used in determining the detector acceptance and efficiency.
- In Chapter 4 the final results of single muon inclusive production cross sections as a function of transverse momentum and pseudorapidity are presented. These experimental results are compared to the FONLL model calculations and discussed.
- Chapter 5 provides a summary and conclusion.

# Chapter 2

## The ALICE experiment

CERN, the European Organisation for Nuclear Research, is a research organisation that operates the largest particle physics laboratory in the world. The organisation is located on the France-Switzerland border near Geneva. Here one can find the Large Hadron Collider (LHC), which is the world's largest and most powerful particle collider and the world's largest machine [CER19]. The LHC is 27 km in circumference and between 50 - 175 m below ground [CERa]. This particle collider is able to collide protons with protons, protons with lead, and lead with lead, however the LHC primarily collides proton beams. There are 4 experiments along the LHC. At points 1, 2, 5 and 8 one can find ATLAS, ALICE, CMS and LHCb, respectively, as can be seen in Figure 2.1.

ALICE, A Large Ion Collider Experiment dedicated to HIC, is unique in that it is able to identify and measure with precision, many particles produced in the collisions with low momentum down to 100 MeV/c. These unique qualities are due to the fact that ALICE has more different types of detectors than any other experiment at the LHC.

This Chapter introduces the ALICE experimental setup in detail. The focus of this chapter is on detectors required for the study of heavy-flavour decay muons. These include the trigger detectors and the Muon Spectrometer. Furthermore, the description of the conditions for collisions of the proton beams and the data taking procedures in ALICE, in particular, for obtaining the data set used in this study will be given.

### 2.1 ALICE at the LHC

At Point 2 of the LHC is the ALICE detector shown in Figure 2.2. The ALICE detector consists of two main parts, the Central Barrel and the Muon Spectrometer. The central barrel is located symmetrically around the interaction point ( $z = 0$  cm) with the Muon Spectrometer located on the C-side ( $z > 0$  cm). One denotes the side of the interaction point for  $z < 0$  cm as the A-side. The Central Barrel is enclosed by the L3 solenoid magnet with a magnetic

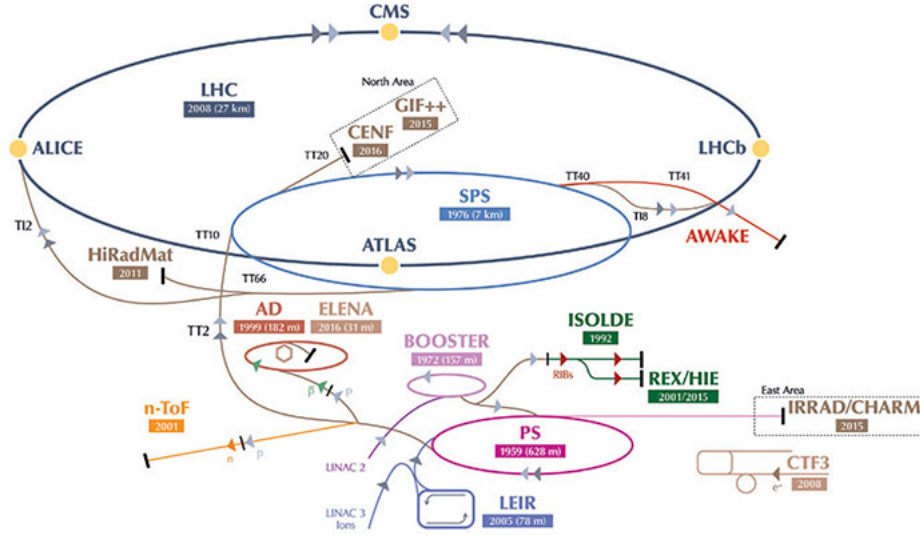


**Figure 2.1:** CERN accelerator complex [BW17], showing a schematic view of the LHC and its injection scheme as well as other ongoing CERN experiments.

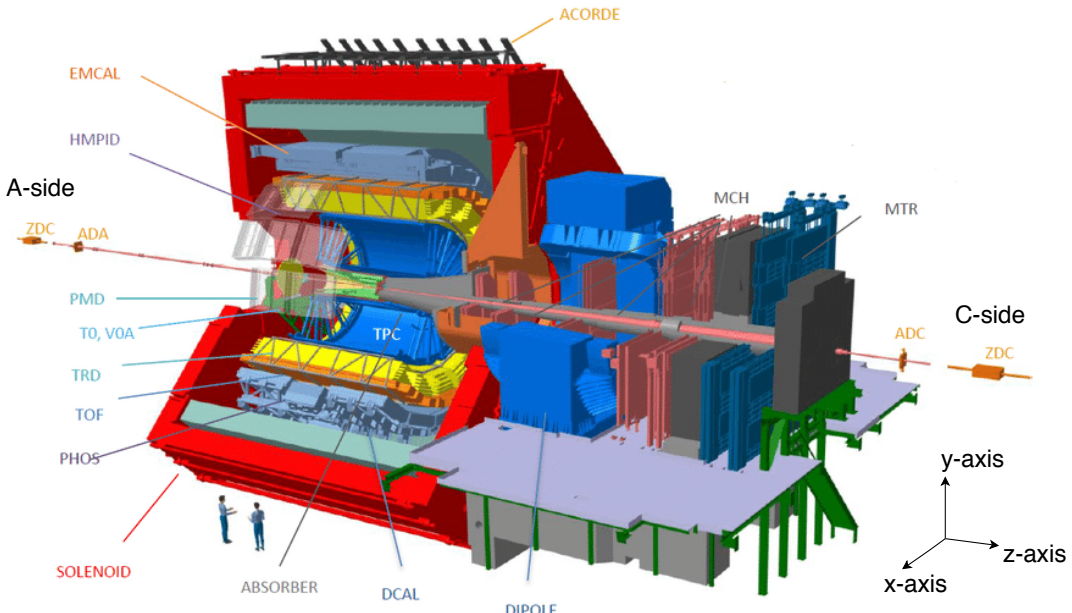


**Figure 2.2:** The ALICE Detector [Pal17].

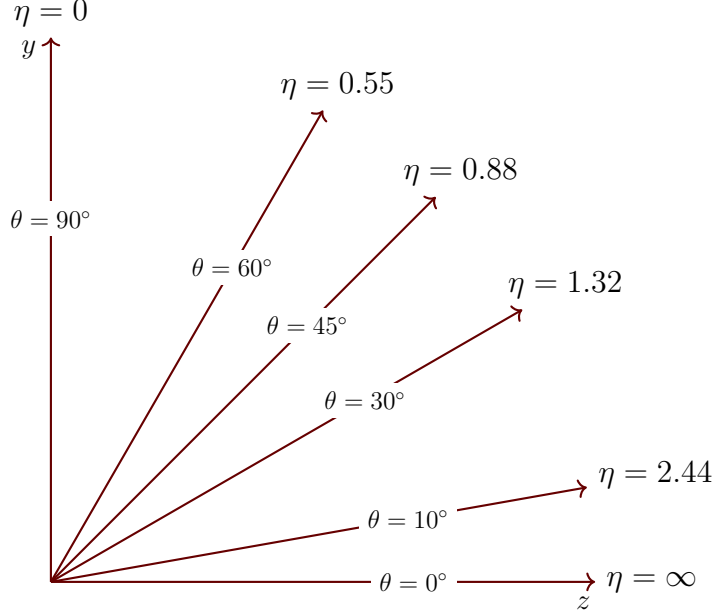


**Figure 2.3:** Pseudorapidity and  $\theta$  angle relation in the  $yz$ -plane.

field of 0.5 T and covers the full azimuthal region  $|\eta| < 0.9$  where  $\eta$  denotes the ALICE reference frame pseudorapidity, as described in Equation 1.3 and illustrated in Figure 2.3.

The detectors in the Central Barrel measure the event information, such as the time an event took place, as well as the track left by a charged particle and the identity of each particle, where the measured particles are hadrons, electrons and photons. The Inner Tracking System (ITS) is the detector in ALICE closest to the beam axis and interaction point. The ITS consists of six layers of detectors, namely the two innermost layers of Silicon Pixel Detectors (SPD) which will be used in this study, two intermediate layers of Silicon Drift Detectors (SDD) and two outermost layers of Silicon Strip Detectors (SSD) [Mil13]. The main purpose of the ITS is to reconstruct the primary and secondary vertices, to track and identify charged particles with a low  $p_T$  cutoff and to improve the momentum resolution at high  $p_T$ . ALICE has excellent particle identification (PID) capabilities, which spans over a continuous momentum interval and utilises all available detector technologies. More details of the different components of the ALICE detector can be found in [Col08].

The following section covers only the detectors used in the measurements of heavy-flavour decay muons, namely the Muon Spectrometer and the trigger detectors which include the VZERO detector, the Silicon Pixel Detector, and the TZERO detector. Following this, the different triggering techniques and LHC beam conditions will be described, as well as the data taking conditions enforced by the LHC.

## 2.2 The ALICE Muon Spectrometer

The measurement of all muons at forward rapidity is done using the forward Muon Spectrometer [Col99] in the pseudorapidity region  $-4.0 < \eta < -2.5$ . The Muon Spectrometer covers physics of heavy-flavour, quarkonia and the W and Z vector bosons. It consists of a front absorber, inner beam pipe shielding, a passive muon filter, a dipole magnet, tracking chambers and trigger chambers. These components will be explained in detail.

### 2.2.1 Front absorber

The front absorber is made up of carbon, concrete and steel, as shown in Figure 2.4 and is 10 interaction lengths long (4.13m [Col14c]), which is the radiation length related to the energy loss of high energy particles. Before the front absorber, to the left of Figure 2.4, is the interaction point, and after the front absorber, to the right, is the Muon Spectrometer. The front absorber is used to reduce the contribution of hadrons, photons, electrons and muons from light hadron decays except muons coming from the interaction point and its surrounding region with  $p_T$  above a certain threshold ( $p_T > 0.5$  or  $4.2$  GeV/c) to be determined by the specified muon trigger. The thresholds relevant to this study are introduced and defined in Chapter 3.2.1.

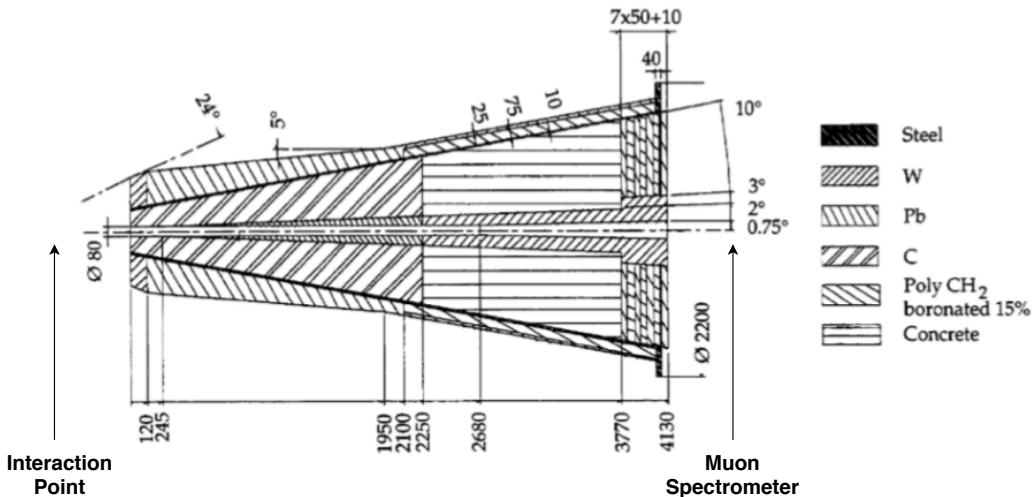


**Figure 2.4:** The Front Absorber [Col00], where the units used are in cm.

### 2.2.2 Inner shielding

In order to protect the Muon Spectrometer against the production of secondary particles produced in the beam pipe, the beam pipe shielding geometry called

for a conical shape instead of cylindrical so as to avoid production of secondary particles along the length of the spectrometer. The beam shield is made of tungsten, lead and steel covering a theta angle up to two degrees ( $\theta < 2^\circ$ ). The Inner Beam Shield protects the tracking and trigger chambers from particles produced at large rapidities, that is, particles originating from the beam pipe itself and not the interaction point [Col99].

### 2.2.3 Muon filter

The passive muon filter is placed between the tracking chambers and trigger stations. It is a 1.2 m thick iron wall of 7.2 interaction lengths, denoted by "iron wall" in Figure 2.5. It absorbs mostly hadrons that punch through the front absorber, secondary hadrons produced inside the front absorber that manage to traverse the tracking stations, as well as low momentum muons ( $p < 4 \text{ GeV}/c$ ) [Col99].

### 2.2.4 Dipole Magnet

A 'warm dipole magnet' of 820 tons was chosen for the dipole magnet [Col99]. This dipole magnet has a 3 Tm field integral and nominal field of 0.7 T. It operates at both polarities. The purpose of the magnet is to assist with particle tracking as the curvature of charged particles, caused by the magnetic field, can be used to identify the momentum of the particle as well as extrapolate the tracks to the parent particle. The magnetic field is perpendicular to the beam direction which is indicated as the x-axis thus defining the bending plane as the zy plane and the non-bending plane as the xz plane [Fin06], which can be seen with respect to the Muon Spectrometer as shown in Figure 2.5.

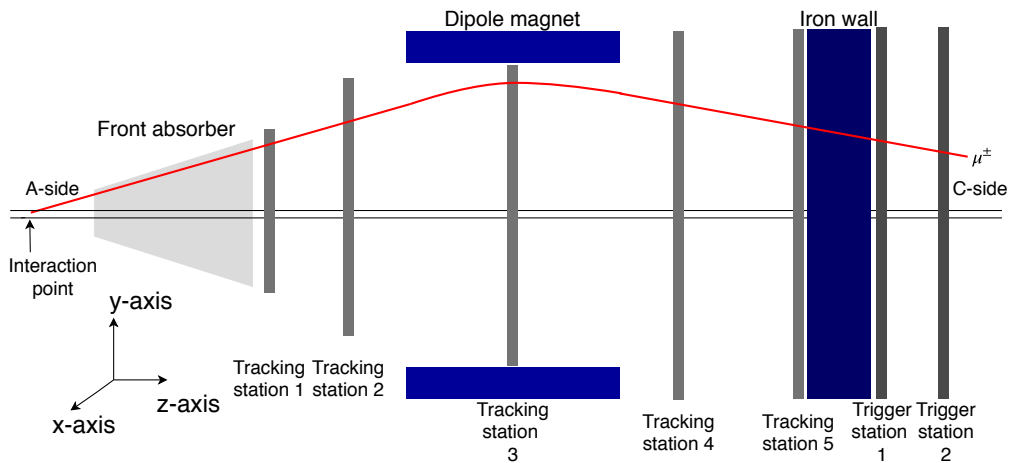


**Figure 2.5:** Schematic representation of the ALICE Muon Spectrometer, with a single muon traversing the Muon Spectrometer, illustrated by the red line.

### 2.2.5 Muon tracking chambers

The detectors used for tracking muons are known as tracking chambers. They make up five tracking stations, two of which are mounted in front of the dipole magnet, one inside the dipole magnet, and two stations behind the dipole magnet, as can be seen in Figure 2.5. Each tracking station is defined by a bending plane (zy-plane) and non-bending plane (xz-plane). Each plane is covered by a set of Cathode Pad Chambers. These Cathode Pad Chambers are based on a multi-wire proportional chamber principle and are gas detectors [Col14b]. They use a gas mixture of 80% Ar and 20% CO<sub>2</sub>. The front two tracking stations (stations 1 and 2) consist of quadrant-type chambers while the other three tracking stations are slat-type. The front two tracking stations are placed 5.4 m and 6.86 m from the interaction point, whereas the other three tracking stations are placed 9.75 m, 12.49 m and 14.49 m from the interaction point. The overall spatial resolution of the tracking chambers is 100 $\mu$ m. The two cathode planes are both read out in order to provide a two-dimensional hit information. In the first station the innermost region provides position information such as the coordinate of a hit in the bending plane and the position of the wire in the nonbending plane [Col99]. The first two tracking stations are located in front of the dipole magnet and they cover the smallest surface area as they are closest to the interaction point, observe high particle densities (up to  $4 \times 10^{-2}$  hits/cm<sup>2</sup>) and have two fully implemented cathode planes [Col99]. This imposes a high-granularity readout structure with high-density on-board readout electronics. Tracking station 3 is located inside the dipole magnet. This station sees a lower particle flux compared to the first two with less than  $6 \times 10^{-3}$  hits/cm<sup>2</sup>. As a result, there are induced multiple scattering effects which must be minimized in order to preserve the mass resolution and, as such, a single readout cathode plane with on-board electronics is utilised. Two more tracking stations, stations 4 and 5, are located behind the magnet. Stations 4 and 5 cover the largest surface area and as such pose mechanical problems for the wire lengths and the ability to maintain a large surface planarity and rigidity in the event of hydrostatic overpressure. These two stations utilise both single and multiple readout cathode planes due to their large surface are. A multimodule design with two active cathode planes was suitable [Col99]. The tracking chambers cover a total surface area of 100 m<sup>2</sup> and have a total number of about one million readout channels.

### 2.2.6 Muon trigger chambers

At the back of the Muon Spectrometer there are two trigger stations, each consisting of two planes of Resistive Plate Chambers (RPCs) resulting in a total of 72 RPCs. In Figure 2.5 the trigger stations, 1 and 2, are mounted behind the muon filter, discussed in Chapter 2.2.2. The trigger stations are located between 16 m and 17 m downstream from the interaction point (C-side) and are

operated utilising gas chambers with a gas mixture of Ar (49%), CH<sub>2</sub>F<sub>4</sub>(7%), C<sub>4</sub>H<sub>10</sub> (40%) and SF<sub>6</sub>(4%) [Ver00]. The resistive plate detectors are used for muon identification and triggering. There are two trigger modes, a low- and high- $p_T$  single muon trigger with a minimum  $p_T$  threshold of 0.5 GeV/c, and 4.2 GeV/c , respectively. The RPCs consist of bakelite electrodes separated by a 2 mm gap. These bakelite electrodes are low resistivity electrodes with a resistance of  $\sim 3 - 9 \times 10^9 \Omega$  cm. The outsides are painted in graphite and one side is connected to the high-voltage and the other to the ground. The inside is painted with linseed oil. The signal is received inductively on each side of the detector through copper strips in both the bending and nonbending plane directions. "The copper strips, read-out strips, are connected to front-end discriminators (ADULT), which are adapted to the timing properties of the detector" [Sen17]. The signal is biased in the front-end electronics to transmit a logical signal to the trigger electronics when an analog pulse is validated in the corresponding channel. Local trigger boards can identify single tracks meeting the previously mentioned  $p_T$  thresholds. The regional and global trigger boards collect data that select either dimuon or single muon events. The time resolution is 1-2 ns and the spatial resolution is  $\sim 1$  cm [Sen17] [RL04]. The local trigger board decides whether there is a trigger or not and whether it is a negative or positive muon trigger. The global trigger board collects information from the regional board to provide trigger signals for the Central Trigger Processor (CTP) and thereby to the experiment.

## 2.3 Alignment of the tracking chambers

To maintain the mass resolution of the Muon Spectrometer which is about 100 MeV/c<sup>2</sup>, it is necessary to monitor the position of the tracking chambers with a Geometry Monitoring System (GMS)[vdGHGCGFLR00]. The broadening of the mass resolution is mainly due to the front absorber and the tracking chambers. The broadening contributions from the front absorber are as a result of multiple scattering and energy loss fluctuations. The tracking chamber contributions come from the intrinsic resolutions and multiple scattering. In order to meet the required mass resolution of 100 MeV/c<sup>2</sup> the contributions from the tracking chamber alignment cannot exceed a mass resolution of 44 MeV<sup>2</sup>/c<sup>2</sup>, as required by the GMS[vdGHGCGFLR00]. It is therefore important that the muon tracking chambers are aligned as this can affect the mass resolution in two ways, namely by the relative chamber and global spectrometer misalignment. Relative chamber misalignment will lead to an error in the measurement of the curvature of the bent tracks, caused by the magnetic field of the dipole magnet, and therefore in extracting a wrong value of the momentum of a muon. Thus, the alignment is executed in two steps. First alignment is done using cosmic data, where the dipole magnet is switched off and the initial position of the chambers is measured using straight muon tracks during the

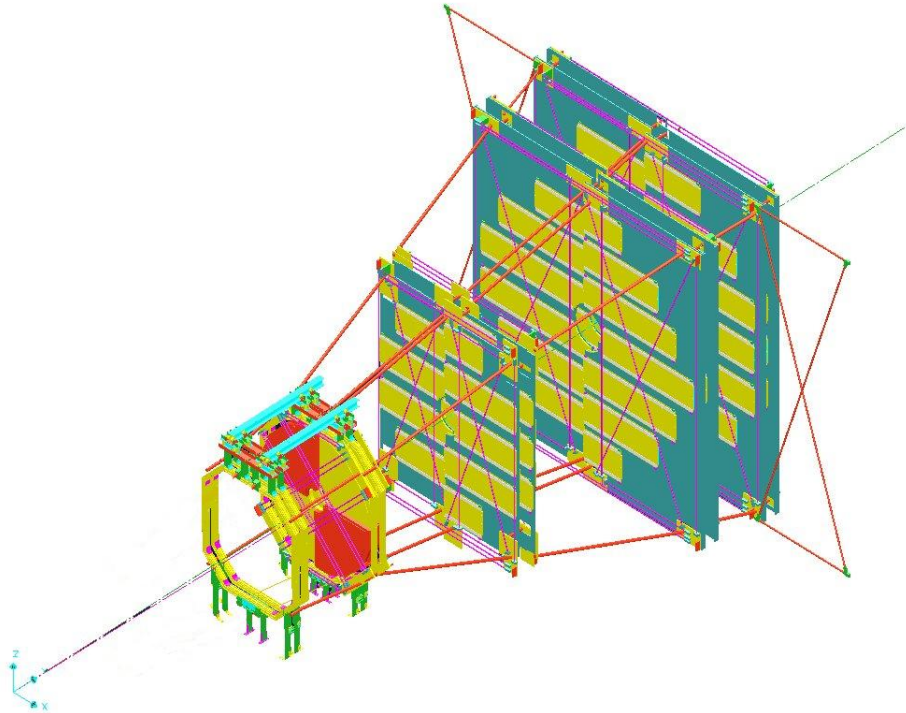


**Figure 2.6:** General view of the GMS setup used to measure relative displacements between the chambers [KT05].

so-called calibration runs with the magnetic field off [vdGHGCGFLR00]. Once this is complete, additional alignment is done with the dipole magnet switched on and the GMS measures chamber displacements during "physics runs" with the magnetic field on. The accuracies of the calibration runs are calculated using simulations [vdGHGCGFLR00]. These displacements are measured using lasers, as indicated by the red lines in Figure 2.6. From these it is possible to determine their displacement of the tracking stations by the relative displacements.

## 2.4 Trigger detectors

The Muon Quality Flag for pp data collected in 2017 is related to a certain set of trigger detectors. Trigger detectors send a signal to the trigger electronic system when collisions occur. In this case, the SPD, V0 and T0 and the Muon Trigger stations are the trigger detectors used. These relevant detectors are discussed. Within the central barrel, notably important detectors used in this analysis are the VZERO (V0) detector, SPD and TZERO (T0) detector. The V0 detector is used for triggering and offline rejection of beam-induced background events [Col12c]. It consists of two scintillator arrays on the A- and C-side, V0A and V0C, located in the forward and backward region of

$2.8 < \eta < 5.1$  and  $-3.7 < \eta < -1.7$ , respectively. The trigger for minimum bias events (MB) in ALICE (CINT) is defined as a logical OR between a signal in the V0A(T0A) or V0C(T0C) detectors along with a signal in the Silicon Pixel Detector (SPD). The SPD is used for the determination of the position of the primary vertex [Col08]. The T0 detector consists of 2 arrays of 12 Cherenkov counters with a photomultiplier tube (PMT). Each array is placed at 72.7 cm (T0-C) and 375 cm (T0-A), on either side of the ALICE interaction point. It is a fast detector used for fast timing, with a fast time response in the order of picoseconds, by providing initial time and provides an L0 trigger signal, the "wake up" signal, which measures the approximate vertex position [Col08]. It also provides a start signal to the Time-of-Flight (TOF) detector in the central barrel which is used for particle identification [Sen17] as well as in van der Meer scans for determining the luminosity.

As described earlier, two Muon Trigger stations of the Muon Spectrometer provide the muon trigger. The two programmable cuts are the low- and high- $p_T$  single muon triggers contributing to these trigger classes, namely CMSL7-B-NOPF-MUFAST (CMSL) and CMSH7-B-NOPF-MUFAST (CMSH), respectively, which are performed in parallel by the trigger electronics. In this study, the low- and high- $p_T$  single muon triggers require the same conditions as the MB trigger, a logical OR between the V0A or V0C with the SPD, with an additional single muon above the specified  $p_T$  threshold that reaches the muon trigger system. The respective low- and high- $p_T$  muon triggers have thresholds of 0.5 GeV/c and 4.2 GeV/c, respectively, which are determined by the inverse proportionality of the momentum to the amplitude of the signal received by the detector.

## 2.5 LHC Beam Conditions

In 2017 the LHC collided proton beams with energies of 6.5 TeV each, resulting in a centre-of-mass energy of 13 TeV. The proton beams are accelerated using a sequence of machines shown in Figure 2.1. First, protons need to be isolated from hydrogen gas. This is done by filling a metal cylinder with hydrogen gas, Duoplasmatron, which is then surrounded by an electric field to dissociate the electrons from the protons. The protons are accelerated up to 100 kV and then sent to an accelerating component that both accelerates and focuses the beam. The particle beam is bunched and accelerated up to 750 keV [CERb]. The beam is then injected into the linear accelerator (LINAC2) where it is accelerated up to 50 MeV. Protons then reach the ring of the proton synchrotron booster (PSB) where the beam is accelerated to 1.4 GeV following which they are injected into the proton synchrotron (PS). In the PS the protons are accelerated to 25 GeV. The PS is responsible for providing 81 bunch packets with 25 ns spacing required for the LHC. Once the beam is ready it is then injected into the super proton synchrotron (SPS) which is 7 km in circumference. The

SPS accelerates the protons to 450 GeV, the injection energy for proton beams in the LHC where they eventually reach the nominal energy of 6.5 TeV. Two beams are injected, one in the clockwise direction and the other in the anti-clockwise direction. While beam one is injected into the LHC near Point 8, beam 2 is injected near Point 2, where ALICE is located [CERb].

### 2.5.1 LHC filling scheme

The filling scheme indicates the spacing between bunches of protons, the number of proton bunches in the LHC ring, and the number of bunches expected to collide at the interaction points. The filling scheme determines the luminosity and the cross section required for the physics of interest. Luminosity is defined as the number of collisions per  $\text{cm}^2$  per second, i.e. higher luminosity implies an increase in the number of collisions.

The convention for naming the filling schemes follows the base structure:  
 $<\text{spacing}>_<\text{Nb}>\text{b}_<\text{IP1/5}>_<\text{IP2}>_<\text{IP8}>_<\text{train length}>_<\text{inj}>$   
 $_<\text{code}>$  where:

- $<\text{spacing}>$  is the time between bunches, 2025 ns, 525 ns, 75 ns, 50 ns or 25ns. This refers to the characteristic bunch spacing used in the main injector batch for the given filling scheme, in nanoseconds. In the case of this study it is 25 nanoseconds.
- $<\text{Nb}>$  denotes the total number of bunches per beam for the given filling scheme. Normally this is identical for both beams. In this case there were 2556 bunches per beam.
- $<\text{IP1/5}>$  indicates the expected number of colliding bunch pairs in interaction point 1 (IP1) and 5 (IP5) for the given filling scheme. IP1 and IP5 are the interaction points of ATLAS and CMS, respectively.
- $<\text{IP2}>$  indicates the number of colliding bunch pairs in interaction point 2 (IP2) where ALICE is located. In this study the number of colliding bunch pairs was 2215.
- $<\text{IP8}>$  indicates the expected number of colliding bunch pairs in interaction point 8 (IP8) where the LHCb detector is located.
- $<\text{train length}>$  shows the maximum length of a train. In this case it was 144 bunches per injection (bpi).
- $<\text{inj}>$  denotes the number of injections per beam, that being 20 for this filling scheme.
- $<\text{code}>$  shows any other useful info.

Each LHC fill is associated with a certain filling scheme [BC03]. For the data taking periods of interest to this study, the filling scheme used is

25ns\_2556b\_2544\_2215\_2332\_144bpi\_20inj.

### 2.5.2 Beam Modes

ALICE operations are guided by the LHC status. The LHC cycles over the modes shown in Figure 2.7, which shows the time sequence of the different modes of the LHC within a fill. While beam 1 and beam 2 are shown in blue and red, respectively, the energy is shown in black. The x-axis indicates the time and the y-axis indicates the beam intensity and energy (GeV), respectively.

ALICE alternates between the various states depending on the beam mode.

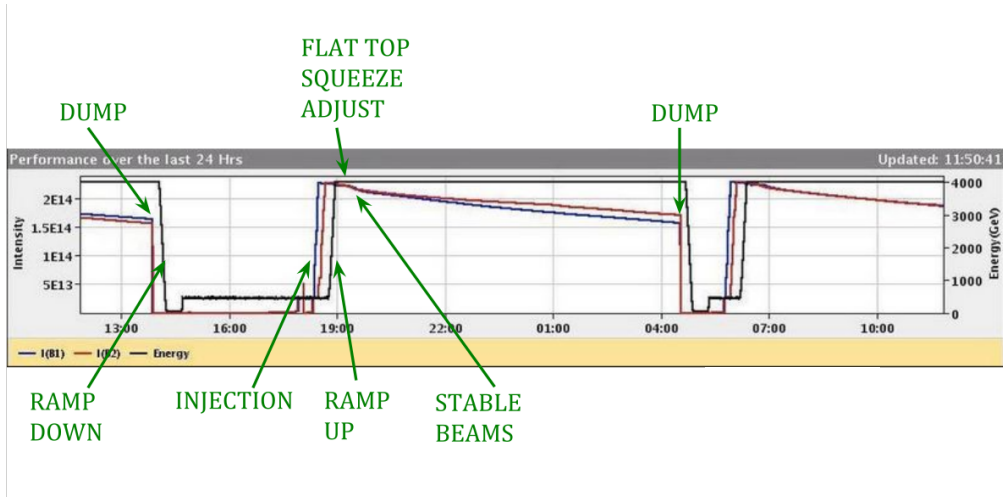


**Figure 2.7:** A typical sequence of LHC Beam Modes within a fill.

The LHC is first injected with proton beams circulating in each beam pipe in opposite directions. For instance, ALICE has to stay (super)SAFE during certain machine operations that could be deemed "unsafe" for the detector, e.g. beam commissioning, beam loss studies, etc. Table 2.1 summarizes the ALICE operations in accordance with the LHC modes. In preparation for injection, the LHC issues the "Handshake", which requires each experiment to be ready for beam injection. Once the warning has been acknowledged, a "handshake" takes place between the experiment and the LHC. At this stage ALICE is in SAFE mode.

After the injection, the LHC goes through a sequence of modes, during which ALICE alternates between various states in preparation for data taking. Before data taking, some of the ALICE subsystems have to perform

calibration runs, subsequently ALICE is in CALIBRATION mode. These run are performed from RAMP to ADJUST, while for other detectors, calibrations can also be done at RAMP DOWN, e.g. the Muon Trigger detector, as described in Table 2.1, when the front-end electronics get conditioned for data taking. For the muon tracking chambers, a pedestal run is taken, when the detector is in the state BEAM\\_TUNING, where the low voltages (LVs) are on at  $\pm 3$  V, and the high voltages (HV) are at an intermediate value (1200V) [Col99]. This happens at beam mode ADJUST. At this high voltage there is no gain of particles crossing the tracking chambers. During this run the pedestals are measured and the thresholds computed in order to correct for the gain dispersion and noise, so that the impact points can be accurately determined [Col09]. Once the beams have been adjusted and are prepared for collisions under stable conditions, the LHC declares STABLE BEAMS. At this point, ALICE is moved to READY mode which means that all detectors are fully biased (HV gains are at operational values, the operational HV for the Muon Tracking Chambers is 1650 V thus suppressing any static background noise) and are ready to take data. The operational HV for the Muon Trigger Chambers is 9400 V. During STABLE BEAMS ALICE takes data until a BEAM DUMP occurs. The BEAM DUMP occurs when beams have been dumped. Then the magnets in the LHC are ramped down and mode changes to RAMP DOWN. Each fill can last more than 10 hours [CERb].

## 2.6 Data Taking Conditions

Each ALICE data taking period has different conditions. A summary of the data taking conditions that applied to the two data taking periods during pp collisions in 2017 is given in Table 2.2.

The data taking periods, LHC17h and LHC17k, analysed were taken with pp collisions in 2017, during Run 2, at  $\sqrt{s} = 13$  TeV. Beam and magnet related conditions are specified for the period of interest in Table 2.2. For this study the "muon cluster" is utilised. A group of detectors that read out together are called a trigger cluster. In this case, the "muon cluster" are the detectors in the forward Muon Spectrometer (muon tracking and trigger) read together with the SPD, V0 and T0, as they have well-matched readout characteristics [Bai19]. This cluster has a faster read out than detectors in the central barrel and, as such, can be distinguished separately in the trigger. Each detector has different trigger conditions which are taken into account. Figure 2.8 illustrates the integrated luminosity. The integrated luminosity delivered to ALICE for pp at 13 TeV, for data taking period LHC17h and LHC17k, is approximately  $39.86 \text{ pb}^{-1}$ . For the triggers relevant to this study, in particular, the low- and high- $p_T$  single muon triggers used in this analysis are shown in grey and

---

<sup>1</sup> $\beta^*$  is the amplitude function at the interaction points. Ideally,  $\beta^*$  must be as small as possible ( $\beta^* = 10\text{m}$ ) [Col16a]

<b>Beam mode</b>	<b>Description of LHC operation</b>	<b>ALICE</b>
INJECTION PROBE BEAM	If either ring of the LHC are injected with or has safe beams circulating within it. Checks are done for different subsystems before injecting higher intensities. The function of this mode is to establish a circulating safe beam with a given lifetime	SAFE (Super Safe (SS) on request)
INJECTION PHYSICS BEAM	The machine has been optimized and the beam has an appropriate lifetime. It is ready to accept higher intensities needed for Physics	SAFE
RAMP UP	Injection completed, preparing the ramp up of the current in the magnets	CALIBRATION
FLAT TOP	Ramp finished, pre-squeeze checks	CALIBRATION
SQUEEZE	Preparing for or "squeezing" the beam as much as possible to increase the number of collisions so at a distance of $\beta^*$ from the focus point the beam is also twice as wide	CALIBRATION
ADJUST	Adjusting beams parameters in the vertical and horizontal planes using quadrupole magnets after the squeeze and preparing for collisions	CALIBRATION of muon tracking chambers
STABLE BEAMS	Stable conditions with collisions in the experiments. Small adjustment of beam parameters permitted	READY
DUMP	Programmed or emergency beam dump	READY, SAFE
RAMP DOWN	Ramp down of magnets and cycling after a dump at the end of Physics fill	CALIBRATION of muon trigger system, SAFE

**Table 2.1:** LHC Beam Modes and corresponding ALICE operations [Cola]

black, respectively. The integrated luminosity for minimum bias (INT7) was  $0.016\text{ pb}^{-1}$ , the low- $p_T$  single muon trigger received an integrated luminosity of  $0.77\text{ pb}^{-1}$  and the high- $p_T$  single muon trigger received an integrated luminosity of  $10.9\text{ pb}^{-1}$  [Colb]. The analysis of these data is discussed in the following chapter.

Beam Type	pp
Beam Mode	STABLE BEAMS
Beam Energy	13 TeV
L3 Magnet Current	-30kA
Dipole Magnet Current	-6kA
Partition	Physics

**Table 2.2:** Data taking conditions

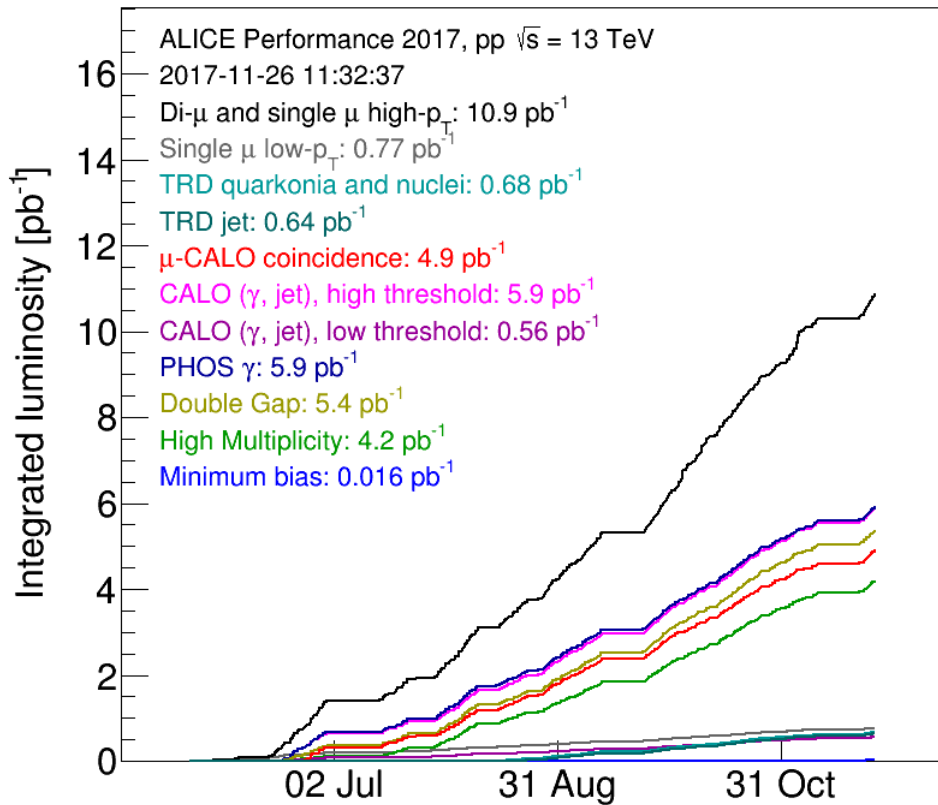


**Figure 2.8:** Integrated luminosity delivered to ALICE in 2017 for pp collisions at 13 TeV [Colb].

# Chapter 3

## Data Analysis

### 3.1 Data sample

The pp data used for this analysis were collected in 2017. Ideally, one would prefer to use the most recent data, however the data collected in 2018 were not ready in terms of reconstruction and data quality assurance. Furthermore, for data collected in 2016, e.g. LHC16o period, not all the triggers needed (e.g. CMSH) were available for the interest of this study. The data samples used in this analysis, taken from periods LHC17h and k, were taken under the same conditions, indicated in Table 2.2. Only runs that passed the ALICE Quality Assurance (QA) checks for physics analysis are selected. QA is a set of criteria/conditions used to define the quality of the data. The conditions satisfied are listed in Table 3.1. The standard event triggers for a heavy-flavour decay muon

Period	LHC17h and LHC17k
Run Type	Physics
Beam Mode	Stable
Trigger Detectors	At least Muon Trigger
Readout Detectors	At least Muon Tracking, Muon Trigger and SPD
Run Quality	Not bad for readout detectors
Run duration	$\geq 10$ min

**Table 3.1:** The Quality Assurance (QA) criteria used to define the quality of the data in this analysis [Col17a].

analysis includes a minimum bias trigger (MB), CINT7-B-NOPF-MUFAST, a single muon low- $p_T$  trigger, CMSL, and a single muon high- $p_T$  trigger, CMSH. In single muon analyses, particularly heavy-flavour studies, these two triggers are always considered in order to check whether it is necessary to combine CMSL and CMSH data samples to improve the statistic precisions in the different  $p_T$  regions of interest [Zha18] [Mar17]. The same procedure is followed

in this thesis. In Table 3.2 the number of runs in each period are given. The final runlists can be found in Appendix 5.3. The triggers, MB and CMSL,

Period	Number of runs
LHC17h	103
LHC17k	102

**Table 3.2:** Total number of analysed runs that passed the QA per data taking period.

were downscaled in both data taking periods (downscaling is the suppression of event rates for that particular trigger class). For LHC17h the triggers MB and CMSL were downscaled to 0.013% and 6.00%, respectively. Similarly, for LHC17k the triggers MB and CMSL were downscaled to 0.014% and 6.00%, respectively [Col17a].

## 3.2 The Analysis Strategy

The aim of this analysis is to extract  $p_T$ - and  $\eta$ -differential production cross sections of single muons produced from heavy-flavour hadron decays at forward rapidity in pp collisions at  $\sqrt{s} = 13$  TeV. The strategy for this analysis is shown in Figure 3.1. The standard event and track cuts are applied offline to ensure that a clean data sample is used for the analysis of single muons. Each event and track cut is described in detail in the following. Thereafter, corrections for acceptance and efficiency are described yielding generated and reconstructed measurements.

### 3.2.1 Event selection cuts

Predefined event selection cuts, namely Physics Selection and Good Vertex, implemented in this analysis are referred to in the excerpt of runGrid.C shown in Figure 3.2. The entire macro is shown in Appendix B. These event cuts were implemented as shown in line 39, as kSelectedTrig, kPhysicsSelected and kGoodVertex.

- **Selected Trigger** is the type of trigger selected: for minimum bias (MB) events, the MB trigger class, which requires a track in the V0 and the SPD (see description in Chapter 2 under Trigger Detectors), is selected. This ensures the measurement of all accepted events. The two single muon triggers, the high- $p_T$  trigger, CMSH, and the low- $p_T$  trigger, CMSL, are used to select single muons of interest in this study utilising hard track  $p_T$  thresholds of  $p_T > 4.2$  GeV/ $c$  and  $p_T > 0.5$  GeV/ $c$ , respectively.

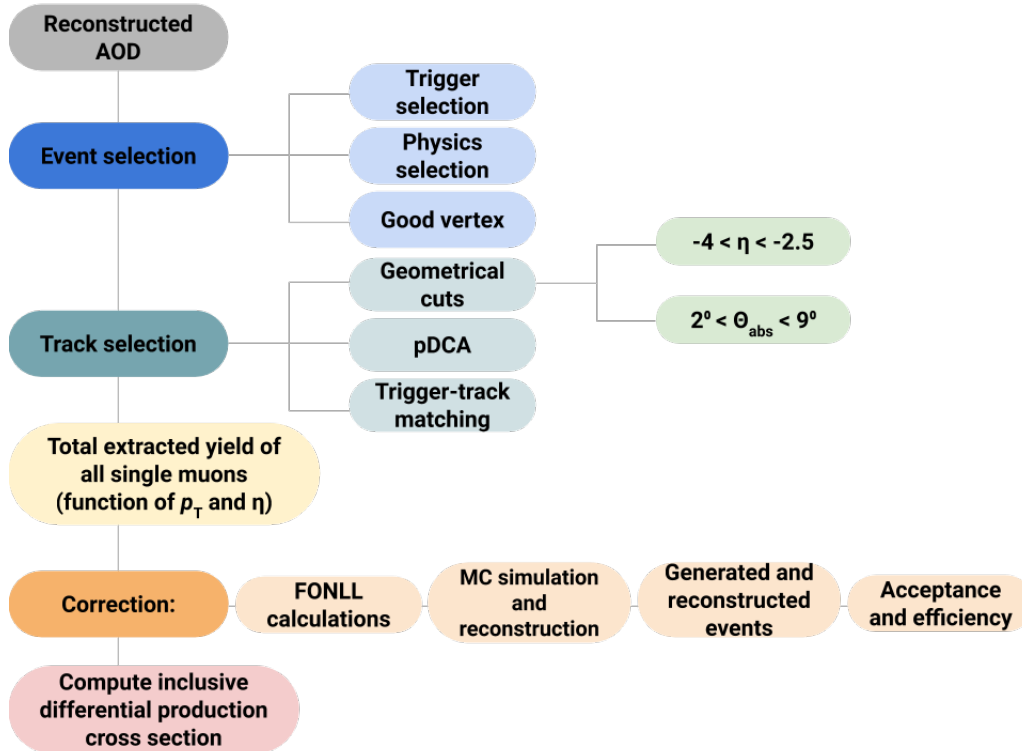


**Figure 3.1:** Analysis strategy followed.

```
32 gROOT->LoadMacro("AliAnalysisExamplePt.cxx++g");
33
34 AliAODInputHandler *aodH = new AliAODInputHandler();
35 mgr->SetInputEventHandler(aodH);
36
37 AliMuonEventCuts *muonEventCuts = new
38 AliMuonEventCuts("StandardMuonEventCuts","StandardMuonEventCuts");
39 muonEventCuts->SetFilterMask(AliMuonEventCuts::kPhysicsSelected |
40 AliMuonEventCuts::kSelectedTrig |AliMuonEventCuts::kGoodVertex);
41 muonEventCuts->SetTrigClassPatterns("CMSH7-B-NOPF-MUFAST", "OMSH:21");
```

**Figure 3.2:** runGrid.C, showing the implementation of event selection cuts.

- **Physics Selection** rejects pile-up background and poor quality events. Pileup is caused by beam-induced background that can occur from same bunch-crossing collisions and out-of-bunch collisions. Same bunch-crossing pileup is defined as two or more collisions occurring in the same bunch crossing. Out-of-bunch pileup is defined as one or more collisions occurring in bunch crossings different from the one which triggered the acquisition. Beam-induced background occurs as a result of beam particles interacting with either the residual gas in the beam pipe or the beam pipe itself. Applying a cut on V0 timing eliminates these background events. This is shown in Figure 3.3 [Kry14].

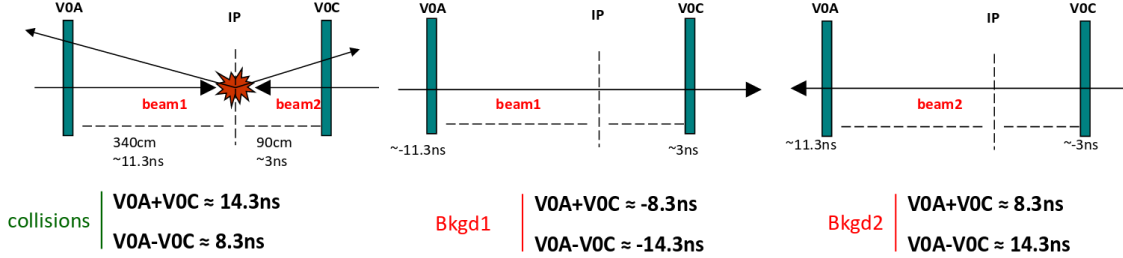


**Figure 3.3:** Schematic representation of V0 detectors' position and timing [Kry14] for the event selection

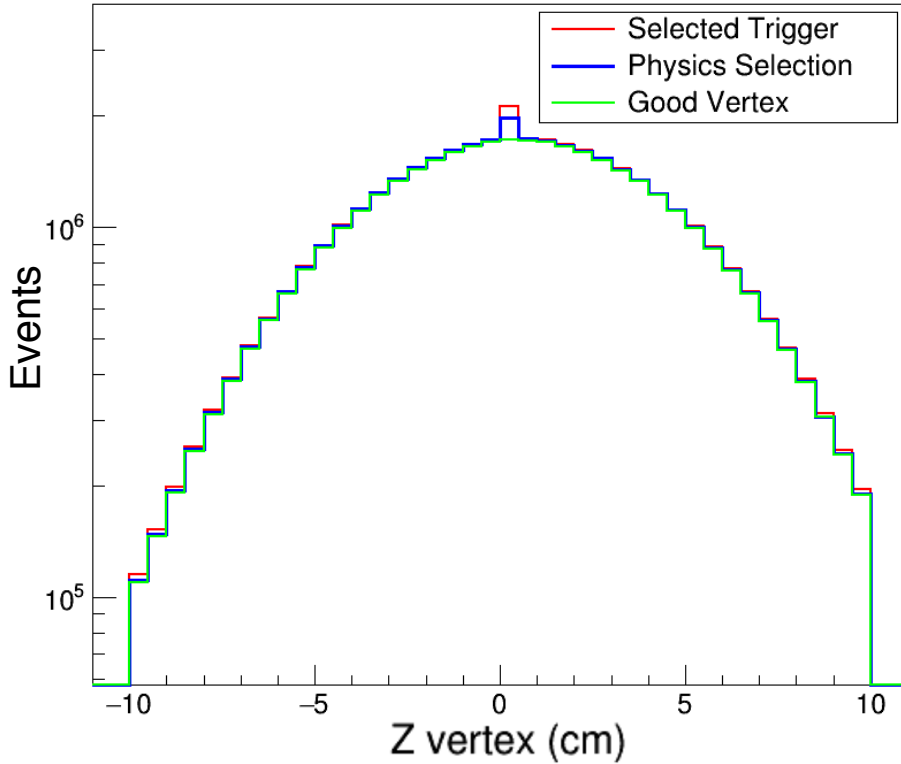
- **Good Vertex** selects events only coming from the primary vertex by reconstructing tracks with the ITS. These tracks provide an accurate measurement of the interaction vertex. The SPD is responsible for vertexing and is optimized in the region  $|z_v^{SPD}| < 10 \text{ cm}$ , as this is where the efficiency of the detector is well defined.

Table 3.3 indicates the number of events recorded per event cut, as described above, and is given according to the selected trigger per data taking period.

Event Cuts	LHC17k			LHC17h		
	CINT	CMSL	CMSH	CINT	CMSL	CMSH
Triggers:						
Event trigger	0.822M	62.0M	25.6M	0.732M	77.1M	22.3M
Physics Selection	0.762M	61.7M	25.4M	0.661M	75.6M	22.0M
Good Vertex	0.725M	61.2M	25.0M	0.656M	74.1M	20.7M

**Table 3.3:** Summary of the trigger-selected statistics after applying various event cuts: physics selection and good vertex.

In Figure 3.4 an example of the vertex distribution is shown for the data taking period LHC17k. This distribution shows the number of events within the optimised region of the SPD,  $-10 \text{ cm} < z_v < 10 \text{ cm}$ , where  $z_v$  is the vertex region in the z-direction, the z-direction being in the direction of the beam [Col10]. The vertex distribution peaks off-center. This is a result of the fact that the primary vertex does not always coincide with the nominal interaction point as well as aging effect. The outlier at  $\sim 1 \text{ cm}$  is seen in other analyses [Sar] and is removed by the Good Vertex event cut. The analysis task used (AliAnalysisTExamplePt.cxx) to implement the event cuts is shown in Appendix C where the code relevant to the analysis is given.



**Figure 3.4:** Vertex distributions depicting the distribution of events as a function of the vertex position for trigger CMSH and data taking period LHC17k after applying the various event cuts.

### 3.2.2 Track selection cuts

The muon analysis requires selecting tracks of muons of interest within the geometrical acceptance of the Muon Spectrometer. These selection criteria are referred to as track cuts. These cuts are described below,

- **Geometrical cuts** take into account the geometrical acceptance of the Muon Spectrometer. This is implemented in terms of the pseudorapidity ( $\eta$ ) and the exit polar angle with respect to the front absorber ( $\theta_{abs}$ ). Tracks are reconstructed in the pseudorapidity region  $-4 < \eta^\mu < -2.5$  to ensure that only tracks within the acceptance of the Muon Spectrometer are analysed. The corresponding track polar angle region is  $2^\circ < \theta_{abs} < 9^\circ$  where  $\theta_{abs}$  defines the acceptance of the Muon Spectrometer as well as the coverage of the absorber at the entrance to the Muon Spectrometer.
- The **correlation of momentum to distance-of-closest approach ( $p$ DCA)** is used to remove beam-gas interactions and particles produced in the front absorber. Beam-gas interactions occur when beam particles interact with the residual gas of the vacuum chamber leaving tracks in

the detectors. The DCA is defined as the distance between the interaction vertex and the extrapolated muon track in the plane containing the vertex and perpendicular to the beam direction. The DCA distribution of tracks coming from the interaction vertex are described by a Gaussian function whose width is inversely proportional to the momentum of the muon. Any beam-induced background will not follow this Gaussian function and can be removed by applying a cut on the product of the momentum of the muon and the DCA ( $p \times \text{DCA}$ ), at 6 times the standard deviation ( $6\sigma$ ) of the Gaussian distribution. In figure 3.5 one can see that this track cut removes the majority of tracks that are high- $p_T$  tracks.

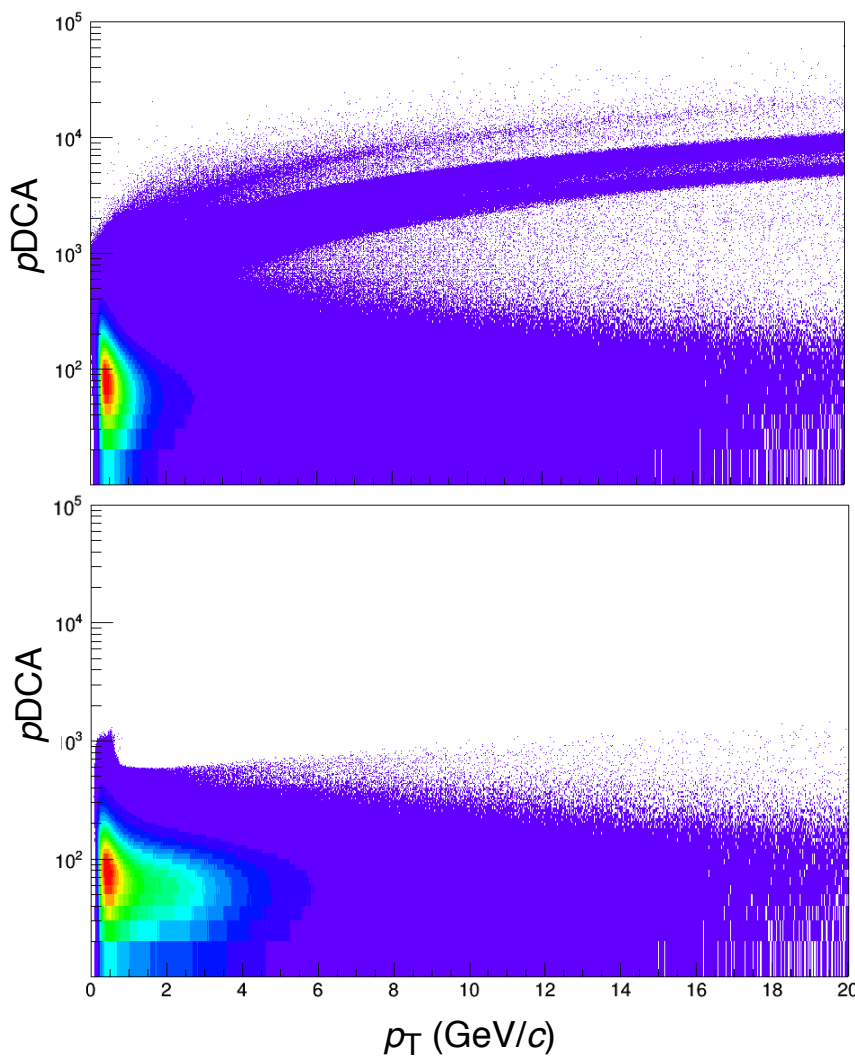


**Figure 3.5:**  $p\text{DCA}$  as a function of  $p_T$ , illustrating the effect of the  $p\text{DCA}$  track cut on LHC17k data with the CMSH trigger. See text for details.

- **Trigger-tracker matching conditions** reduce hadronic background that cross the iron wall separating the muon tracking and trigger chambers. The trigger-tracker matching cut removes fake or ghost tracks. These are tracks which are not associated to a single particle crossing the entire Muon Spectrometer. It requires that each reconstructed muon track in the muon tracking chambers match the corresponding track in the trigger chambers. The CMSL and CMSH triggers require that the muon tracks considered should meet the transverse momentum threshold of  $p_T > 0.5 \text{ GeV}/c$  and  $p_T > 4.2 \text{ GeV}/c$ , respectively. This track cut reduces the number events drastically, as seen in Table 3.4.

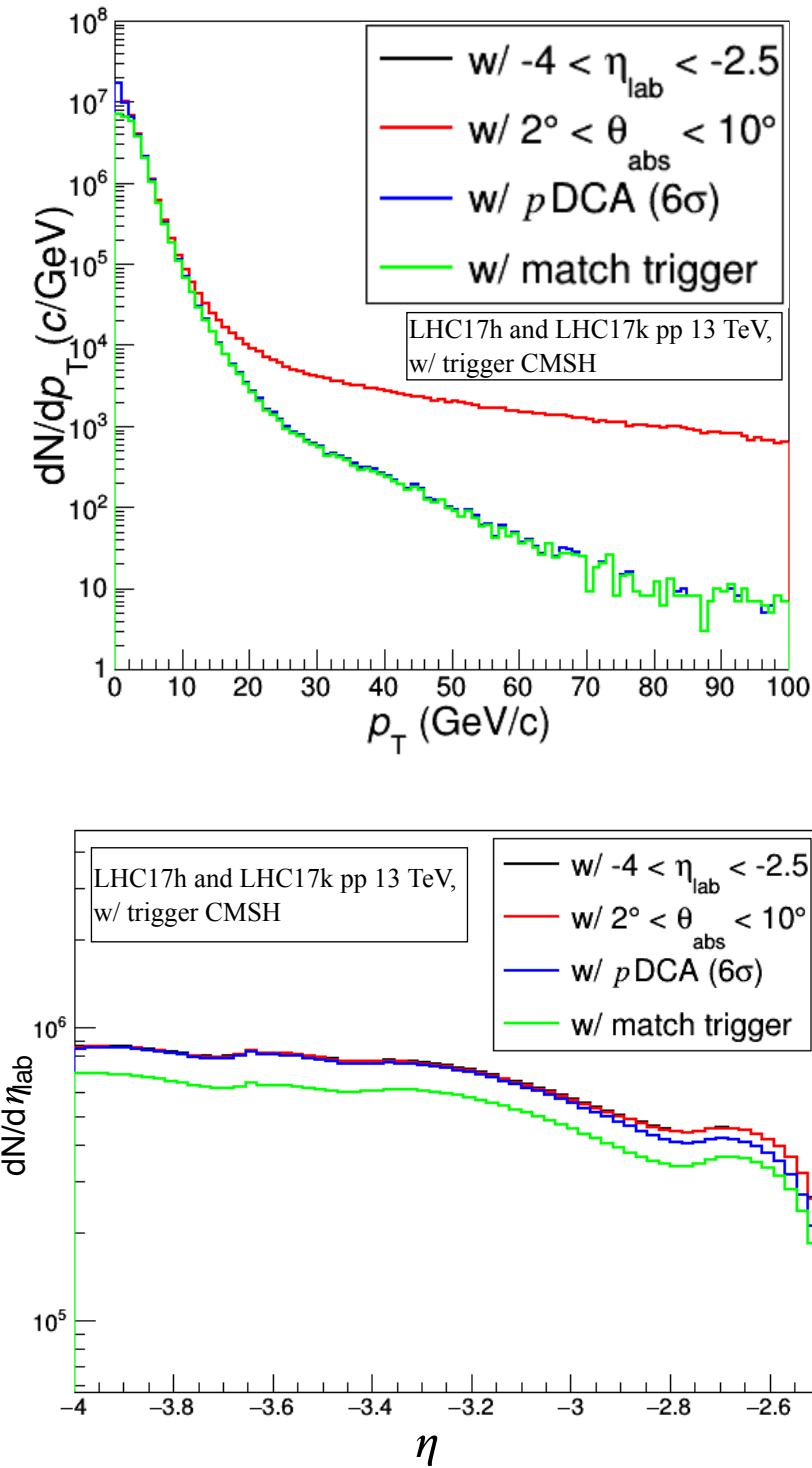
In Figure 3.5 an example of the  $p\text{DCA}$  is shown as a function of the transverse momentum ( $p_T$ ) where the top figure illustrates the events before the  $p\text{DCA}$  cut is implemented and the bottom figure illustrates the number of events after the  $p\text{DCA}$  track cut. It is clear that the removal of beam-gas interactions and particles produced in the front absorber affects the number of events, as shown visually by the removal of the top half of the plot, as well as in the statistics table, Table 3.4, where 23.2M events are reduced to 22.6M events.

Table 3.4 shows the trigger-selected statistics after applying various event and track cuts used in this analysis and the corresponding data taking periods.

Event Cuts	LHC17k		LHC17h	
Triggers:	CMSL	CMSH	CMSL	CMSH
$\eta$	55.8M	23.3M	69.7M	19.9M
$\theta_{abs}$	54.5M	23.2M	69.3M	19.8M
$p\text{DCA}$	54.8M	22.6M	68.4M	19.2M
Trigger-tracker matching	0.944M	14.9M	1.15M	12.8M

**Table 3.4:** The number of events recorded per track cut according to the triggers selected for each data taking period used in this analysis.

In Figure 3.6 the  $p_T$ - and  $\eta$ -distributions are shown in the top and bottom, respectively, from merged LHC17h and LHC17k data samples for the CMSH trigger, with event and track cuts implemented. These different distributions illustrate the track cuts described, namely a geometrical cut on the pseudorapidity,  $\eta$  (black), a geometrical cut on the polar angle region,  $\theta_{abs}$  (red), a cut on  $p\times\text{DCA} (6\sigma)$  (blue), and the trigger-tracker matching conditions (green). Both the  $p_T$ - and  $\eta$ - distributions are shown for particle identification purposes. Similarly, the  $p_T$ - and  $\eta$ -distributions from merged LHC17h and LHC17k data samples for the CMSL trigger, with event and track cuts implemented, are shown in Figure 3.7.



**Figure 3.6:** Extracted  $p_T$ - and  $\eta$ - distributions obtained from merged data samples collected during periods LHC17h and k using the CMSH trigger class. These distributions are extracted after implementing event and track cuts.

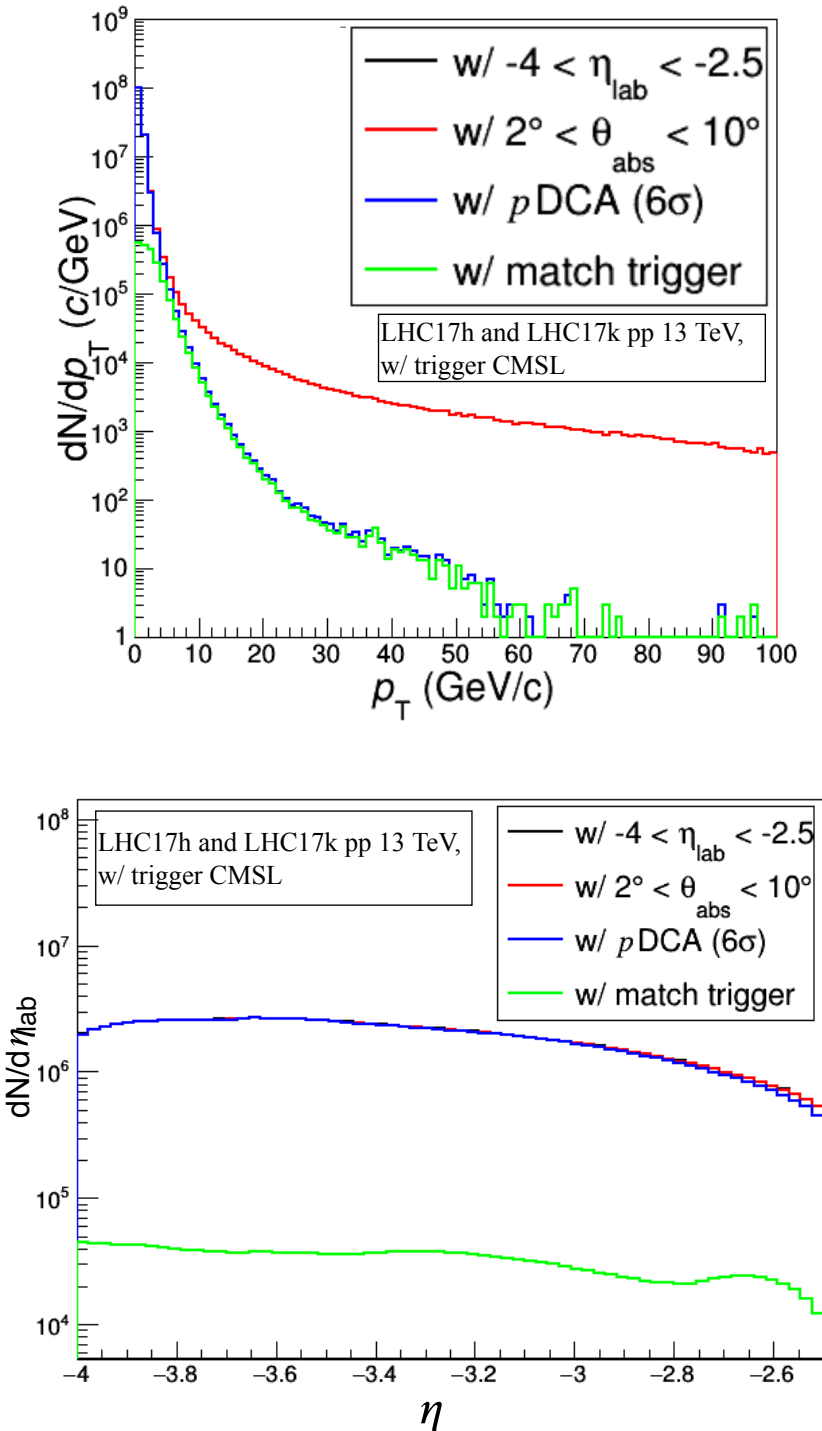


**Figure 3.7:** Extracted  $p_T$ - and  $\eta$ - distributions obtained from merged data samples collected during periods LHC17h and k using the CMSL trigger class. These distributions are extracted after implementing event and track cuts.

### 3.3 ALICE offline framework

The ALICE offline framework, AliROOT, used by the ALICE collaboration, is based on an object-oriented programming language, namely C++, and uses the framework developed by CERN called ROOT, as well as GEANT 3.21 for detector simulation codes. This framework is used for analysis, reconstruction and simulation which are utilised in the analysis and efficiency studies described in this chapter.

The AliROOT framework simulates primary hadronic collisions using Monte Carlo event generators such as PYTHIA [Ska06] and HIJING [gW94] as well as the response of the ALICE detector using transport packages such as GEANT4 [ea03] and FLUKA [FJ05]. The event generators store various properties of the simulated Monte Carlo "particle" such as its momentum and energy. The transport packages then transport each of the aforementioned particles into the detectors where deposited energies are measured and detected as *hits*. These *hits* store information on the particle's energy loss and the origin of the track, or its mother particle. Each *hit* is then turned into a *digit*, after which the detector response information specific to that *hit* is used to store the *hits* as raw data. Tracks stored as Event Summary Data (ESD) are reconstructed tracks that are either reconstructed from measured raw data or simulated raw data. The ESD contains any necessary information for the study such as the run number or primary vertex information. Figure 3.8 shows the framework followed, indicating the process from *digits*, Monte Carlo simulated tracks, and raw data, real data tracks, to ESD. The raw data then needs to be corrected for calibration and alignment by using the data stored in the Offline Condition Database (OCDB) for the corresponding run numbers used. The ESD tree OCDB stores AliEn (Alice Environment) files which are used as pointers to the physical calibration and alignment conditions of each run. These conditions are either stored on local storage space or the grid. Additional calibration and alignment reconstruction is done using the simulation macro, sim.C (see Appendix D), and reconstruction macro, rec.C (see Appendix E).

### 3.4 FONLL model calculations

The Fixed Order plus Next-to-Leading Logarithm (FONLL, [Nas98]) calculations are used in this study to compare with results obtained from experimental data. The FONLL is a theoretical model for calculating the single inclusive heavy-flavour hadron production cross sections. Therefore, FONLL calculations are accepted predictions for open heavy-flavour (e.g. charm and beauty) hadron production cross sections since they overcome the divergence at high  $p_T$  by the re-summation of the pQCD series in the high  $p_T$  region by matching pQCD NLO calculations with the calculations from fragmentation function formalism [Zha12]. In addition, FONLL calculations are used in the

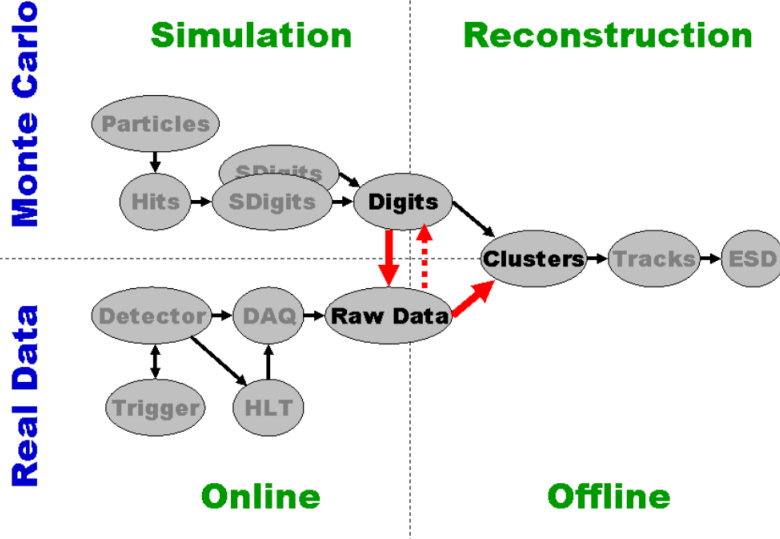


**Figure 3.8:** The ALICE Offline Framework for Raw Data [Col19a].

context of this analysis to evaluate the acceptance times efficiency ( $A \times \epsilon$ ) of the Muon Spectrometer.  $A \times \epsilon$  takes into account the alignment of the trigger and tracking chambers with respect to the rest of the ALICE detector due to possible variations in the positions of detector elements. FONLL simulates the production cross section of heavy-flavour hadrons and subsequent single-muon decays as a function of  $p_T$  and  $\eta$  in pp collisions at 13 TeV. This is done in order to obtain the shape of these  $p_T$ - and  $\eta$ -distributions by considering the CTEQ6.6 Parton Distribution Functions (PDFs) [ea08]. The following processes were considered in the FONLL simulation of heavy-flavour production cross sections in pp collisions at 13 TeV [Nas98];

$$p + p \rightarrow c + X \quad (3.1)$$

$$p + p \rightarrow b + X \quad (3.2)$$

followed by the subsequent decay processes into single muons;

$$c \rightarrow 70\% D^0 + 30\% D^+ \rightarrow \mu + X \quad (BR = 10.86\%) \quad (3.3)$$

$$b \rightarrow \mu + X \quad (BR = 10.33\%) \quad (3.4)$$

$$b \rightarrow D \rightarrow \mu + X \quad (BR = 9.66\%) \quad (3.5)$$

for which the branching ratios (BR) are also indicated. In Figure 3.9 the  $p_T$ -differential production cross sections from heavy-flavours are extracted using the FONLL simulations and plotted in the region  $2 < p_T < 20$  GeV/c and  $-6 < \eta < 6$ , since it is well known that charm- and beauty-decay dominate in this  $p_T$  region, whereas at lower  $p_T < 6$  GeV/c single muons from pions and kaons dominate, while at higher  $p_T > 12$  GeV/c the decay of the W and Z

bosons dominate [Col17b]. As denoted in the legend, the green data points describe the decay of a beauty hadron ( $\bar{b}u/\bar{b}d$ ) to a D hadron ( $c\bar{u}/c\bar{d}$ ) to a muon ( $\mu$ ), the blue data points describe the decay of a beauty hadron ( $\bar{b}u/\bar{b}d$ ) directly to a muon ( $\mu$ ), the red data points describe the decay of charm to the combination of  $D^0(c\bar{u})$  and  $D^+(c\bar{d})$  to a muon ( $\mu$ ), and the black data points describes the sum of all decay channels, denoted as HF for heavy flavour. In the distributions to follow, the error bars in the horizontal direction indicate the statistical error which is defined as the square root of the sum of the weight in each bin squared, shown in Equation 3.6,

$$\text{statistical error} = \sqrt{\left(\sum_{i=1}^N w_i^2\right)}, \quad (3.6)$$

where  $w_i$  is the weight in each bin,  $i$ . This is the statistical error defined by the ROOT package.

Figure 3.10 shows the  $p_T$  distributions of the sum of all decay channels and the fit function as blue and green histograms, respectively. The fit function describes the FONLL cross section calculation well in the range  $2 < p_T < 15$  GeV/ $c$ , as illustrated in the bottom panel by the ratio of the FONLL to the fit in the lower panel of the figure. The  $p_T$ -fit function is described by Equation 3.7,

$$p0(e^{x(p1 \times (1 - e^{xp2}) + p3)} \times \frac{1}{x^{p4}} \times (p5 + xp6 + x^2 p7)). \quad (3.7)$$

The parameters of the fit function in Equation 3.7 that best describe the sum of all decay channels are listed as,

- $p0 = 377.065$ ,
- $p1 = 1.11722$ ,
- $p2 = -0.127816$ ,
- $p3 = -1.6324$ ,
- $p4 = 2.09285$ ,
- $p5 = 28.614.9$ ,
- $p6 = -358.339$ ,
- $p7 = -174.430$ .

Similarly, in Figure 3.11, the  $\eta$ -differential cross sections are extracted using the FONLL simulation, calculated over the region  $2 < p_T < 20$  GeV/ $c$  and  $\eta$  region  $-6 < \eta < 6$ , where the green, blue, red and black histograms

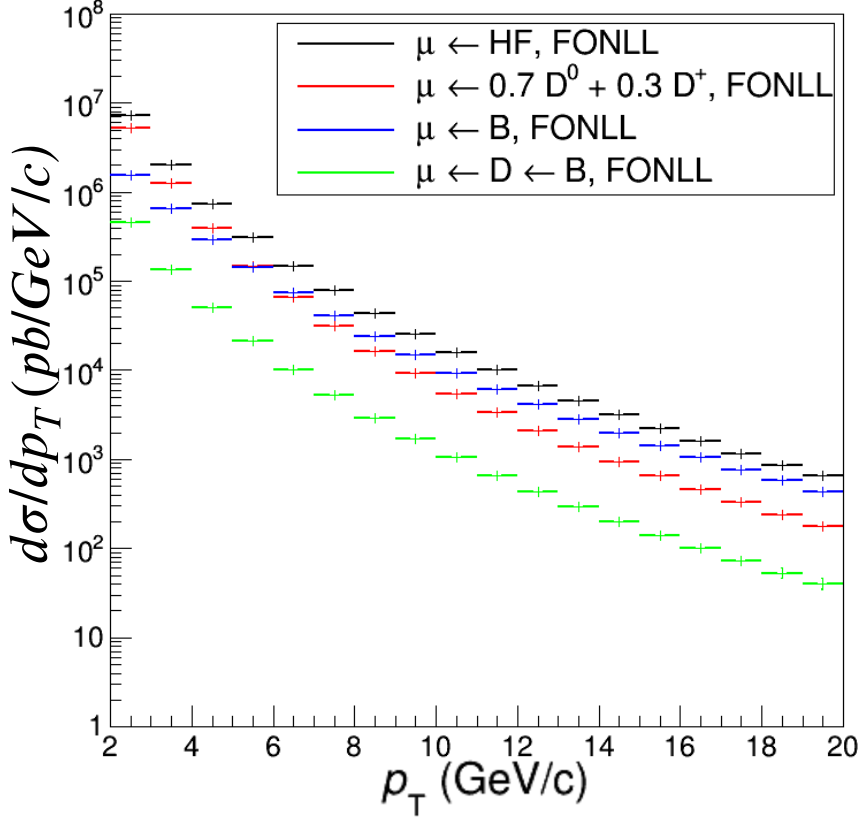


**Figure 3.9:** Differential production cross sections of heavy-flavour decay muons as a function of  $p_T$  for pp collisions at 13 TeV obtained from calculations by means of FONLL event generator [Nas98].

represent the same decay processes as in the  $p_T$ -differential cross sections. The  $\eta$ -differential cross sections are plotted over the region  $-6 < \eta < 6$  which is the full pseudorapidity range of the ALICE detector. This is consistent with previous studies [Mar17]. The  $\eta$ -differential cross section of the sum of the decay processes (black) was fitted with a function (red), as shown in Figure 3.12. The fit describes the distribution well, particularly over the region  $-4 < \eta < -2.5$ , as this is the geometrical acceptance of the muon spectrometer. In this case, the  $\eta$ -fit function can be described by Equation 3.8,

$$p0 + xp1 + x^2p2 + x^4p3 + x^6p4 + x^8p5. \quad (3.8)$$

The parameters of the fit function in Equation 3.8 that best describe the sum of all decay channels are listed as,

- $p0 = 8.916e+07$ ,
- $p1 = 4.095e+06$ ,

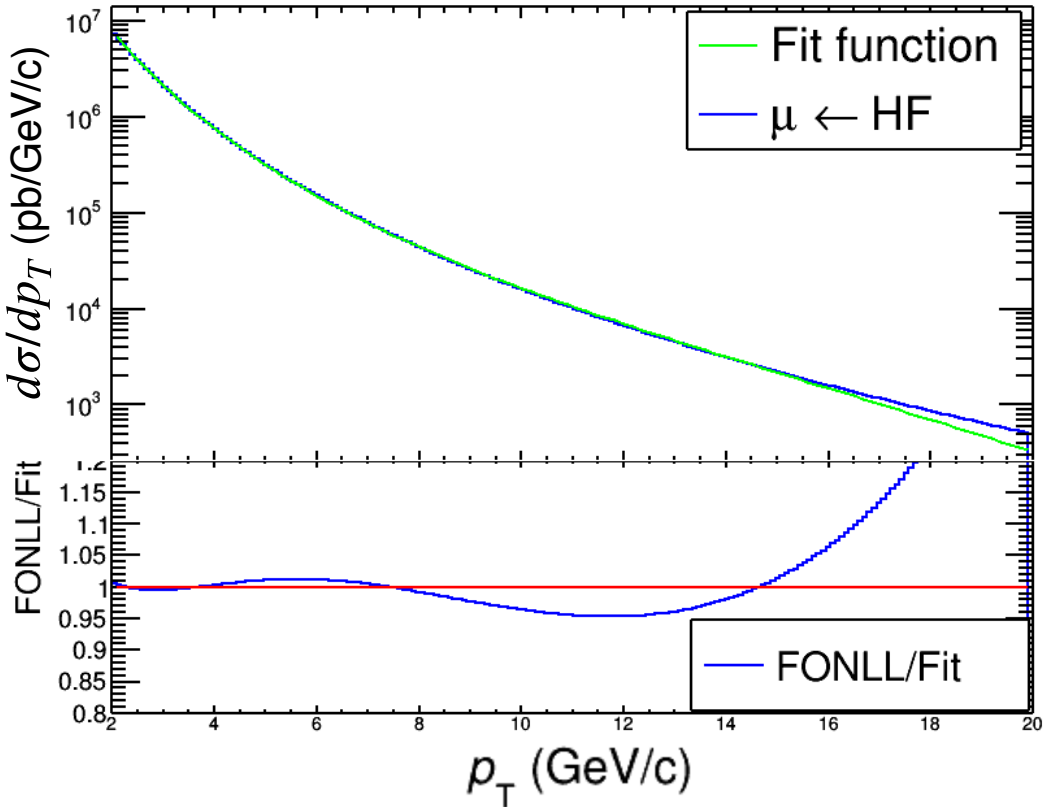


**Figure 3.10:** (Top) Differential production cross section of heavy-flavour decay muons as a function of  $p_T$  in pp collisions at 13 TeV obtained from calculations using the FONLL event generator [Nas98] compared to the fit function given in Equation 3.7, including statistical errors as horizontal bars. (Bottom) The ratio of the FONLL results to the fit function.

- $p2 = -1.291e+06$ ,
- $p3 = -1.687e+04$ ,
- $p4 = 635.1$ ,
- $p5 = -4.592$ .

The ratio of the FONLL results to the fit function are shown in the lower panel. The ratio is close to unity, between 0.99 and 1.01, thus the fit parameters are acceptable.

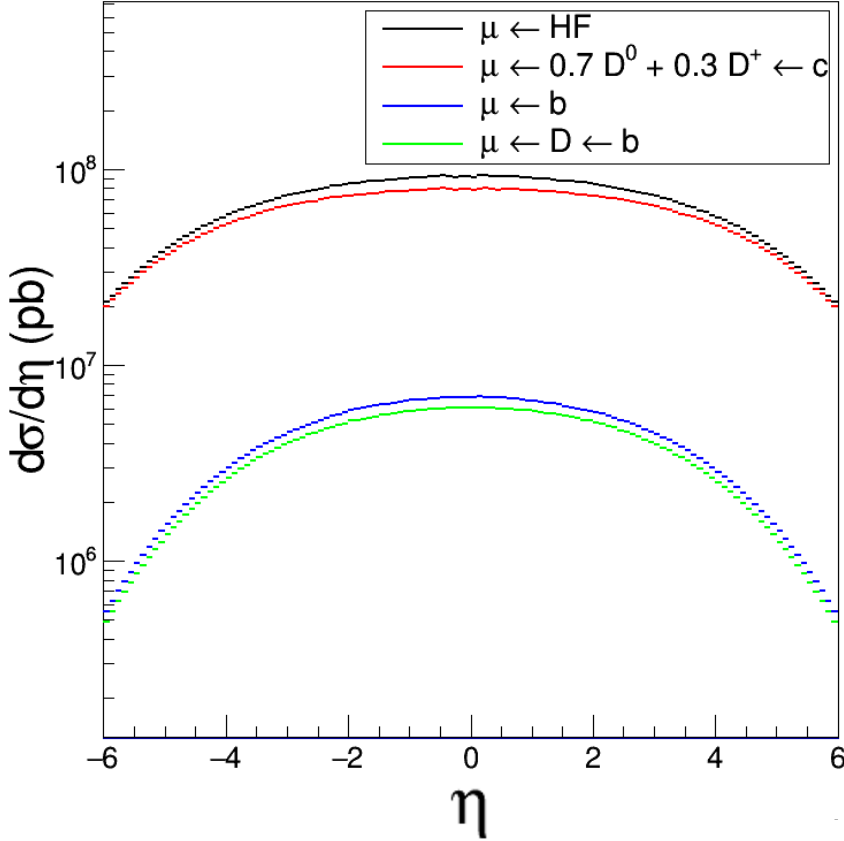


**Figure 3.11:** Differential production cross sections from heavy-flavour production as a function of  $\eta$  for pp collisions at 13 TeV obtained from FONLL event generator calculations [Nas98].

The parameters of the fit functions described in Equations 3.7 and 3.8 are then used as input in a Monte Carlo (MC) generator to simulate and reproduce the  $p_T$ - and  $\eta$ -distributions for a 100% efficient Muon Spectrometer by using a sim.C macro shown in Appendix D, within the AliRoot framework. These distributions are later referred to as "generated" spectra.

AliRoot is also used to reconstruct the raw physics data, accomplished by considering in the simulation the real detector performance (e.g. calibration) and alignment during each data taking period. This real event information is then used to reconstruct the data. These will be referred to as "reconstructed" spectra. The reconstruction of each run is performed using the rec.C macro given in Appendix E. The reconstructed and generated events are then used to obtain the acceptance and efficiency (discussed in the following section) which is then used to correct the total yield of all single muons shown in Figures 3.6 and 3.7. The acceptance and efficiency is determined according

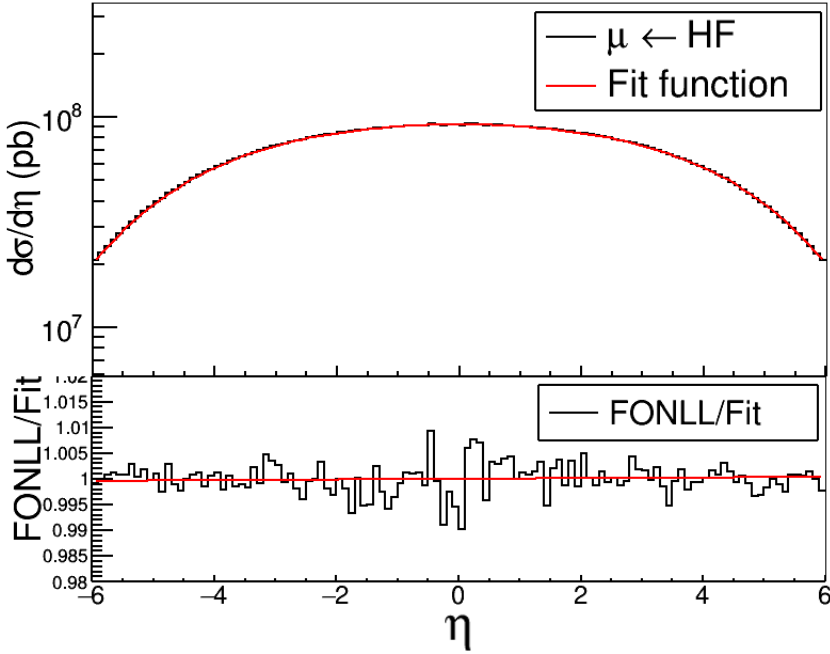


**Figure 3.12:** (Top) Differential production cross section of heavy-flavour muons as a function of  $\eta$  for pp collisions at 13 TeV obtained from calculations using the FONLL event generator [Nas98] and fitted with the function described in Equation 3.8. (Bottom) The ratio of the FONLL results to the fit function.

to Equation 3.9 [Mar17].

$$A \times \epsilon = \frac{\text{reconstructed}}{\text{generated}} \quad (3.9)$$

In Figure 3.13 both the reconstructed and generated  $\eta$ - and  $p_T$ -distributions are illustrated in the top and bottom panels, respectively, for the muon trigger, CMSH. The errors shown are statistical errors given by Equation 3.6. In the top and bottom figures of Figure 3.13, the reconstructed and generated events are shown in red and blue, as a function of  $\eta$  and  $p_T$ , respectively. The ratio of the reconstructed and generated events is then used to determine the acceptance and efficiency correction factor for the associated high- $p_T$  muon trigger, as described in the following section.

The same process is followed for the muon trigger, CMSL. In the top and bottoms panels of Figure 3.14 both the reconstructed and generated  $\eta$ - and  $p_T$ - distributions are illustrated, respectively. The ratio of the reconstructed and generated distributions is once again used to determine the acceptance and efficiency correction factor associated with the low- $p_T$  muon trigger.

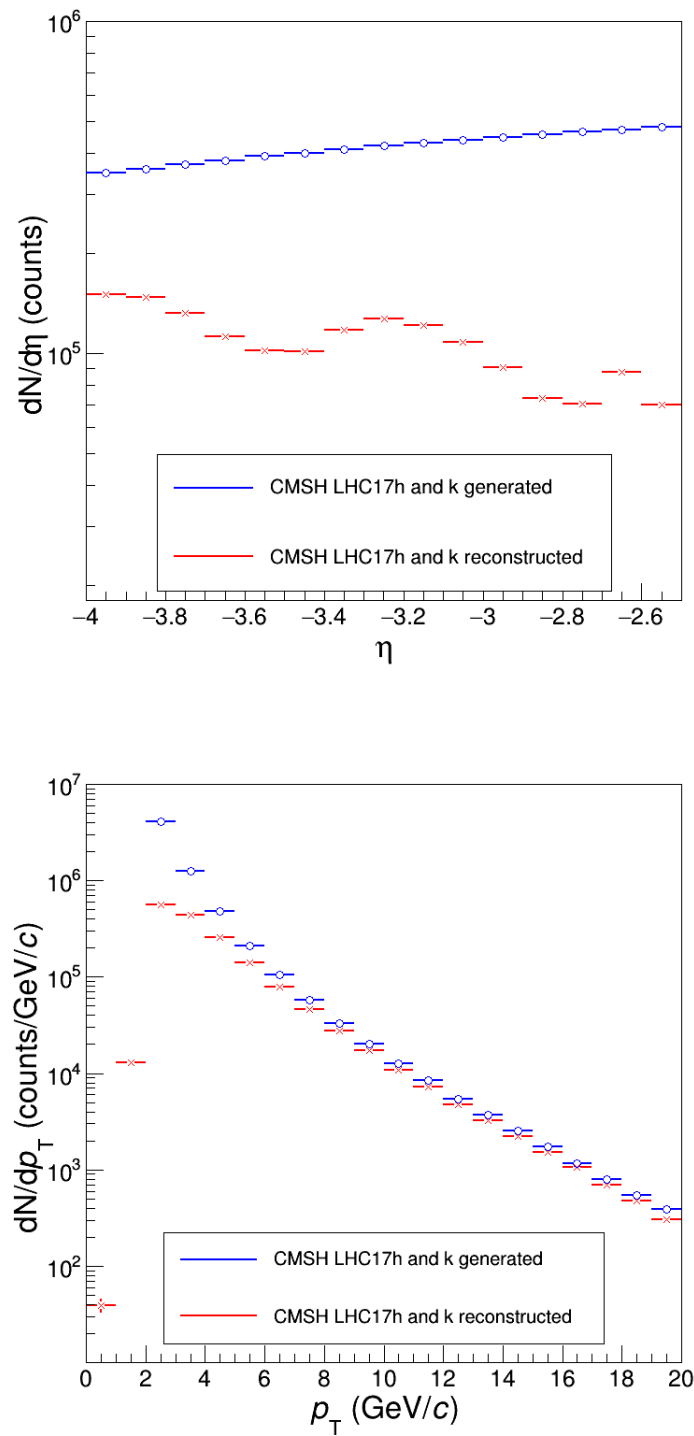


**Figure 3.13:** Reconstructed and generated  $\eta$ - and  $p_T$ -distributions for the geometrical acceptance of the Muon Spectrometer,  $-4 < \eta < -2.5$ , with the high- $p_T$  muon trigger, CMSH.

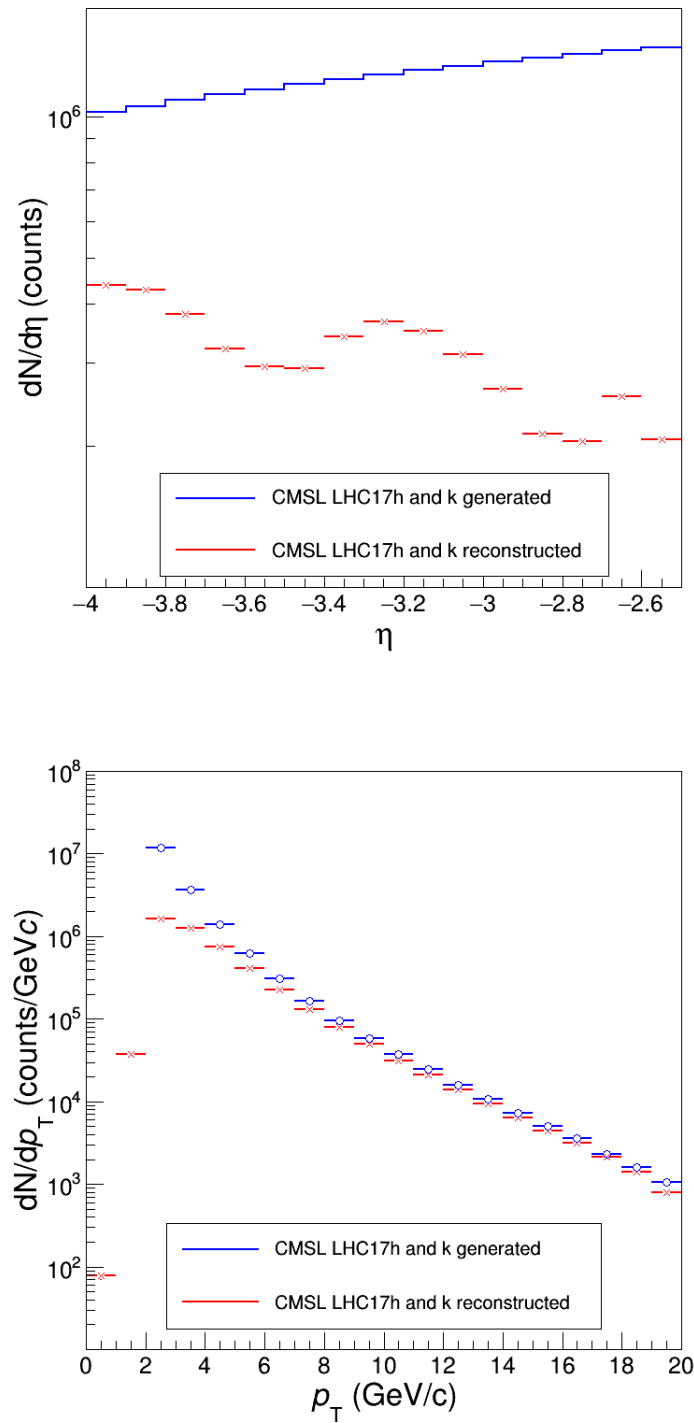


**Figure 3.14:** Reconstructed and generated  $\eta$ - and  $p_T$ -distributions for the geometrical acceptance of the Muon Spectrometer,  $-4 < \eta < -2.5$ , with the low- $p_T$  muon trigger, CMSL.

### 3.5 Acceptance and efficiency correction

The resulting acceptance and efficiency ( $A \times \epsilon$ ) is calculated according to Equation 3.9, i.e. dividing the number of reconstructed events by the number of generated events obtained in Figure 3.13. The correction factor is used to correct the  $p_T$  and  $\eta$  distributions shown in Figure 3.6 and Figure 3.7. The only errors associated with the results presented are statistical errors as described by Equation 3.6. The reason for the correction is to take into account specific configurations of every detector element of the Muon Spectrometer. The  $A \times \epsilon$  accounts for detector elements that have been excluded because of issues such as high voltage trips, etc. during each data taking period. As a result, the  $A \times \epsilon$  for each data taking period is analysed separately. The results of both data taking periods, are combined and subsequently corrected for the  $A \times \epsilon$  to produce the total extracted yield of all single muons for each muon trigger.

The top and bottom panels of Figure 3.15 show the  $A \times \epsilon$  as a function of  $p_T$  for the combined data taking periods, LHC17h and LHC17k, in the range  $2 < p_T < 20 \text{ GeV}/c$  for the high- and low- $p_T$  muon triggers, CMSH and CMSL, respectively. The red dotted line indicates an acceptance and efficiency of unity. The values of  $A \times \epsilon$  were also obtained as a function of  $\eta$  in the range  $-4 < \eta < -2.5$ , as shown in the top and bottom panels of Figure 3.16 for the high- and low- $p_T$  muon triggers, CMSH and CMSL, respectively. Values of  $A \times \epsilon$  are subsequently used to correct the total extracted yield of all single muons bin by bin. For both triggers, as a function of  $p_T$ , the acceptance and efficiency is low, between 0.15 and 0.7, at  $p_T < 6 \text{ GeV}/c$ , as shown in Figure 3.15. For the high- $p_T$  muon trigger, CMSH, both the total extracted yield and the corrected yield are shown in the top and bottom of Figure 3.17 as a function of  $p_T$  and  $\eta$ , respectively. The errors shown are statistical errors given by Equation 3.6. The same is done for the yields extracted for the low- $p_T$  muon trigger. The total extracted yields of all single muons with the low- $p_T$  muon trigger, CMSL, are corrected for  $A \times \epsilon$  bin by bin. Both the total extracted yield and the corrected yield are shown in the top and bottom panel of Figure 3.18 as a function of  $p_T$  and  $\eta$ , respectively. In order to express these corrected yields of single muons, they must first be normalised with respect to the MB in order to compute the differential production cross section, i.e. the number of muon triggered events ( $N_{CMSL(H)}$ ) is normalised to the number of minimum bias events ( $N_{CINT}$ ). The procedure is presented in the next chapter.

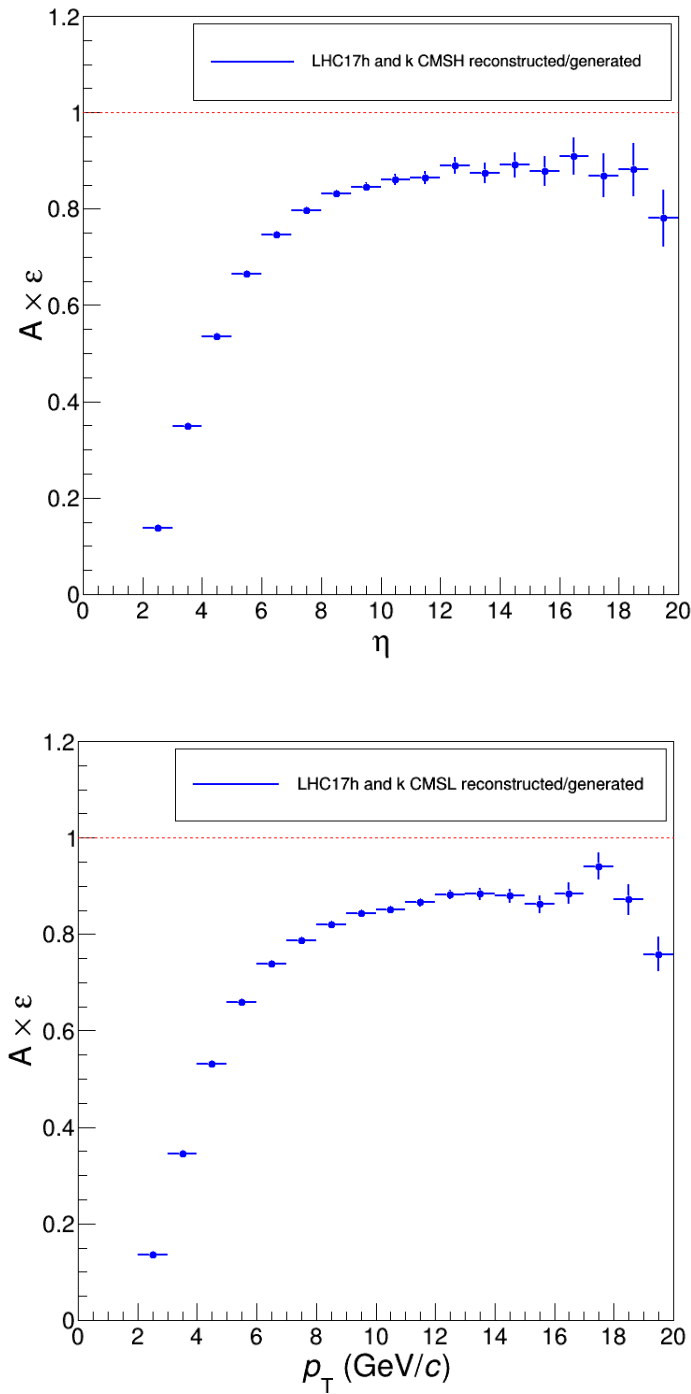


**Figure 3.15:**  $A \times \epsilon$  as a function of  $p_T$  for the high- and low- $p_T$  muon triggers, CMSH(L), in the range  $2 < p_T < 20$  GeV/c.

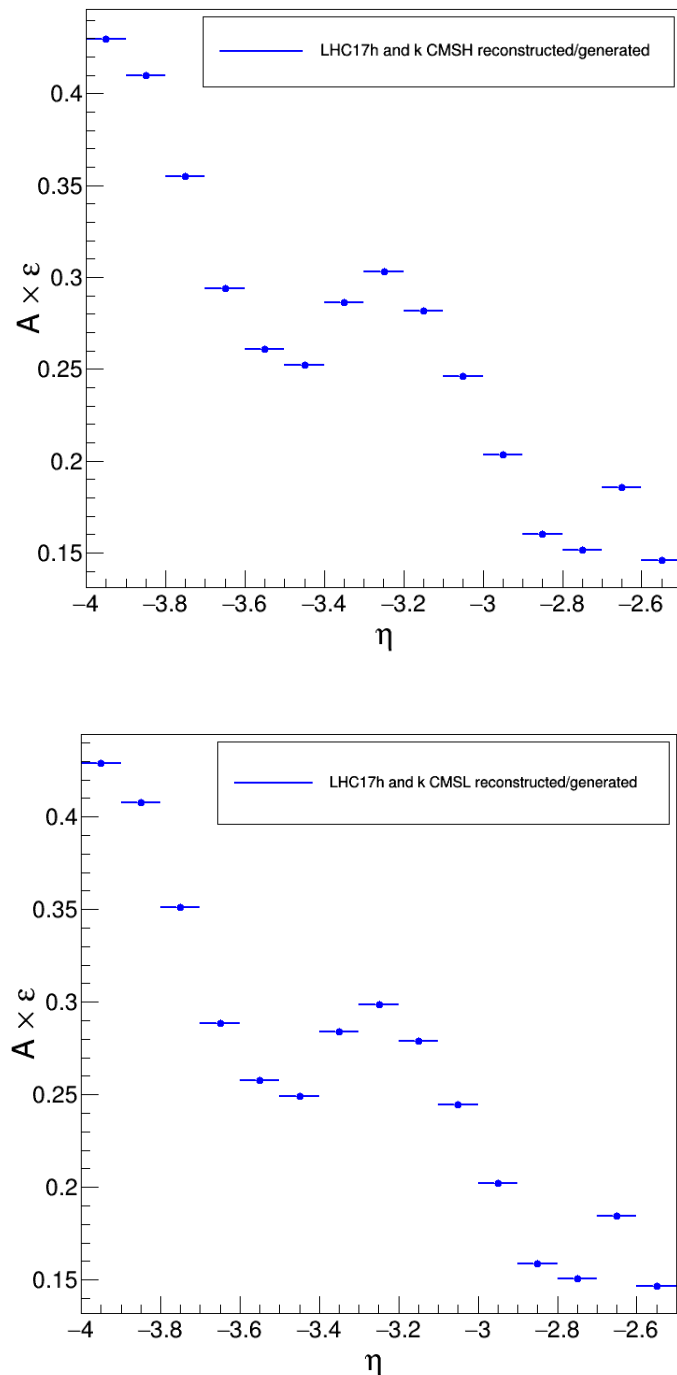


**Figure 3.16:**  $A \times \epsilon$  as a function of  $\eta$  for the high- and low- $p_T$  muon triggers, CMSH(L)7-B-NOPF-MUFAST, in the range  $-4 < \eta < -2.5$ .

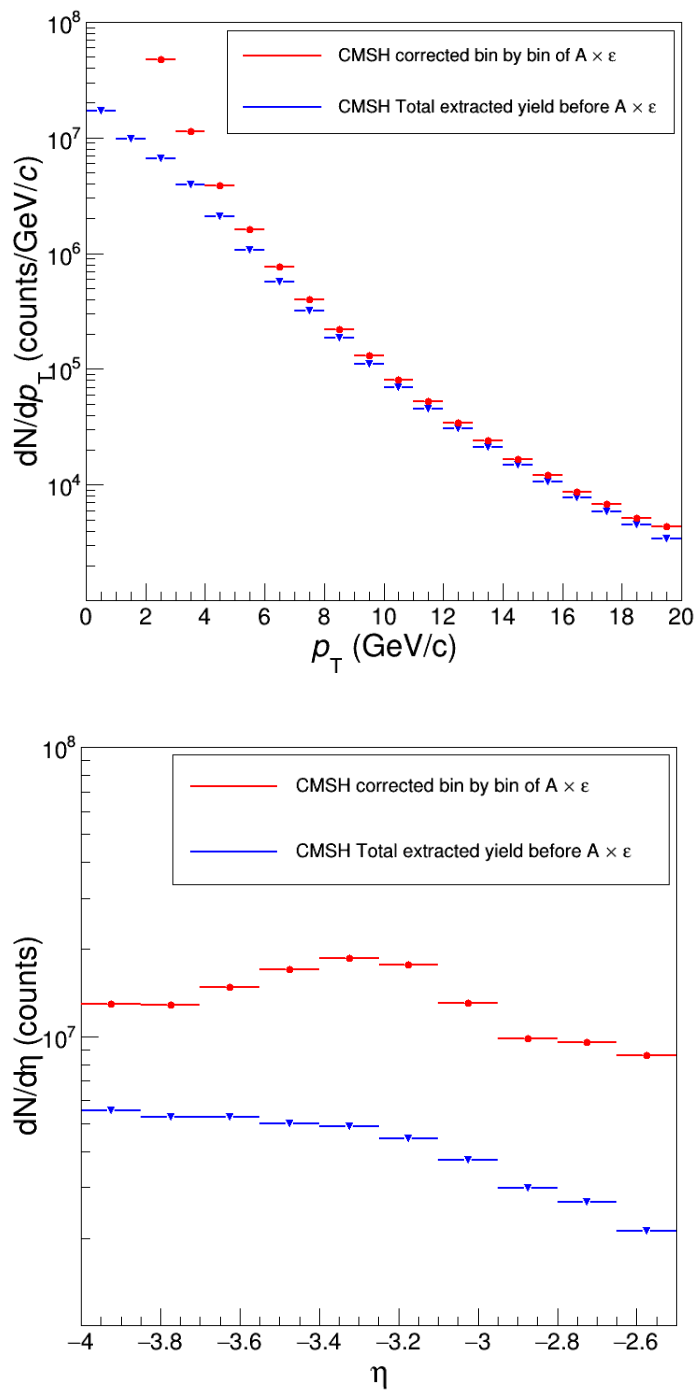


**Figure 3.17:** Total extracted yield of all single muons (blue) and corrected bin by bin for  $A \times \epsilon$  (red) as a function of  $p_T$  and  $\eta$  in the range  $2 < p_T < 20$  GeV/c and  $-4 < \eta < -2.5$ , respectively, for the muon trigger CMSH.

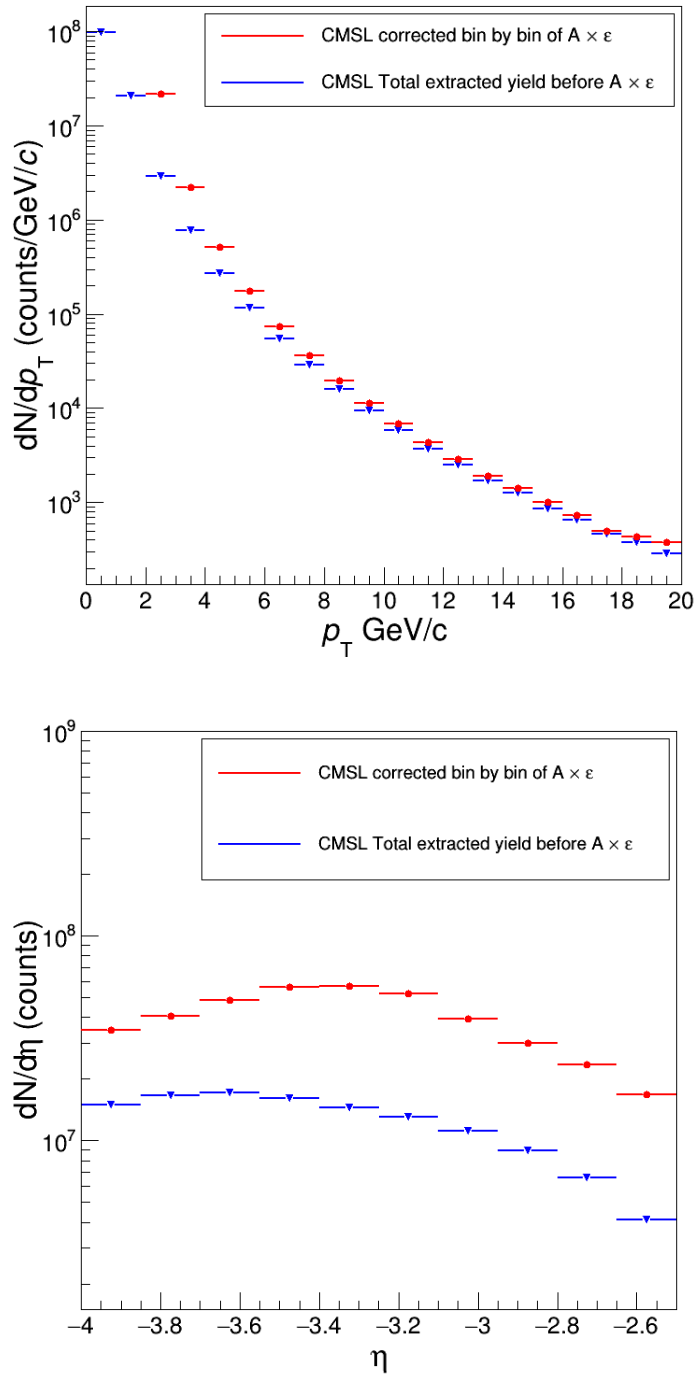


**Figure 3.18:** Total extracted yield of all single muons (blue) and corrected bin by bin for  $A \times \epsilon$  (red) as a function of  $p_T$  and  $\eta$  in the ranges  $2 < p_T < 20$  GeV/c and  $-4 < \eta < -2.5$  for the low muon trigger CMSL.

# Chapter 4

## Results and Discussion

The aim of this thesis is to extract the inclusive differential production cross section of muons from heavy-flavour decays obtained as a function of transverse momentum and pseudorapidity.

### 4.1 Differential production cross section measurements

The acceptance and efficiency corrected yields, discussed in the previous chapter, are used in order to obtain the differential production cross section via Equation 4.1, where they are represented as  $\frac{dN_{tot}^{\mu^\pm \leftarrow HF}}{dp_T(dy)}$  and  $A \times \epsilon$ , respectively. The normalisation factor,  $F_{norm}$ , the number of CMSL(H) events ( $N_{CMSL(H)}$ ) and the minimum bias cross section,  $\sigma_{MB}$ , will be discussed in the following subsections. The term  $\frac{dN^{\mu \leftarrow BKG}}{dp_T(dy)}$  and systematic uncertainties are outside of the scope of this thesis, however, their relevance will be discussed further in the following.

$$\frac{d\sigma_{\mu^\pm \leftarrow HF}}{dp_T(dy)} = \frac{dN_{tot}^{\mu^\pm \leftarrow HF}/dp_T(dy) - dN^{\mu \leftarrow BKG}/dp_T(dy)}{A \times \epsilon \cdot F_{norm} \cdot N_{CMSL(H)}} \cdot \sigma_{MB} \quad (4.1)$$

#### 4.1.1 Normalisation factor ( $F_{norm}$ )

The data sample analysed represents a fraction of MB events. In order to obtain the MB equivalent number of muon triggered events, a suitable normalisation factor ( $F_{norm}$ ) is required. The normalisation factor is the number of muon triggered events ( $N_{CMSL(H)}$ ) normalised to the number of minimum bias events ( $N_{CINT}$ ), as shown in Equation 4.2.

$$F_{norm} = \frac{N_{CMSL(H)}}{N_{CINT}}, \quad (4.2)$$

The normalisation factor,  $F_{norm}$  is defined by Equation 4.3;

$$F_{norm,(CMSL(H))} = \frac{L0b_{CINT} \cdot F_{CINT}^{purity} \cdot F_{CINT}^{pile-up}}{L0b_{CMSL(H)} \cdot F_{CMSL(H)}^{purity}} \quad (4.3)$$

where,

- $L0b_{CINT}$  is the scaler (trigger rate) values recorded at  $L0b$  level for CINT;
- $L0b_{CMSL(H)}$  is the scaler (trigger rate) values recorded at  $L0b$  level for CMSL(H);
- $F_{CINT}^{purity}$  is the purity factor for CINT, defined as the ratio of events, after the offline event selection, to the total number of events;
- $F_{CINT}^{pile-up}$  is the pile-up correction factor, defined as the purity factor associated to the MB trigger computed as the ratio of physics selected events to the total number of events;
- $F_{CMSL(H)}^{purity}$  is the purity factor for CMSL(H), defined as the fraction of accepted CMSL(H) triggered events that pass the offline event selection.

The  $L0b$  values for each trigger are obtained per run number of the selected data taking periods, as is the purity factor, which is defined as the number of physics selected events divided by all events.

The  $L0b$  factors are calculated using the script trigger.C (see Appendix F). This script produces an output with the L0b values and number of interacting bunches per run number. The purity factors are calculated using the script ReadPurity.C (see Appendix G). This script produces an output containing the ratio of physics selected events to all events. The pile-up correction fraction is obtained using the output of trigger.C and ReadPurity.C as input in the script muCalc.C (see Appendix H). This is a result of the definition of the pile-up fraction, described in Equation 4.4 as

$$F_{CINT}^{pile-up} = \frac{\mu}{1 - e^{-\mu}}, \quad (4.4)$$

given that

$$\mu = -\log(1 - \frac{F_{CINT}^{purity} \times L0b_{CINT}}{n_b \times f_{LHC}}), \quad (4.5)$$

where  $L0b_{CINT}$  is the scaler rate for the trigger CINT and  $n_b$  is the number of interacting bunches, both obtained using trigger.C, the purity factor is obtained using ReadPurity.C, and  $f_{LHC}$  is the revolution frequency of the LHC, where the value used is 11245 Hz [CERa].

The  $L0b$  values, number of interacting bunches, the purity factors and the pile-up fraction are all used as input for the script NormFinal.C found in

Appendix I which outputs the final normalisation factor for the trigger and data taking period specified.

The normalisation factors for each data taking period, per muon trigger, are given in Table 4.1. These values are substituted into Equation 4.1 for the associated data taking period and muon trigger.

	CMSH	CMSL
LHC17h	2160.64	59.5236
LHC17k	2088.82	58.3949

**Table 4.1:** Normalisation factors obtained for each data taking period, per muon trigger in this study.

### 4.1.2 Minimum Bias cross section $\sigma_{MB}$

The Minimum Bias cross section,  $\sigma_{MB}$ , is obtained from van der Meer scans at the LHC. Van der Meer (vdM) scans measure the cross section visible to given sub-detectors, the VZER0 (V0) and TZERO (T0) detectors. The rates measured in these sub-detectors are used to measure the cross section as the beams collide at different separations of the centres [Col18]. In van der Meer scans, the two proton beams are moved across each other in the transverse directions. The x and y scans are performed separately. The rate of the reference process as a function of the beam separation is used to determine the luminosity for head-on collisions of a pair of bunches. The cross section is proportional to the head-on rate and inversely proportional to the luminosity.

The two reference processes are based on the V0 detector and the T0 detector. The V0-based trigger condition requires at least one hit in each detector, V0-A and V0-C. Similarly, the T0-based trigger condition requires at least one hit in each detector, T0-A and T0-C, as well as an additional condition that the longitudinal coordinate of the interaction vertex lies in the range  $|z| < 30\text{cm}$ , where the interaction point at  $z=0$  is the nominal position [Col16a].

The corresponding cross section measurements for each process obtained in [Col19b] are,

$$\begin{aligned}\sigma_{V0AND} &= 57.8 \text{ mb} \\ \sigma_{TZERO} &= 30.1 \text{ mb},\end{aligned}$$

with a conservative uncertainty of 5%. The values given are the minimum bias cross sections for proton-proton collisions at  $\sqrt{s} = 13 \text{ TeV}$  obtained in 2015 because the finalised MB cross sections for the data sample of 2017 are not available yet [Col19b].

### 4.1.3 Background

A single muon background study is outside the scope of this thesis. For interest, potential sources of single muon background contributing to the total single muon  $p_T$ -differential yield in the region of interest, particularly the low- $p_T$  region, are shown in Figure 4.1 and discussed in details in [Zha18].

A comprehensive background study will allow one to estimate and remove the contributions of these decay processes shown in Figure 4.1 from the differential production cross section of muons.

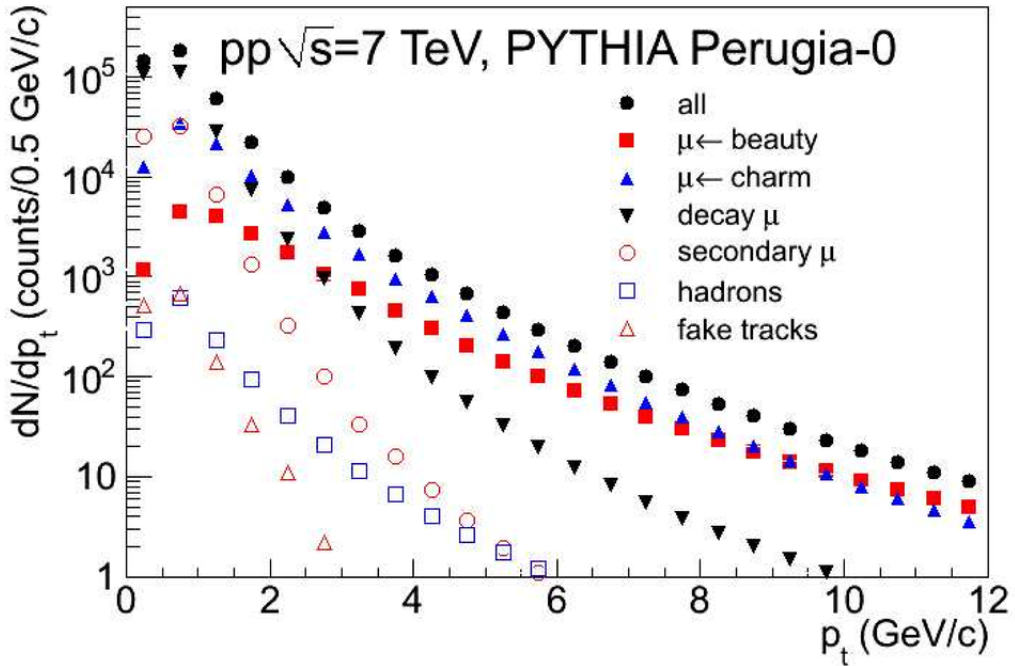


**Figure 4.1:** Typical single muon background contribution in the  $p_T$  distributions in the Muon Spectrometer studied in [Col14b].

### 4.1.4 Systematic Uncertainties

Systematic uncertainties are the uncertainties associated with the detector conditions. These uncertainties arise from various stages of the measurement such as the calibration of the detectors, the probability of detection of a given type of interaction, that is the acceptance, and model parameters that are not well defined [Rei03]. The systematic uncertainties associated with this study include the muon tracking efficiency arising from the efficiency in data and Monte Carlo. The systematic uncertainty associated with the single muon trigger efficiency arises from the intrinsic efficiency of the trigger chambers and the response of the trigger algorithm [Col17b]. An additional contribution arises from the  $\chi^2$  cut which is implemented for trigger-tracker matching. A

final contribution arises from the resolution and alignment of the tracking chambers [Col17b]. The results presented in this study do not include these systematic uncertainties as it is outside the scope of this thesis.

## 4.2 Discussion of results

### 4.2.1 Measured differential cross sections

The measured inclusive differential cross section of single muons is determined according to Equation 4.1, however, without the inclusion of background subtraction ( $dN^{\mu^\pm \leftarrow BKG}/dp_T(y)$ ) and systematic uncertainties. As mentioned in Section 3.1, two triggers are considered in heavy-flavour studies to gain on statistics in different  $p_T$  regions of interest [Col17b] [Mar17].

The results obtained from CMSL and CMSH are shown in Figures 4.2 and 4.3 where the differential cross sections are presented as a function of  $p_T$  and  $\eta$  in the range  $2 < p_T < 20$  GeV/c and  $-4 < \eta < -2.5$ , respectively. The only errors associated with the results presented are statistical errors as described by Equation 3.6. The bottom panels of the figures show the ratio of the high- $p_T$  trigger to the low- $p_T$  trigger. Figure 4.2 shows both triggers as a function of  $p_T$  with the ratio of the high- $p_T$  trigger to the low- $p_T$  trigger below. It is observed that the inclusive  $p_T$ -differential production cross section results exhibit a decreasing exponential shape. That is, the inclusive  $p_T$ -differential production cross section of single muons decreases with increasing  $p_T$ , i.e. the magnitude of the cross section is of the order  $10^7$  pb/GeV/c at  $p_T = 2$  GeV/c and decreases to  $10^3$  pb/GeV/c at  $p_T = 12$  GeV/c. This shape is observed for both triggers and reflects the same trend as those presented in [Zha18] and [Mar17] for the measurements in pp collisions at  $\sqrt{s} = 5.02$  TeV and 8 TeV over the  $p_T$  region of interest for the heavy-flavour muon study, that being  $2 < p_T < 12$  GeV/c. Figure 4.1 indicates that the region of interest for heavy-flavour muon studies is between  $2 < p_T < 12$  GeV/c.

From the ratio of the two triggers it can be deduced that the high- $p_T$  trigger yields a slightly higher cross section than the low- $p_T$  trigger by  $\sim 10\%$ . This is consistent with previous studies [Zha18]. In References [Col17b] and [Mar17] the two triggers, CMSH and CMSL, are combined where CMSL is used in the low- $p_T$  region ( $2 < p_T < 6$  GeV/c) and CMSH is used in the high- $p_T$  region ( $6 < p_T < 20$  GeV/c). In this study we found that the differences are consistently around a factor of 1.1, with the high- $p_T$  trigger (CMSH) yielding a slightly higher cross section. Therefore, from now onwards, the inclusive  $p_T$ -differential production cross section results obtained with the CMSH trigger shall be used in the remainder of this analysis.

In the top panel of Figure 4.3 both triggers are shown as a function of  $\eta$ . The bottom panel shows the ratio of the high- $p_T$  trigger to the low- $p_T$

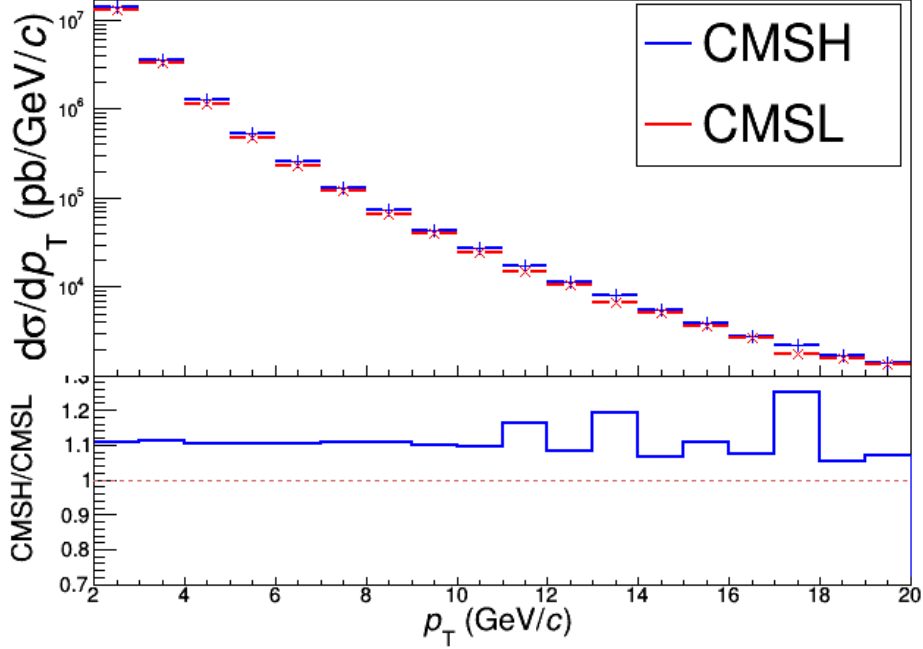


**Figure 4.2:** (Top) Inclusive differential production cross sections of single muons from heavy-flavour decays as a function of  $p_T$  comparing the low- and high- $p_T$  triggers, CMSL and CMSH, with statical errors in the horizontal direction. (Bottom) The ratio of CMSH to CMSL.

trigger below. It is observed that the inclusive  $\eta$ -differential production cross section results show a slight decrease overall with a bump, an increase, at  $\eta = -3.3$ . The cross sections remain constant, in the order of  $10^6$ - $10^7$  pb, over the entire pseudorapidity region. A similar shape is observed for both triggers but is not in agreement with previous results. It was found that the shape is determined mainly by the acceptance and efficiency correction factor, as seen in Figure 3.16. The only available comparative measurement is given in Reference [Mar17], which did not compare the two triggers but the cross section was found to be almost the same order of magnitude. This previous result was more uniform in acceptance and efficiency compared to Figure 3.16. This needs to be investigated further.

From the ratio of the two triggers it can be deduced that the high- $p_T$  trigger (CMSH) yields a slightly higher cross section than the low- $p_T$  trigger. The difference is less than 10%. Similar to the  $p_T$ -differential production cross sections, from now onwards, the  $\eta$ -differential cross sections obtained with the CMSH trigger shall be used in the remainder of this analysis.

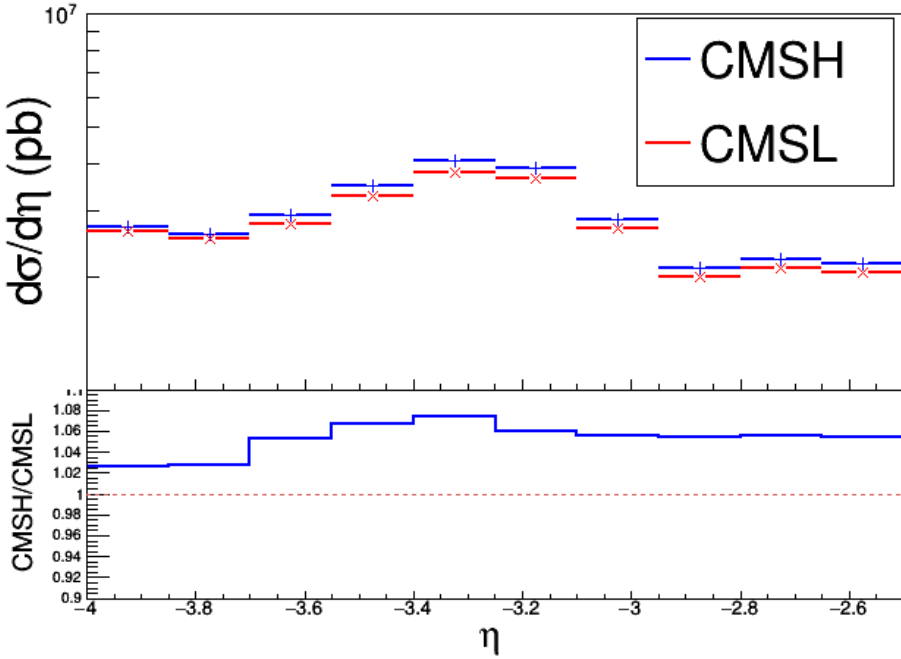


**Figure 4.3:** (Top) Inclusive differential production cross sections of single muons from heavy-flavour decays as a function of  $\eta$  comparing the low- and high- $p_T$  triggers, CMSL and CMSH, with statical errors as horizontal bars. (Bottom) The ratio of CMSH to CMSL.

#### 4.2.2 Comparison with FONLL calculations

Figure 4.4 shows the results (teal) for the high- $p_T$  trigger, CMSH, as a function of  $p_T$  in the range  $2 < p_T < 20$  GeV/ $c$  compared to FONLL predictions for each decay channel in blue, red and green, as well as the total obtained from the summed contribution in black [Nas98]. The predictions account for the correct branching ratios for decays into leptons, as shown in Chapter 3.4. Figure 4.4 includes statistical errors as horizontal bars. It is shown that for FONLL predictions the lighter and more direct hadrons ( $0.7D^0 + 0.3D^+ \rightarrow \mu$  and  $B \rightarrow \mu$ ) are more abundantly produced compared to the heavier hadrons. The indirect production of beauty via charm ( $B \rightarrow D \rightarrow \mu$ ) yields a lower cross section, as demonstrated in Figure 4.4. The same relative contributions for these decay processes are seen at lower energies [Col17b] [Col14b]. Qualitatively, the shape of the measured inclusive differential production cross section of single muons from heavy-flavour decays as a function of  $p_T$  are reproduced by FONLL calculations for the high- $p_T$  muon trigger. The  $p_T$  region of interest for heavy-flavour production is  $2 < p_T < 12$  GeV/ $c$ . Quantitatively, the  $p_T$ -differential production cross section results are underpredicted by the FONLL predictions. In the  $p_T$  interval  $2 < p_T < 6$  GeV/ $c$ , muons from heavy-flavour hadron decays originate predominantly from charmed hadrons, while

muons from beauty-hadron decays dominate over a wide  $p_T$  range,  $6 < p_T < 20 \text{ GeV}/c$ . In the region,  $4 < p_T < 6 \text{ GeV}/c$ , previous results correspond with the crossover seen between charm and beauty direct hadron decays, seen in Figure 4.4 [Col17b] [Col14b].

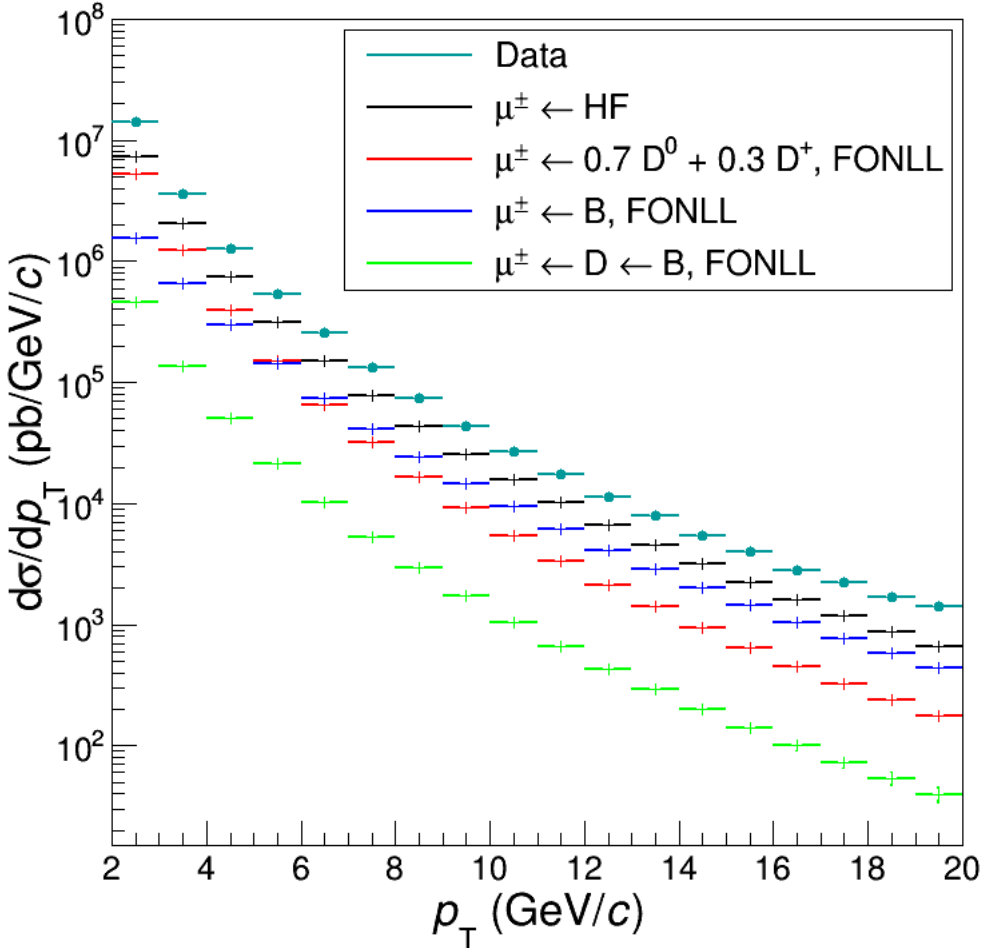


**Figure 4.4:** Inclusive differential production cross sections of single muons from heavy-flavour decays as a function of  $p_T$  for the high- $p_T$  trigger, compared with FONLL results, all with statistical uncertainties in the horizontal direction.

Figure 4.5 shows the measured inclusive differential production cross section (teal) compared with the sum of the FONLL decay channels (black) in the upper panel, and the ratio of the results obtained to the sum of the FONLL decay channels in the lower panel, as a function of  $p_T$ . From the ratio of the results obtained to the FONLL predictions it can be observed that at  $p_T < 6 \text{ GeV}/c$  and  $p_T > 12 \text{ GeV}/c$ , the results obtained are underpredicted by factors 1.7 to 2 and 1.7 to 2.2, respectively. In this study, the region of  $2 < p_T < 12$

$\text{GeV}/c$  could potentially include background muons from light hadron decays, such as pions and kaons, contributing to the cross section at low  $p_T < 6 \text{ GeV}/c$ , as shown, e.g. in Figure 4.1. These low- $p_T$  muons are not accounted for in this analysis. According to [Col14b] and Figure 2 in [Col17b], a contribution from vector boson decay muons is expected to be negligible (< 1%) at  $p_T$  below 12  $\text{GeV}/c$ , however it starts to increase at  $p_T > 12 \text{ GeV}/c$ . The removal of the contributions from hadronic muon background in the  $p_T$  region below 6  $\text{GeV}/c$  as well as of muons from vector bosons in the  $p_T$  region above 12  $\text{GeV}/c$  is expected to decrease the differential production cross section measurements for heavy-flavour decay muons shown in Figure 4.5. The systematic uncertainty of hadronic muon background at low  $p_T$  accounts for 1-4.4% uncertainty and that of muons from vector bosons at high  $p_T$  accounts for 0-1.1%. Overall, the systematic uncertainties range from 0-4.4% as shown in Table 1 in [Col17b]. These systematic uncertainties are not taken into account in this study.

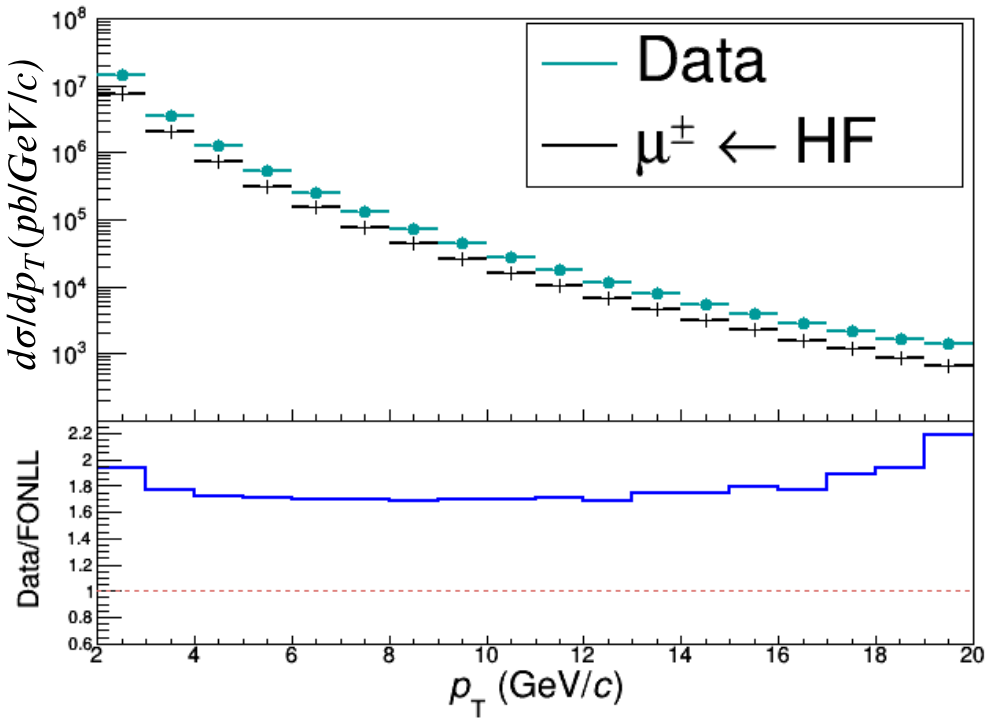


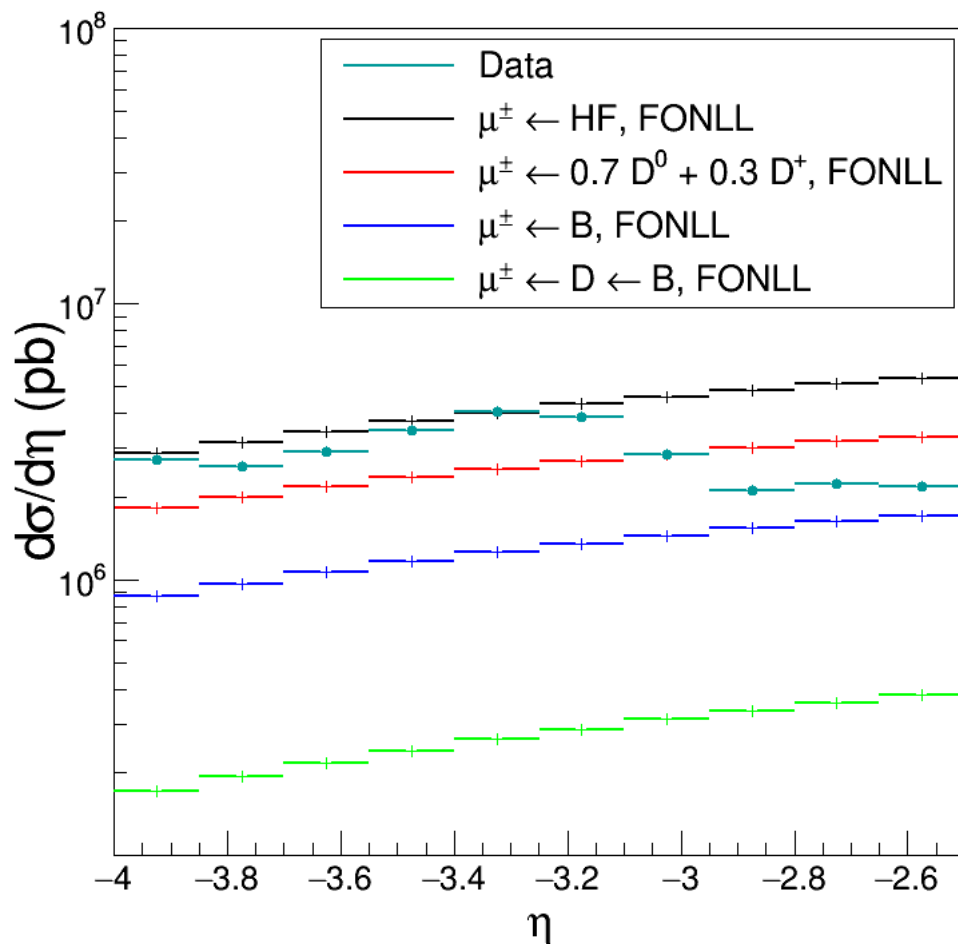
**Figure 4.5:** (Top) Inclusive differential production cross sections of single muons from heavy-flavour decays as a function of  $p_T$  for the high- $p_T$  trigger, compared with the sum of the FONLL decay channels, all with statistical uncertainties as horizontal bars. (Bottom) The ratio of results obtained to the sum of the FONLL decay channels.

Similarly, Figure 4.6 shows the results (teal) for the high- $p_T$  trigger, CMSH,

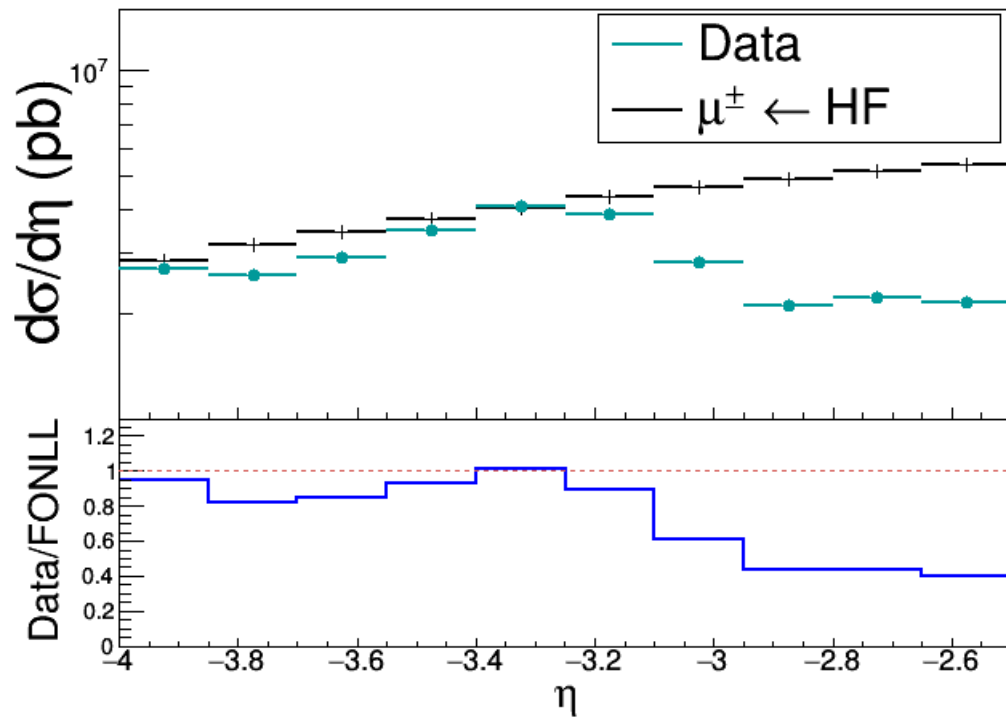
as a function of  $\eta$  in the range  $-4 < \eta < -2.5$  compared to FONLL predictions for each decay channel in blue, red and green, as well as the total obtained from the summed contribution in black [Nas98]. Figure 4.6 includes statistical errors as horizontal bars. It is shown that for FONLL predictions the lighter and more direct hadron decays are more abundantly produced compared to the heavier hadron decays. The shape of the obtained inclusive  $\eta$ -differential production cross section of single muons from heavy-flavour decays is not reproduced by FONLL calculations or previous results. Particularly, within the region  $-3.2 < \eta < -2.5$  a clear deviation is observed. Figure 4.7 shows a decrease in the results obtained but a continuous increase in the FONLL predictions. As mentioned in Section 4.2.1, the shape seen, in particular in the region  $-3.2 < \eta < -2.5$ , could be attributed to acceptance and efficiency effects. The  $\eta$ -differential production cross section results are underpredicted by the FONLL predictions for the direct beauty decay ( $B \rightarrow \mu$ ) and beauty to charm decays ( $B \rightarrow D \rightarrow \mu$ ), as well as the charm decay ( $0.7D^0 + 0.3D^+ \rightarrow \mu$ ) in the region  $-4 < \eta < -3$ , however, between  $-3 < \eta < -2.5$ , they are overpredicted by the FONLL prediction for the charm decay. Globally, the  $\eta$ -differential production cross section results are overpredicted by the sum of these contributions.

Figure 4.7 shows the  $\eta$ -differential production cross section results (teal) compared with the sum of the FONLL decay channels (black) in the upper panel, and the ratio of the results obtained to the sum of the FONLL decay channels in the lower panel. The  $\eta$ -differential production cross section results are overpredicted by the sum of the FONLL decay channels between  $-3.2 < \eta < -2.5$  and almost compatible between  $-4 < \eta < -3.3$ . As a result, the ratio of the obtained distribution to FONLL calculations, shown in the lower panel of Figure 4.7, reduces to  $\sim 0.4$  in the region  $-3 < \eta < -2.5$ .

In summary, Figures 4.4 and 4.6, show the relative contributions of heavy-flavour hadron decays compared to the results obtained. Both  $p_T$  and  $\eta$  FONLL calculations show that the indirect beauty decay ( $B \rightarrow D \rightarrow \mu$ ) has the lowest contribution. The  $\eta$ -distributions show that the direct charm decay ( $0.7D^0 + 0.3D^+ \rightarrow \mu$ ) is consistently higher than the direct beauty decay ( $B \rightarrow \mu$ ), however, in the  $p_T$ -distributions, the direct beauty decay dominates over charm decay at higher- $p_T$ , above  $\sim 6$  GeV/c. The Summary, Conclusion and Outlook follow in the next chapter.



**Figure 4.6:** Inclusive differential production cross sections of single muons from heavy-flavour decays as a function of  $\eta$  for the high- $p_T$  trigger, compared with FONLL results, all shown with statistical uncertainties as horizontal bars.



**Figure 4.7:** (Top) Inclusive differential production cross sections of single muons from heavy-flavour decays as a function of  $\eta$  for the high- $p_T$  trigger, compared with the sum of the FONLL decay channels, all with statistical uncertainties as horizontal bars. (Bottom) The ratio of results obtained to the sum of the FONLL decay channels.

# Chapter 5

## Summary and Conclusion

This study investigated the inclusive differential production cross sections of single muons from heavy-flavour decays as a function of transverse momentum,  $p_T$ , and pseudorapidity,  $\eta$ , in pp collisions at 13 TeV at forward rapidity with ALICE.

### 5.1 Summary

Chapter 1 provided an introduction to ALICE at the LHC, focussing on the forward rapidity regime as it probes small Bjorken- $x$  values that can allow PDF information. A brief discussion of the theoretical background and heavy-flavour production in pp collisions in ALICE was laid out.

Chapter 2 dealt with the ALICE experimental setup, in particular the ALICE Muon Spectrometer and the data taking conditions.

This was followed in Chapter 3 by the analysis of the experimental data and the production of inclusive heavy-flavour single muon cross sections using FONLL calculations ( $c \rightarrow \mu$ ,  $b \rightarrow \mu$  and  $b \rightarrow c \rightarrow \mu$ ). These FONLL calculations are needed for the determination of the acceptance and efficiency correction factor as well as for the cross section predictions in the region  $2 < p_T < 20$  GeV/ $c$ .

The very preliminary results obtained in this study are presented in Chapter 4, excluding the systematic uncertainties and background contributions. In the  $p_T$ -differential production cross section it is observed that the cross section decreases exponentially with increasing  $p_T$ . The results are underpredicted by FONLL calculations, by almost a factor of 2. The relative contributions to the FONLL production cross section calculations at  $\sqrt{s} = 13$  TeV are consistent with studies at lower energies, both as a function of  $p_T$  and  $\eta$ . However, in the region of interest of this study,  $2 < p_T < 12$  GeV/ $c$ , where muons from the decay of heavy-flavours dominate, the ratios between FONLL calculations and the measurements are about 1.6. Qualitatively, these very preliminary results of  $p_T$ -differential production cross sections of single muons from heavy-

flavour decays are consistent with previous measurements. Overall, the shape of the  $p_T$ -differential cross section is well reproduced by FONLL calculations. The inclusive differential production cross section as a function of  $\eta$  exhibits a different trend to what is expected. The FONLL predictions deviate from measured data, particularly between  $-3.2 < \eta < -2.5$ . This shape is not observed in previous measurements. Further investigations are needed in this case.

## 5.2 Conclusion

The shape of the  $p_T$ -differential production cross sections of single muons from heavy-flavour decays are consistent with previous measurements at lower centre-of-mass energies. Qualitatively, the FONLL predictions underestimate the measurements. However, in the region of interest,  $2 < p_T < 12$  GeV/ $c$ , the difference reduces to 40%. At low- $p_T$ ,  $2 < p_T < 6$  GeV/ $c$ , the dominant process is the charm decay ( $0.7D^0 + 0.3D^+ \rightarrow \mu$ ) and at mid- to high- $p_T$ ,  $6 < p_T < 20$  GeV/ $c$ , the dominant process is the direct beauty decay ( $B \rightarrow \mu$ ). The shape of the  $\eta$ -differential production cross section of single muons from heavy-flavour decays is not in agreement with previous results. This can be attributed to the acceptance and efficiency correction factor. The decreasing trend is in contrast with previous measurements and FONLL predictions. The calculations, in particular the charm decay ( $0.7D^0 + 0.3D^+ \rightarrow \mu$ ), overestimate the measurements between  $-3 < \eta < -2.5$  by  $\sim 40\text{-}60\%$ . Further investigations are needed. Preliminary inclusive differential production cross sections of single muons from heavy-flavour decays as a function of  $p_T$  and  $\eta$  at  $\sqrt{s} = 13$  TeV are presented. The results obtained can provide PDF information as well as serve as a test for pQCD model calculations. Both  $p_T$ - and  $\eta$ -distributions are used for the identification of particles. The modification of the  $p_T$ -differential production cross sections of single muons from heavy-flavour decays in HIC to pp collisions serve as a probe of the QGP.

## 5.3 Outlook

The results presented in this thesis are very preliminary. They do not include systematic uncertainties nor background subtraction needed to extract the signal of heavy-flavour decay muons in the region  $6 < p_T < 12$  GeV/ $c$ . In the future, a comprehensive study of single muon background and systematic uncertainties would be vital to extract the single-muon differential cross sections. These inclusions would enable a realistic comparison with previous measurements and FONLL calculations. The latter will represent an important test of perturbative Quantum Chromodynamics as heavy-flavour production cross sections in pp collisions can be estimated in the framework of pQCD due to

their production in initial hard partonic scatterings. The discrepancies in the  $\eta$ -differential cross sections need to be investigated in future studies.

Also, until now, with the ALICE Muon Spectrometer, only inclusive measurements of heavy-flavour decays could be performed due to limitations in the mass resolution in the Muon Spectrometer and the lack of detectors close to the interaction vertex. As such, tracks could not be reconstructed to separate muons from charm and beauty decays. In future studies, it is envisaged to measure heavy-flavour decays exclusively at forward rapidity. This will be facilitated by the installation of the Muon Forward Tracker, which will be placed in between the ITS and the Front Absorber of the Muon Spectrometer. Improved measurements will allow us to differentiate between a charm decaying into a muon and a bottom decaying into a muon. This will not only help in understanding heavy-flavour hadron production measured with the Muon Spectrometer, but will also provide results that can complement those measured with the central barrel where exclusive open heavy-flavour measurements in the semielectronic channel are already possible. As a result, the data collected in Run 3, which will make use of these installations, will further help to interpret current and other existing studies.

# List of References

- [Bai19] O. V. Baillie. ALICE trigger system: Present and Future. <https://ep-news.web.cern.ch/content/alice-trigger-system-present-and-future>, 2019. [Online; accessed 2020-02-24].
- [BC03] R. Bailey and P. Collier. Standard Filling Schemes for Various LHC Operation Modes. Technical Report LHC-PROJECT-NOTE-323, CERN, Geneva, Sep 2003.
- [Bet07] S. Bethke. Experimental tests of asymptotic freedom. *Progress in Particle and Nuclear Physics*, 58:351–386, 2007.
- [BW17] Y. Nie, R. Schmidt, V. Chetvertkova, G. Rosell-Tarragó, F. Burkart and D. Wollmann. Numerical simulations of energy deposition caused by 50 MeV-50 TeV proton beams in copper and graphite targets. *Physical Review Accelerators and Beams*, 20, 2017.
- [CERa] CERN. LHC Machine Outreach. <https://lhc-machine-outreach.web.cern.ch/lhc-machine-outreach>. [Online; accessed 2019-06-19].
- [CERb] CERN. Taking a closer look at LHC, Proton Source. [https://www.lhc-closer.es/taking\\_a\\_closer\\_look\\_at\\_lhc/0.proton\\_source](https://www.lhc-closer.es/taking_a_closer_look_at_lhc/0.proton_source). [Online; accessed 2019-19-18].
- [CER19] CERN. The Large Hadron Collider. <https://home.cern/science/accelerators/large-hadron-collider>, 2019. [Online; accessed 2019-09-18].
- [Cola] ALICE Collaboration. ALICE Collaboration Shifts Instructions: Shift Leader Documentation:. [https://svnweb.cern.ch/cern/wsvn/alicep2/ShiftLeaders/SL\\_course.pdf](https://svnweb.cern.ch/cern/wsvn/alicep2/ShiftLeaders/SL_course.pdf). [Online; accessed 2019-01-05].
- [Colb] ALICE Collaboration. Luminosity Plot ALICE performance 2017 pp  $\sqrt{s} = 13$  TeV. [https://aliquaevseos.web.cern.ch/aliquaevseos/data/2017/lumi\\_public\\_13TeV\\_2017.png](https://aliquaevseos.web.cern.ch/aliquaevseos/data/2017/lumi_public_13TeV_2017.png). [Online; accessed 2020-02-03].

- [Col99] ALICE Collaboration. *ALICE dimuon forward spectrometer: Technical Design Report*. Technical Design Report ALICE. CERN, Geneva, 1999.
- [Col00] ALICE Collaboration. Addendum to the Technical Design Report of the Dimuon Forward Spectrometer. [https://aliceinfo.cern.ch/secure/system/files/documents/technical\\_coordination/tdr2-main.pdf](https://aliceinfo.cern.ch/secure/system/files/documents/technical_coordination/tdr2-main.pdf), 2000. [Online; accessed 2019-07-15].
- [Col04] ALICE Collaboration. The Physics Performance Report Volume 1. *Journal of Physics*, G30(1527):216–227, 2004.
- [Col08] ALICE Collaboration. The ALICE experiment at the CERN LHC. *Journal of Instrumentation*, 3(8), 2008.
- [Col09] V. Chambert, ALICE Collaboration. The electronics of ALICE Dimuon tracking chambers. <https://cds.cern.ch/record/1158633/files/p242.pdf>, 2009. [Online; accessed 2019-07-17].
- [Col10] ALICE Collaboration. First proton-proton collisions at the LHC as observed with the ALICE detector: measurement of the charged particle pseudorapidity density at  $\sqrt{s} = 900$  GeV. *European Physical Journal*, C65:111–125, 2010.
- [Col12a] ALICE Collaboration. Measurement of charm production at central rapidity in proton-proton collisions at  $\sqrt{s} = 2.76$  TeV. *Journal of High Energy Physics*, 7(191), 2012.
- [Col12b] ALICE Collaboration. Measurement of electrons from semileptonic heavy-flavour hadron decays in pp collisions at  $\sqrt{s} = 7$  TeV. *Physics Review*, D86(112007), 2012.
- [Col12c] ALICE Collaboration. Production of muons from heavy flavour decays at forward rapidity in pp and pb-pb collisions at  $\sqrt{s} = 2.76$  TeV. *Physical Review Letters*, 109(112301), 2012.
- [Col12d] ATLAS Collaboration. Observation of a new particle in the search of the Standard Model Higgs boson with the ATLAS detector at the LHC. *Physics Letters*, B716(1-29), 2012.
- [Col12e] CMS Collaboration. Observation of a new boson at a mass of 125 GeV with the CMS experiment at the LHC. *Physics Letters*, B716(30), 2012.
- [Col14a] ALICE Collaboration. Beauty production in pp collisions at  $\sqrt{s} = 2.76$  TeV measured via semi-electronic decays. *Physics Letters*, B738(97), 2014.

- [Col14b] ALICE Collaboration. Heavy flavour decay muon production at forward rapidity in proton-proton collisions at  $\sqrt{s} = 7$  TeV. *Physics Letters*, B728:216–227, 2014.
- [Col14c] ALICE Collaboration. Performance of the ALICE experiment at the CERN LHC. *International Journal of Modern Physics*, A29(1430044):24, 2014.
- [Col16a] ALICE Collaboration. Analyses of van der Meer scans taken with pp collisions in 2015, 2016. Analysis Note for the Physics Working Group-Ultraperipheral and Diffraction.
- [Col16b] ALICE Collaboration. Measurement of electrons from beauty hadron decays in pp collisions at  $\sqrt{s} = 7$  TeV. *Physics Letters*, B763(507), 2016.
- [Col17a] ALICE Collaboration. Physics Working Group Muon: Muon QA: Lhc17k muon\_calo\_pass2 Muon pp QA. <https://twiki.cern.ch/twiki/bin/view/ALICE/MuonppQA2017>, 2017. [Online; accessed 2019-12-10].
- [Col17b] ALICE Collaboration. Production of muons from heavy-flavour hadron decays in pp collisions at  $\sqrt{s} = 5.02$  TeV. *Physics Letters*, B770(459-472), 2017.
- [Col18] ALICE Collaboration. ALICE 2017 luminosity determination for pp collisions at  $\sqrt{s} = 5$  TeV. <https://cds.cern.ch/record/2648933/files/vdmNote.pdf>, 2018. [Online; accessed 2019-12-8].
- [Col19a] ALICE Collaboration. ALICE offline: Framework for raw data. <https://alice-offline.web.cern.ch/Activities/Raw-Data.html>, 2019. [Online; accessed 2020-01-22].
- [Col19b] ALICE Collaboration. ALICE Twiki CERN, Event Normalization *InternalPrivateCommunication*. <https://twiki.cern.ch/twiki/bin/viewauth/ALICE/EventNormalization>, 2019. [Online; accessed 2020-01-6].
- [DF08] N. A. Tahir, R. Schmidt, M. Brugger, R. Assmann, A. V. Shutov, I. V. Lomonosov, A. R. Piriz, D. H. H. Hoffmann, C. Deutsch and V. E. Fortov. The CERN super proton synchrotron as a tool to study high energy density physics. *New Journal of Physics*, 10(073028), 2008.
- [ea03] S. Agostinelli, *et al.* GEANT4-a simulation toolkit. *Nuclear Instruments and Methods in Physics*, A506:2250–303, 2003.
- [ea08] P. M. Nodolsky, *et al.* Implications of CTEQ global PDF analysis for collider observables. *Physical Review*, D78(013004), 2008.

- [ea12] J. Beringer, *et al.* Review of Particle Physics. *Physics Review*, D86(010001), 2012.
- [ea18] R. Rapp, P.B. Gossiaux, *et al.* Extraction of heavy-flavor transport coefficients in QCD matter. *Nuclear Physics A*, 979:21 – 86, 2018.
- [Fin06] C. Finck. The Muon Spectrometer of the ALICE. *Journal of Physics: Conference Series*, 50:397–401, 2006.
- [FJ05] A. Ferrari, P. R. Sala, A. Fass and J.Ranft. *FLUKA: A multi-particle transport code (program version 2005)*. CERN Yellow Reports: Monographs. CERN, Geneva, 2005.
- [fPPPI] Institute for Particle Physics Phenomenology (IPPP). Modelling the invisible: The Standard Model. <https://www.modellinginvisible.org/standard-model/>. [Online; accessed 2019-09-01].
- [gW94] M. gyulassy and X.-N. Wang. HIJING 1.0:a Monte HIJING 1.0: A Monte Carlo program for parton and particle production in high energy hadronic and nuclear collisions. *Computational Physics Community*, 83(307), 1994.
- [Kea17] D. Keane. The Beam Energy Scan at the Relativistic Heavy Ion Collider. *Journal of Physics: Conference Series*, 878(012015), 2017.
- [Kha06] D. Kharzeev. The physics of strong color fields: New frontier of QCD. *ACTA PHYSICA POLONICA*, B37(12), 2006.
- [Kra12] I. Schienbein, H. Spiesberger, B. A. Kniehl, G. Kramer. Inclusive charmed-meson production at the CERN LHC. *The European Physical Journal*, C72(7), 2012.
- [Kry14] E. Kryshen. Analysis tutorial. 2014.
- [KT05] P. Pillot, J. Y. Grossiord, V. Kakoyan and R. Tieulent. The geometry monitoring system of the ALICE muon spectrometer: simulation results. *ALICE Internal Note*, 20, 2005.
- [Mar17] M. Marchisone. Muon production from open heavy flavours in pp collisions at  $\sqrt{s} = 8$  TeV: cross section and multiplicity dependence, 2017. Analysis Note for the Physics Working Group-Heavy-flavour (ANA-642).
- [Mhl15] S. Mhlanga. The study of the production of heavy-flavour muons as a function of charged-particle multiplicity in proton-proton collisions at 8 TeV with ALICE at the LHC. Master’s thesis, University of Cape Town, 2015.

- [Mil13] L. Milano. Transverse momentum spectra of hadrons identified with the ALICE Inner Tracking System, 2013.
- [MN15] M. Cacciari, M. L. Mangano and P. Nason. Gluon PDF constraints from the ratio of forward heavy-quark production at the lhc at  $\sqrt{s} = 7$  and 13 TeV. *European Physical Journal J*, C75(12), 2015.
- [Nas98] M. Cacciari, M. Greco, P. Nason. The  $p_T$  spectrum in heavy-flavour hadroproduction. *Journal of High Energy Physics*, (05):007, 1998.
- [NO07] S. Frixione, P. Nason and C. Oleari. Matching NLO QCD computations with parton shower simulations: the POWHEG method. *Journal of High Energy Physics*, 11(70), 2007.
- [NR92] M. L. Mangano, P. Nason and G. Ridolfi. Heavy quark correlations in hadron collisions at next-to-leading order. *Nuclear Physics*, B373(295), 1992.
- [oEB] Editors of Encyclopaedia Britannica. Antiparticle. <https://www.britannica.com/science/antiparticle>. [Online; accessed 2020-02-08].
- [Pal17] L. Palomo. The ALICE experiment upgrades for LHC run 3 and beyond: contributions from mexican groups. *Journal of Physics Conference Series*, 912(012023), 2017.
- [Rei03] L. Lyons, R. P. Mount, R. Reitmeyer. Statistical problems in particle physics, astrophysics and cosmology. <http://www-public.slac.stanford.edu/sciDoc/docMeta.aspx?slacPubNumber=slac-r-703>, 2003.
- [RL04] F. Jouve, P. Rosnet and L. Royer. Front-End Electronics of the ALICE dimuon trigger, 2004.
- [Sar] A. Sarkar. W and Z boson Production in Heavy Ion Collision at 5 TeV. [https://indico.cern.ch/event/591325/contributions/2386599/attachments/1380120/2097670/W\\_Analysis\\_Heavy\\_Ion\\_5TeV\\_ALICE.pdf](https://indico.cern.ch/event/591325/contributions/2386599/attachments/1380120/2097670/W_Analysis_Heavy_Ion_5TeV_ALICE.pdf). [Online; accessed 2020-02-27].
- [Sch12] J. Schukraft. Heavy-ion physics with the ALICE experiment at the CERN Large Hadron Collider. *Philosophical transactions. Series A, Mathematical, physical, and engineering sciences*, 370:917–32, 2012.
- [Sen17] K. J. Senosi. *Vector boson production with the ALICE detector*. PhD thesis, University of Cape Town, 2017.

- [Shi08] I. Shipsey. A win-win situation. *Nature Physics*, 4:438–440, 2008.
- [Ska06] T. Sjöstrand, S. Mrenna, P. Skands. PYTHIA 6.2 Physics and Manual. *Journal of High Energy Physics*, 605:26, 2006.
- [SS89] J. C. Collins, D. E. Soper, and G. F. Sterman. Factorization of hard processes in QCD. *Advanced Service Direct High Energy Physics*, 5:1–91, 1989.
- [Tho18] M. Thomson. *Modern Particle Physics*. Cambridge University Press, 3 edition, 2018.
- [vdGHGCGFLR00] H. van der Graaf, H. Groenstege, C. Guyot, F. Linde and P. Rewiersma. RasNiK, an alignment system for the ATLAS MDT barrel muon chambers. *NIKHEF Internal Note*, 4, 2000.
- [Ver00] R. Arnaldi, A. Baldit, V. Barret, N. Bastid, G. Blanchard, E. Chiavassa, P. Cortese, P. Crochet, G. Dellacasa, N. De Marco, P. Dupieux, B. Espagnon, J. Fargeix, A. Ferretti, M. Gallio, L. Lamoine, L. Luquin, F. Manso, V. Metivier, A. Musso, A. Piccotti, A. Rahmani, O. Roig, L. Royer, E. Scalas, E. Scomparin, E. Vercellin. A low-resistivity RPC for the ALICE dimuon arm. *Nuclear Instruments and Methods in Physics*, A451(462), 2000.
- [Zha12] X. Zhang. *Study of Heavy Flavours from Muons Measured with the ALICE Detector in Proton-Proton and Heavy-Ion Collisions at the CERN-LHC*. PhD thesis, Clermont-Ferrand U., 2012.
- [Zha18] Z. Zhang. Production of muons from heavy-flavour decays in pp collisions at  $\sqrt{s} = 5.02$  TeV, 2018. Analysis Note for the Physics Working Group-Heavy-flavour (ANA-671).

# Appendices

# Run list

Below are the runlists of the data periods analysed for this study, LHC17h and LHC17k muon\_calo\_pass2 AliAOD runs.

Period	runlist
LHC17h	273103 273101 273100 273099 273077 273010 273009 272985 272983 272976 272949 272947 272939 272935 272934 272933 272932 272905 272903 272880 272873 272871 272870 272836 272835 272834 272833 272829 272828 272784 272783 272782 272762 272760 272749 272747 272746 272692 272691 272620 272619 272608 272607 272585 272577 272575 272574 272521 272469 272468 272466 272463 272462 272461 272414 272413 272411 272400 272394 272360 272359 272335 272194 272156 272155 272154 272153 272152 272151 272123 272101 272100 272076 272075 272042 272041 272040 272039 272038 272036 272034 272030 272029 272025 272020 271970 271969 271962 271955 271953 271946 271925 271921 271915 271912 271886 271879 271878 271874 271873 271871 271870 271868
LHC17k	276508 276507 276506 276500 276462 276461 276439 276438 276437 276435 276434 276432 276429 276351 276348 276312 276307 276302 276297 276294 276292 276291 276290 276259 276230 276205 276178 276177 276170 276169 276166 276145 276141 276140 276108 276105 276104 276102 276099 276098 275664 275661 275657 275650 275648 275624 275559 275558 275515 275472 275471 275467 275459 275457 275453 275452 275448 275406 275404 275401 275369 275361 275360 275357 275332 275328 275283 275247 275246 275245 275188 275177 275175 275174 275173 275151 275150 275149 275076 275075 275073 275070 275068 275067 274979 274978 274886 274884 274883 274882 274822 274817 274815 274811 274807 274806 274803 274802 274801 274743 274736 274708

# runGrid.C

```
void runGrid()
{
    // Load common libraries
    gSystem->Load("libCore.so");
    gSystem->Load("libTree.so");
    gSystem->Load("libGeom.so");
    gSystem->Load("libVMC.so");
    gSystem->Load("libPhysics.so");
    gSystem->Load("libMinuit.so");
    gSystem->Load("libSTEERBase");
    gSystem->Load("libESD");
    gSystem->Load("libAOD");
    gSystem->Load("libANALYSIS");
    gSystem->Load("libANALYSISalice");
    gSystem->Load("libCORRFW");
    gSystem->Load("libPWGmuon");
    gROOT->ProcessLine(".include $ROOTSYS/include");
    gROOT->ProcessLine(".include $ALICE_ROOT/include");
    gSystem->SetIncludePath("-I.$ALICE_ROOT/include -I$ROOTSYS/include
                           -I$ALICE_ROOT/MUON -I$ALICE_ROOT/include -I$ALICE_PHYSICS
                           /include");

    // Create and configure the alien handler plugin
    gROOT->LoadMacro("CreateAlienHandler.C");
    AliAnalysisGrid *alienHandler = CreateAlienHandler();
    if (!alienHandler) return;

    // Create the analysis manager
    AliAnalysisManager *mgr = new AliAnalysisManager
    ("AliAnalysisExamplePt");

    // Connect plug-in to the analysis manager
    mgr->SetGridHandler(alienHandler);

    gROOT->LoadMacro("AliAnalysisExamplePt.cxx++g");

    AliAODInputHandler *aodH = new AliAODInputHandler();
    mgr->SetInputEventHandler(aodH);
```

```
AliAnalysisExamplePt *task = new
    AliAnalysisExamplePt("AliAnalysisExamplePt");

    // Create containers for input/output
    AliAnalysisDataContainer *cinput = mgr->
    GetCommonInputContainer();
    AliAnalysisDataContainer *coutput = mgr->
    CreateContainer("chist",
        TList::Class(),     AliAnalysisManager::kOutputContainer,
        "gridoutput.AOD.1.root");

    // Connect input/output
    mgr->AddTask(task);
    mgr->ConnectInput(task, 0, cinput);
    mgr->ConnectOutput(task, 1, coutput);

    // Enable debug printouts
    mgr->SetDebugLevel(0);

    if (!mgr->InitAnalysis())
        return;

    mgr->PrintStatus();
    // Start analysis in locally
    // mgr->StartAnalysis("local");
    // Start analysis in grid
    mgr->StartAnalysis("grid");
};

}
```

# AliAnalysisExamplePt.cxx

```
#include "TChain.h"
#include "TTree.h"
#include "TH1F.h"
#include "TCanvas.h"
#include <iostream>
#include "AliAnalysisTask.h"
#include "AliAnalysisManager.h"
#include "AliAODEvent.h"
#include "AliAODTrack.h"
#include "AliMuonTrackCuts.h"
#include "AliAODInputHandler.h"
#include "AliAnalysisExamplePt.h"
#include "AliAODVertex.h"
#include "AliMuonEventCuts.h"

// example of an analysis task creating a p_t spectrum
// Authors: Panos Cristakoglou, Jan Fiete Grosse-Oetringhaus,
// Christian Klein-Boesing
// Reviewed: A.Gheata (19/02/10)
ClassImp(AliAnalysisExamplePt)
//-----
//***// Here is where you initialise your objects //***//
//***// Make sure to declare in AliAnalysisExamplePt.h//***//
AliAnalysisExamplePt::AliAnalysisExamplePt(const char *name)
    : AliAnalysisTaskSE(name), fAOD(0), fMuonTrackCuts(0),
    fMuonEventCuts(0), fOutputList(0), fHistEta(0),
    fHistVertex(0), fHistPt(0), fHistpDCA(0), fTrack(0)
{
    // Constructor
    fMuonTrackCuts = new AliMuonTrackCuts(Form
("TrackCuts_%s",name), "TrackCuts");
    fMuonTrackCuts -> SetFilterMask(AliMuonTrackCuts::kMuEta
|AliMuonTrackCuts::kMuThetaAbs|AliMuonTrackCuts::kMuMatchLpt
|AliMuonTrackCuts::kMuPdca);
//-----
//***// Implement Physics selection on events//***//
fMuonEventCuts = new AliMuonEventCuts("event","event");
fMuonEventCuts -> SetFilterMask(AliMuonEventCuts::kSelectedTrig
```

```

| AliMuonEventCuts::kPhysicsSelected |
AliMuonEventCuts::kGoodVertex);
fMuonEventCuts->SetTrigClassPatterns("CMSPH7-B-NOPF-MUFAST");
//-----//
```

```

Bool_t useMC = kFALSE;
fMuonTrackCuts->SetIsMC(useMC); //montecarlo
fMuonTrackCuts->Print("mask");
fMuonTrackCuts->SetAllowDefaultParams(kTRUE);
fMuonTrackCuts->ApplySharpPtCutInMatching(kTRUE);
    // Define input and output slots here
    // Input slot #0 works with a TChain
    DefineInput(0, TChain::Class());
    // Output slot #0 id reserved by the base class for AOD
    // Output slot #1 writes into a TH1 container
    DefineOutput(1, TList::Class());
}
//-----
void AliAnalysisExamplePt::UserCreateOutputObjects()
{
    // Create histograms
    // Called once

    fOutputList = new TList();

///////////////////////////////
```

```

fHistVertex=new TH1F("fHistVertex","Vertexdistribution",
60, -15, 15);
fHistVertex->GetXaxis()->SetTitle("Zvertex(cm)");
fHistVertex->GetYaxis()->SetTitle("Events");
fHistVertex->SetMarkerStyle(kFullCircle);

fHistpDCA = new TH2D("fHistpDCA", "p_{T} vs pDCA",
1000, 0, 20, 10000, 0, 100000);
fHistpDCA->GetXaxis()->SetTitle("p_{T}(GeV/c)");
fHistpDCA->GetYaxis()->SetTitle("pDCA");
fHistpDCA->SetMarkerStyle(kFullCircle);

fHistPt = new TH1F("fHistPt", "P_{T}distribution",
10000, 0, 100);
fHistPt->GetXaxis()->SetTitle("P_{T}(GeV/c)");
fHistPt->GetYaxis()->SetTitle("dN/dP_{T}(c/GeV)");
fHistPt->SetMarkerStyle(kFullCircle);

fHistEta = new TH1F("fHistEta", "Etadistribution",
240,-4.2,-2.4);
fHistEta->GetXaxis()->SetTitle("#eta");
```

```

fHistEta->GetYaxis()->SetTitle("dN/d#eta_{lab} (c/GeV)");
fHistEta->SetMarkerStyle(kFullCircle);

///////////////////////////////
fOutputList->Add(fHistVertex);
fOutputList->Add(fHistpDCA);
fOutputList->Add(fHistPt);
fOutputList->Add(fHistEta);

///////////////////////////////
PostData(1,fHistVertex);
PostData(1,fHistpDCA);
PostData(1,fHistPt);
PostData(1,fHistEta);

///////////////////////////////
PostData(1,fOutputList);
}

///////////////////////////////

void AliAnalysisExamplePt::NotifyRun()
{
    fMuonTrackCuts->SetRun(fInputHandler);
}
//-----
void AliAnalysisExamplePt::UserExec(Option_t * /*option*/)
{
    // Main loop
    // Called for each event
    // Post output data.
    fAOD = dynamic_cast<AliAODEvent*>(InputEvent());
    if (!fAOD) {
        printf("ERROR: fAOD not available\n");
        return;
    }

//-----
    if (!fMuonEventCuts->IsSelected(fInputHandler)) return;
//-----

    AliAODVertex *vz = fAOD->GetPrimaryVertexSPD();
    if (vz->GetZ() >-10. && vz->GetZ() < 10. ){
        fHistVertex->Fill(vz->GetZ());
    }
    //Loop over the events
}

```

```

for ( Int_t iTracks = 0; iTracks < fAOD->GetNumberOfTracks();  

iTracks++ )  

{  

    AliAODTrack* track = dynamic_cast<AliAODTrack*>  

    (fAOD->GetTrack(iTracks));  

    if (!track) {  

        printf("ERROR: Could not receive track %d\n", iTracks);  

        continue;  

    }  

//-----  

if (!fMuonTrackCuts->IsSelected(track)) continue;  

//-----  

// PT DISTRIBUTION WITH DCA  

    fHistpDCA->Fill(track->Pt(), track->P()*track->DCA());  

// PT DISTRIBUTION  

    fHistPt->Fill(track->Pt());  

// // Eta DISTRIBUTION  

    fHistEta->Fill(track->Eta());  

} //track loop  

PostData(1, fOutputList);
}  

//-----  

void AliAnalysisExamplePt::Terminate(Option_t *)
{
    // Draw result to the screen
    // Called once at the end of the query

    fOutputList = dynamic_cast<TList*>(GetOutputData(1));
    if (!fOutputList) {
        printf("ERROR: Output list not available\n");
        return;
    }

    fHistVertex= dynamic_cast<TH1F*> (fOutputList->At(0));
    if (!fHistVertex) {
        printf("ERROR: fHistVertex not available\n");
        return;
    }

    fHistpDCA = dynamic_cast<TH2D*> (fOutputList->At(1));
    if (!fHistpDCA) {

```

```
    printf("ERROR:fHistpDCA not available\n");
    return;
}

fHistPt = dynamic_cast<TH1F*> (fOutputList->At(2));
if (!fHistPt) {
    printf("ERROR:fHistPt not available\n");
    return;
}

fHistEta = dynamic_cast<TH1F*> (fOutputList->At(3));
if (!fHistEta) {
    printf("ERROR:fHistEta not available\n");
    return;
}

///////////////////////////////
TCanvas *cfHistVertex = new TCanvas("fHistVertex",
"fHistVertex", 10,10,510,510);
cfHistVertex->cd(1)->SetLogy();
fHistVertex->SaveAs("vertex_LHC17h_CMSH.root");
fHistVertex->DrawCopy("E");

TCanvas *cpDCA = new TCanvas("fHistpDCA","fHistpDCA",
10,10,510,510);
cpDCA->cd(1)->SetLogz();
fHistpDCA->DrawCopy("colz");
fHistpDCA->SaveAs("ptvspdca_LHC17h_CMSH.root");

TCanvas *cPt = new TCanvas("Pt","Pt",10,10,510,510);
cPt->cd(1)->SetLogy();
fHistPt->DrawCopy("E");
fHistPt->SaveAs("pt_LHC17h_CMSH.root");

TCanvas *cEta = new TCanvas("Eta","Eta",10,10,510,510);
cEta->cd(1)->SetLogy();
fHistEta->DrawCopy("E");
fHistEta->SaveAs("eta_LHC17h_CMSH.root");

/////////////////////////////
}
```

# sim.C

```
void sim(Int_t nev=3000)
{
#ifndef __CINT__
    gSystem->Load("liblhapdf"); // Parton density functions
    if ( 0 )
    {
        std::cout
            << "Setting up Pythia6 required env. variables"
            << std::endl;
    }
    else   gSystem->Load("libpythia6"); //Pythia 6.2
    if ( 0 )
    {
        std::cout
            << "Setting up Pythia8 required libraries and
            << env. variables"
            << std::endl;
//gSystem->Load("libpythia8");
//gSystem->Load("libAliPythia8");
    }
#endif
    AliSimulation_ssimulator;
    simulator.SetRunQA("MUON:ALL");
    simulator.SetRunHLT("");
    simulator.SetDefaultStorage("raw://");
    if (kFALSE) simulator.SetCDBSnapshotMode("OCDB_sim.root");
    if ( 0 )
    {
        simulator.SetMakeSDigits("MUON_T0_VZERO");
        // T0 and VZERO for trigger efficiencies,
        // FMD for diffractive studies
        simulator.SetMakeDigitsFromHits("ITS");
        // ITS needed to propagate the simulated vertex
        simulator.SetMakeDigits("MUON_T0_VZERO");
        // ITS); // ITS needed to propagate the simulated vertex
    }
    else
    {
```

```

simulator.SetTriggerConfig("MUON");
simulator.SetMakeSDigits("MUON");
simulator.SetMakeDigits("MUON");
// ITS); // ITS needed to propagate the simulated vertex
}
if ( 0 ) {
    TGeoGlobalMagField::Instance() -> SetField(new AliMagF
        ("Maps","Maps", -1., -1, AliMagF::k5kG));
}
else {
    // Mag.field from OCDB
    simulator.UseMagFieldFromGRP();
    // MUON Tracker
    if ( 1 )
    {
        simulator.SetSpecificStorage("MUON/Align/Data",
            "alien://folder=/alice/simulation/2008/v4-15-
uuuuuuRelease/Full");
    }
    else
    {
        simulator.SetSpecificStorage("MUON/Align/Data",
            "alien://folder=/alice/simulation/2008/v4-15-
uuuuuuRelease/Ideal");
    }
    // ITS
    if ( 0 )
    {
        simulator.SetSpecificStorage("ITS/Align/Data",
            "alien://Folder=/alice/simulation/2008/v4-15-
uuuuuuRelease/Ideal");
    }
    if ( 0 || 1 )
    {
        simulator.UseVertexFromCDB();
    }
}
// The rest
TStopwatch timer;
timer.Start();
simulator.Run(nev);
timer.Stop();
timer.Print();
}

```

## rec.C

```
void rec() {
    AliReconstruction reco;
    // run/run (No RejectList)
    reco.SetCleanESD(kFALSE);
    reco.SetStopOnError(kFALSE);
    reco.SetRunQA("MUON:ALL");
    //reco.SetRunLocalReconstruction("MUON");
    //reco.SetRunTracking("MUON");
    //reco.SetFillESD("MUON");
    //reco.SetRunVertexFinder(kFALSE);
    ////kTRUE by default (kFALSE if no SPD/ITS)
    reco.SetRunReconstruction("MUON");
    // Default = raw OCDB
    reco.SetDefaultStorage("alien://Folder=/alice/data/2017/
    //OCDB");
    // GRP from local OCDB
    reco.SetSpecificStorage("GRP/GRP/Data",
    Form("local://%s",gSystem->pwd()));
    //AliCDBManager* man = AliCDBManager::Instance();
    //man->SetDefaultStorage("alien://folder=/alice/data/2015/
    //OCDB");
    //man->SetSpecificStorage("GRP/GRP/Data",
    //Form("local://%s",gSystem->pwd()));
    //man->SetSpecificStorage("MUON/Align/Data",
    //"alien://folder=/alice/data/2015/OCDB",5);
    TStopwatch timer;
    timer.Start();
    reco.Run();
    timer.Stop();
    timer.Print();
}
```

# trigger.C

```
#if defined(__CINT__)
/////////////////////////////Load common libraries
#include "/home/amal/alice/sw/ubuntu1604_x86-64/AliRoot/0-1/include/AliCDBEntry.h"
#include "/home/amal/alice/sw/ubuntu1604_x86-64/AliRoot/0-1/include/AliCDBManager.h"
#include "/home/amal/alice/sw/ubuntu1604_x86-64/AliRoot/0-1/include/AliGRPObject.h"
#include "/home/amal/alice/sw/ubuntu1604_x86-64/AliRoot/0-1/include/AliLog.h"
#include "/home/amal/alice/sw/ubuntu1604_x86-64/AliRoot/0-1/include/AliLHCData.h"
//Use AliRoot includes to compile our task
gSystem->Load("libCore.so");
gSystem->Load("libTree.so");
gSystem->Load("libGeom.so");
gSystem->Load("libVMC.so");
gSystem->Load("libPhysics.so");
gSystem->Load("libMinuit.so");
gSystem->Load("libSTEERBase");
gSystem->Load("libESD");
gSystem->Load("libAOD");
gSystem->Load("libANALYSIS");
gSystem->Load("libANALYSISalice");
gSystem->Load("libCORRFW");
gSystem->Load("libPWGmuon");
gSystem->Load("libPWGmuondep");
//Use AliRoot includes to compile our task
gROOT->ProcessLine(".include $ALICE_ROOT/include");
gROOT->ProcessLine(".include $ALICE_PHYSICS/include");
gROOT->ProcessLine(".include $ALICE_ROOT/lib");
gROOT->ProcessLine(".include $ALICE_PHYSICS/lib");
gSystem->AddIncludePath("-I.");
gROOT->ProcessLine(".include $ROOTSYS/include");
gROOT->ProcessLine(".include $ALICE_ROOT/include");
gSystem->SetIncludePath("-I. -I/include -I$ROOTSYS/include -I$ALICE_ROOT/MUON -I$ALICE_ROOT/include -I$ALICE_PHYSICS/
```

```

#include");

#ifndef
///////////
// #include"
void trigger()
{
    ofstream ouf2("LHC17kScalerINT.out");
    const char *runListName = "LHC17krunlist.txt";
    if(!runListName) {
        cout << "run_list_file_name_does_not_exist...stop now!"
            << endl;
        return NULL;
    }
    ifstream runListFile;
    runListFile.open((char*)runListName);
    Int_t runNr;
    if (runListFile.is_open()) {
        while (kTRUE){
            runListFile >> runNr;
            if(runListFile.eof()) break;
            cout<<runNr<<"\n";

            AliAnalysisTriggerScalers scaler(runNr,"raw://");
            AliLHCData* lhc = static_cast<AliLHCData*>
                (scaler.GetOCDBObject("GRP/GRP/LHCData",runNr));

            Int_t NumberOfInteractingBunches(0);
            Int_t NumberOfInteractingBunchesMeasured(0);
            Int_t NIBM2(0);

            int beam1(0);
            int beam2(1);
       ///////////
        AliLHCDipValI* val = lhc -> GetBunchConfigDeclared
            (beam1,0);

        for ( Int_t i = 0;i<val->GetSizeTotal(); ++i )
        {
            if ( val->GetValue(i) < 0 )
                ++NumberOfInteractingBunches;
        }

        AliLHCDipValI* valm = lhc->GetBunchConfigMeasured
            (beam1,0);
    }
}

```

```
for ( Int_t i = 0; i < valm->GetSizeTotal(); ++i )
{
    if ( valm->GetValue(i) < 0 )
        ++NumberOfInteractingBunchesMeasured;
}

valm = lhc->GetBunchConfigMeasured(beam2,0);
cout << NumberOfInteractingBunches << endl;

AliAnalysisTriggerScalerItem *ts2 = scaler.
GetTriggerScaler(runNr,"L0b","CINT7-B-NOPF-MUFAST");
ouf2 << runNr <<"\n" << ts2->Rate() <<"\n\n" <<
NumberOfInteractingBunchesMeasured << endl;
}
}
else {
    cout << "run_list_file" << runListName <<
"\ndoes not exist...stop now!" << endl;
    return NULL;
}
runListFile.close();
}
```

# ReadPurity.C

```
void ReadPurity()
{
    TFile *file = new TFile("/home/amal/Desktop/fnorm/17h/
000271868_event_stat.root");
    TH2F *hist= (TH2F*)file->Get("fHistStat");
    hist->SetDirectory(0);
    file->Close();
    Double_t bY = 0;
    Double_t aY = hist->GetYaxis();
    Int_t nBinsY = hist->GetYaxis()->GetNbins();
    for (Int_t i=1; i<=nBinsY; ++i) {
        TString s = hist->GetYaxis()->GetBinLabel(i);
        cout << "BIN====" << i << " " << s.Data() << endl;
        if (s.Contains("CMSL7")) {
            bY = i;
            break;
        }
    }
    Double_t bX = 0;
    Double_t aX = hist->GetXaxis();
    Int_t nBinsX = hist->GetXaxis()->GetNbins();
    for (Int_t i=1; i<=nBinsX; ++i) {
        TString s = hist->GetXaxis()->GetBinLabel(i);
        cout << "BIN====" << i << " " << s.Data() << endl;
        if (s.Contains("accepted")) {
            bX = i;
            break;
        }
    }
    const Double_t db = hist->GetBinContent(1,bY);
    const Double_t da = hist->GetBinContent(bX,bY);
    const Double_t dp = da / db;
    cout << bX << endl;
    cout << bY << endl;
    cout << "ALL=" << db << " "
        << "SEL=" << da << " "
        << "PUL=" << dp << endl;
    cout << db << " " << da << " " << dp << endl;
    return;
}
```

# muCalc.C

```
void muCalc(){

    Int_t run;
    Double_t l0bMB; // l0b MB rate
    Double_t nb; //number of bunches colliding
    Double_t prenumerator;
    Double_t premudenominator;
    Double_t premu; //
    Double_t mu; //mu value
    Double_t pf; //purity fraction
    Double_t fLHC = 11245; //LHC frequency
    Double_t fpileup;
    Double_t fpileuperror;
    /////////////////////////////////
    TH1F *hfpileup = new TH1F("fpileup","fpileup",102,0,102);
    TH1F *hfpileuperror = new TH1F("fpileup","fpileup",
    102,0,102);

    TFile *filemb = new TFile("purity/LHC17k_CINT_purity.root");
    TH1F hMB = (TH1F)filemb->Get("LHC17k_CINT_purity");

    ifstream infMB("LHC17kScalerINT.out");

    for(Int_t i=0; i<102; i++){
        infMB >> run >> l0bMB >> nb;

        pf = hMB->GetBinContent(i+1);

        prenumerator = pf*l0bMB;
        premudenominator = nb*fLHC;

        premu = prenumerator/premudenominator;

        mu = -TMath::Log(1-premu);

        fpileup = mu/(1 - TMath::Exp(-mu));
    ///////////////////////////////
}
```

```
cout << fpileup << endl;
fpileuperror = (1/TMath::Sqrt(pf) + 1/TMath::Sqrt(10bMB)
+ 1/TMath::Sqrt(nb) + 1/TMath::Sqrt(fLHC));
hfpileup->GetXaxis()->SetBinLabel(i+1,Form("%d",run));
hfpileup->SetBinContent(i+1,fpileup);

hfpileuperror->SetBinContent(i+1,fpileuperror);
}

TCanvas *cfpileup = new TCanvas("hfpileup","hfpileup",
0,0,600,600);
hfpileup->GetYaxis()->SetTitle("f_{pile-up}");
hfpileup->GetXaxis()->SetTitle("Run");
hfpileup->SetTitle("Pileup\u2225fraction\u2225(pp)");
hfpileup->GetXaxis()->SetTitleOffset(1.3);
hfpileup->GetYaxis()->SetTitleOffset(1.3);
hfpileup->SetLabelSize(0.0235);
hfpileup->Draw();
hfpileup->SaveAs("LHC17k_Pileupfraction.root");
}
```

# NormFinal.C

```
#include <math.h>
#include <iostream.h>
void NormFinal()
{
    const double f_rev = 11245;
    const int n=102;
    int Run;
    double L0b_CINT7 ,L0b_CMSL7 ,L0b_CMSH7 ,Nb ,PF_CINT7 ,PF_CMSL7 ,
    PF_CMSH7 ,CF_CINT7 ;

    double CF_MB ,PF_MB ,L0b_MB ;

    double FNorm_MSL ;
    double FNorm_MSH ;

    double SigmaMSL ;
    double SigmaMSH ;

    double FNormErrMSL ;
    double FNormErrMSH ;

    double FNorm_MSL_Final1 ;
    double FNorm_MSH_Final1 ;
    double FNorm_MSL_Final2 ;
    double FNorm_MSH_Final2 ;
    double FNorm_MSL_Final ;
    double FNorm_MSH_Final ;

    double FNormErrMSL_Final ;
    double FNormErrMSH_Final ;

    ifstream fin("AnalysisFNorm_Scalar_LHC17k.txt");

    cout << "Run" << setw(20) << "FNorm_MSL" << setw(15)
    << "FNormErrMSL" << setw(15) << "FNorm_MSH" << setw(15)
    << "FNormErrMSH" << endl;
    for(int i=0; i<n;i++)
    {
```

```

//////////fin >> Run >> L0b_CINT7 >> L0b_CMSH7 >> L0b_CMSL7
>> Nb >> PF_CINT7 >> PF_CMSH7 >> PF_CMSL7
>> CF_CINT7;

// COTVX MB Trigger
CF_MB = CF_CINT7; // CF_CINT7;
PF_MB = PF_CINT7; // PF_CINT7;
L0b_MB = L0b_CINT7; // L0b_CINT7;

// MSL Trigger FNorm & FNormErr
FNorm_MSL = (L0b_MB*PF_MB*CF_MB)/
(L0b_CMSL7*PF_CMSL7);
SigmaMSL = sqrt((1/L0b_MB)+(1/L0b_CMSL7));
FNormErrMSL = FNorm_MSL*SigmaMSL;

FNorm_MSL_Final1+=FNorm_MSL/pow(SigmaMSL,2);
// Numerator
FNorm_MSL_Final2+=(1/pow(SigmaMSL,2));
// denominator

// MSH Trigger FNorm & FNormErr
FNorm_MSH = (L0b_MB*PF_MB*CF_MB)/
(L0b_CMSH7*PF_CMSH7);
SigmaMSH = (1/L0b_MB)+(1/L0b_CMSH7);
FNormErrMSH = FNorm_MSH*SigmaMSH;

FNorm_MSH_Final1+=(FNorm_MSH/pow(SigmaMSH,2));
FNorm_MSH_Final2+=(1/pow(SigmaMSH,2));

cout << Run << setw(15) << FNorm_MSL <<
setw(15)
<< FNormErrMSL << setw(15) << FNorm_MSH <<
setw(15) << FNormErrMSH << endl;
}

//////////fin.close();

FNorm_MSL_Final = FNorm_MSL_Final1/(double)
FNorm_MSL_Final2;
FNorm_MSH_Final = FNorm_MSH_Final1/(double)
FNorm_MSH_Final2;

cout << "FNorm_MSL_final=" << FNorm_MSL_Final
<< endl;
cout << "FNormErrMSL_Final="

```

```
<< FNorm_MSL_Final*sqrt(1/FNorm_MSL_Final2)
<< endl;

cout << "FNorm_MSH_final=" << FNorm_MSH_Final
<< endl;
cout << "FNormErrMSH_Final="
<< FNorm_MSH_Final*sqrt(1/FNorm_MSH_Final2)
<< endl;
}
```